ISOTHERMAL MODELS OF COMBUSTION CHAMBER FLOWS

by

Anthony Simon Green

Thesis submitted for the degree of
Doctor of Philosophy
in the Faculty of Engineering
University of London
and for the
Diploma of Membership
of Imperial College

Imperial College of Science and Technology
Mechanical Engineering Department

June 1981

ABSTRACT

This thesis describes measurements and calculations of isothermal flows in a range of water models intended to represent practical gas-turbine combustion chambers. The simplest model is a two-dimensional, axisymmetric geometry which incorporates a slot jet supplied from an annulus. The three-dimensional models include a simulation of a primary zone with fixed angle primary jets and a more complex model consisting of an annulus, primary and dilution ports.

Distributions of axial mean velocity and normal stress, measured with a laser Doppler anemometer, are used as data for subsequent comparison with calculated results. A numerical scheme solves the transport equations for velocity, pressure, turbulence kinetic energy and energy dissipation rate using a finite-difference formulation. The qualitative and quantitative accuracy of the calculation scheme, in predicting the measured values for each model geometry, is discussed and the cause of discrepancies analysed. The extent to which numerical diffusion, grid node distribution and pressure dominance affect the solution is also examined for each model geometry.

To illustrate the application of the calculation scheme to practical combustion chamber design, a parametric study is presented for each geometry and the implications discussed. For the two-dimensional axisymmetric geometry, a reduction in slot width created separation regions at the leading edge of the slot which reduced the primary zone recirculation strength. Similar results were found for the three-dimensional non-annulus cases where inlet mass flow ratios, in the range $0.14 < \dot{m}_b/\dot{m}_p < 1.54$, caused a monatonic decrease in recirculation strength. The three-dimensional model with an annulus, however, showed that, for a similar range of $\dot{m}_b/\dot{m}_p$, the recirculation strength decreased to a constant value caused by an increasing proportion of the baseplate inlet flow being recirculated back upstream.

ACKNOWLEDGEMENTS

I would like to express my gratitude to Professor J.H. Whitelaw, who supervised the work in this thesis, for his encouragement, criticism and friendly advice throughout the course of research.

The work has also benefitted by being a part of a larger overall research collaboration between Imperial College and industry. I would like to thank particularly: Dr. W.P. Jones and Dr. J.J. McGuirk of the Department of Chemical Engineering and Chemical Technology at Imperial College, for advice with numerical modelling; Mr. A. Sotheran of Rolls-Royce Ltd., Bristol and Mr. M. Sherwood, Mr. D.C. Dryburgh and Dr. C.H. Priddin of Rolls-Royce Ltd., Derby, for advice and for periods spent in both combustion departments; and, finally, to Mr. J.B. Jamieson, Mr. R. Cottington, Mr. J. Bullard and Dr. C. Coats of the National Gas Turbine Establishment for continued interest and advice. Periodic seminars held with Rolls-Royce Ltd. and N.G.T.E. to present progress in the research work, together with my colleagues Sandra Godoy and Zafar Khan, have given me valuable experience.

I would like to acknowledge help and assistance from the technical staff of the Fluids Section, particularly Mr. W. Crew and Mr. O. Vis who made the water models used in the experiments. Excellent library facilities were provided by Miss E. Archer and her staff in the department library. I would also like to thank Miss J. Davies for typing the thesis.

Fellow room mates Sami Al Sanea and Pavlos Tagarakis, and also Bessam Younis deserve a special mention for their friendship throughout my time at Imperial College.

Finally I gratefully acknowledge the financial assistance provided by the National Gas Turbine Establishment.

CONTENTS

Page No.

Abstract 2

Acknowledgements 3

Contents 4

List of Figures 9

List of Tables 15

Nomenclature 16

CHAPTER 1

INTRODUCTION

1.1 OBJECTIVES 20

1.2 COMBUSTION CHAMBERS AND DESIGN CRITERIA 21

  1.2.1 Chamber Design 21

  1.2.2 Fuel Injection 22

  1.2.3 Basic Design Criteria 23

1.3 COMBUSTION CHAMBER RESEARCH 24

  1.3.1 Experimental Research 24

  1.3.2 Empirical Correlation 26

  1.3.3 Numerical Modelling 26

1.4 ASSESSMENT 28

1.5 PRESENT CONTRIBUTION 31

1.6 OUTLINE OF THESIS 32

CHAPTER 2

THE EXPERIMENTAL APPARATUS

2.1 INTRODUCTION 34

2.2 THE WATER FLOW RIG 34

2.3 THE MEASURING TECHNIQUE 35

Page No.

2.3.1 Introduction 35
2.3.2 The Optical System 36
2.3.3 The Signal Processing System 41
2.3.4 The Method of Measurement 43

2.4 LIMITATIONS IN ACCURACY OF THE MEASURING TECHNIQUE 44
2.4.1 Introduction 44
2.4.2 Finite Transit Time Broadening 44
2.4.3 Velocity Gradient Broadening 44
2.4.4 Instrument Noise Broadening 45

2.5 SUMMARY 46

CHAPTER 3

THE CALCULATION PROCEDURE

3.1 INTRODUCTION 47
3.2 DESCRIPTION OF THE EQUATIONS 47
3.2.1 The Conservation Equations 47
3.2.2 The Turbulence Model 48
3.2.3 The Finite-difference Formulation 51
3.2.4 The Boundary Conditions 53
3.2.5 The Solution of the Finite-difference equations 57

3.3 LIMITATIONS OF THE CALCULATION APPROACH 60
3.3.1 Limitations of the Turbulence Model 60
3.3.2 Limitations of the Finite-difference Technique 63

3.4 SUMMARY 64

Page No.

CHAPTER 4

A TWO-DIMENSIONAL MODEL WITH AN ANNULUS

4.1 INTRODUCTION 65

4.2 THE MODEL DETAILS 65

  4.2.1 The Geometry 65

  4.2.2 The Flow Pattern 66

4.3 THE MEASUREMENTS 66

4.4 THE CALCULATION DETAILS 70

4.5 COMPARISON OF MEASURED AND CALCULATED RESULTS 72

4.6 CALCULATED RADIAL VELOCITY, PRESSURE AND KINETIC ENERGY 74

4.7 FURTHER CALCULATIONS 76

4.8 SUMMARY 79

CHAPTER 5

A THREE-DIMENSIONAL MODEL WITHOUT AN ANNULUS

5.1 INTRODUCTION 81

  5.1.1 Limitations of Two-dimensional Study 81

  5.1.2 Extension to Three-dimensional Flows 81

5.2 DETAILS OF THE MODEL 83

  5.2.1 The Geometry 83

  5.2.2 Observed Flow Patterns Using Flow Visualisation 84

5.3 THE MEASUREMENTS 86

  5.3.1 The Range of Measurements 86

  5.3.2 Measurements with Baseplate Jet Only (Cases 1 and 2) 87

  5.3.3 The Measurements Incorporating a Baseplate Jet and Baffle (Case 3) 90

  5.3.4 Further Measurements Incorporating a Baseplate Jet and Baffle (Cases 4 and 5) 91

Page No.

5.4 DETAILS OF THE CALCULATIONS 93

5.4.1 The Grid 93

5.4.2 The Boundary Conditions 93

5.4.3 The Application of the Numerical Model 94

5.5 COMPARISON OF MEASUREMENTS AND CALCULATIONS 96

5.5.1 Results for Case with Baseplate Jet (Case 2) 96

5.5.2 Results for Case with Baseplate Jet and Baffle (Case 3) 97

5.5.3 Radial Velocity and Kinetic Energy Results for Case 3 99

5.5.4 Results for Cases with Baseplate Jet and Baffle (Cases 4 and 5) 101

5.5.5 Further Calculations 102

5.6 DISCUSSION AND CONCLUSIONS 104

CHAPTER 6

A THREE-DIMENSIONAL MODEL WITH AN ANNULUS

6.1 INTRODUCTION 106

6.1.1 Incorporating the Annulus 106

6.1.2 Outline of the Work 107

6.2 DETAILS OF THE MODEL 108

6.2.1 The Geometry 108

6.2.2 The Flow Patterns 109

6.3 THE MEASUREMENTS 109

6.4 DETAILS OF THE CALCULATIONS 113

6.4.1 The Grid 113

6.4.2 The Boundary Conditions 114

6.4.3 The Application of the Numerical Model 115

Page No.

6.5 THE CALCULATED RESULTS 116
6.5.1 Comparison of Measured and Calculated Axial Mean Velocity 116
6.5.2 Calculated Results for Radial Velocity and Turbulence Kinetic Energy 119
6.6 FURTHER CALCULATIONS 120
6.7 DISCUSSION AND SUMMARY 122

CHAPTER 7

CONCLUSIONS

7.1 CONTRIBUTIONS OF THE WORK 125
7.2 FUTURE WORK 128

REFERENCES 130

FIGURES 139

LIST OF FIGURES

CHAPTER 1

Figure 1.1 Tubular combustion chamber and arrangement

Figure 1.2 Tubo-annular arrangement

Figure 1.3 Annular combustion chamber

Figure 1.4 Swirl-atomiser fuel injector

Figure 1.5 Vaporiser fuel injector

Figure 1.6 Combustion chamber zones

CHAPTER 2

Figure 2.2.1 Plan view of water flow rig

Figure 2.3.1 The scattering volume
- (a) Fringe model of scattering volume
- (b) Dimensions of scattering volume ellipsoid

Figure 2.3.2 The measuring system

Figure 2.3.3 Frequency shift effects and beam order
- (a) Velocity probability distribution
- (b) Corresponding frequency probability distribution
- (c) Corresponding frequency probability distribution with frequency shift f_s
- (d) Beam order of diffraction grating

Figure 2.3.4 Schematic diagram of processing equipment and signal waveforms

Figure 2.4.1 Common types of broadening
- (a) Finite transit time broadening
- (b) Velocity gradient broadening

CHAPTER 3

Figure 3.1 Velocity and scalar control volumes for a three-dimensional calculation domain.
  (a) u,v and scalar control volumes in x-y plane
  (b) w and scalar control volumes in y-z plane

Figure 3.2 Cyclic boundary conditions
  (a) Physical domain with periodic uniformity about 0
  (b) Calculation domain with cyclic boundary conditions applied at periodic axes

CHAPTER 4

Figure 4.2.1 The two-dimensional axisymmetric model
Figure 4.2.2 Flow pattern from flow visualisation
Figure 4.3.1 The measuring locations
Figure 4.3.2 Radial profiles of mean axial velocity and normal stress
  (a) Axial locations $1.64 < {}^{x}/D < 2.13$
  (b) Axial locations $2.25 < {}^{x}/D < 2.63$
  (c) Axial locations $3.02 < {}^{x}/D < 4.25$

Figure 4.4.1 The finite-difference grid (28x30 nodes)
Figure 4.4.2 Dependence of mean axial velocity on grid node density at ${}^{x}/D = 2.55$
Figure 4.5.1 Comparison of calculated and measured mean axial velocity profiles at four locations
Figure 4.5.2 Comparison of calculated and measured streamline contours (determined from mean axial velocity)

Figure 4.6.1 Contours of calculated radial velocity ($\overline{v}$)

Figure 4.6.2 The pressure distribution
  (a) The local normalised pressure contours (p_c) in the gap region
  (b) A cross-section of the pressure contours at $^r/R = 0.99$
Figure 4.6.3 Contours of calculated turbulence kinetic energy
Figure 4.7.1 Location of trajectory angle and magnitude of jet resultant velocity
Figure 4.7.2 Calculated radial velocity contours for variations in local geometry
  (a) Reduced gap width by 50%
  (b) Reduced gap width by 25%
  (c) Increased annulus width by 25%
  (d) Reduced annulus width by 25%
Figure 4.7.3 Calculated axial velocity profiles for variations in local geometry (i)
  (a) Axial velocity profiles at $^x/D = 1.95$ for variation in gap width
  (b) Axial velocity profiles at $^x/D = 1.95$ for variation in annulus width
Figure 4.7.4 Calculated axial velocity profiles for variations in local geometry (ii)
  (a) Axial velocity profiles at $^x/D = 2.0$ for variation in annulus width
  (b) Axial velocity profiles at $^x/D = 2.0$ for variation in gap width

CHAPTER 5

Figure 5.2.1 The three-dimensional model without an annulus

Figure 5.2.2 Flow patterns from flow visualisation

(a) Flow pattern for geometry without a baffle (Case 1)

(b) Flow pattern for geometry without a baffle (Case 2)

(c) Flow pattern for geometry with a baffle (Cases 3, 4 and 5)

Figure 5.3.1 The measuring locations

Figure 5.3.2 Measured profiles for geometry without a baffle

(a) Mean axial velocity profiles at $^{x}/D = 4.6$ for Case 1 ($\theta = 0^{o}$)

(b) Measured mean axial velocity profiles for Case 2

(c) Measured normal stress profiles for Case 2

Figure 5.3.3 Measured mean axial velocity contour for Case 2 ($\theta = 45^{o}$)

Figure 5.3.4 Measured profiles for geometry with a baffle (Case 3)

(a) Measured mean axial velocity profiles for Case 3

(b) Measured normal stress profiles for Case 3

Figure 5.3.5 Measured mean axial velocity contours for Case 3 ($\theta = 45^{o}$)

Figure 5.3.6 Measured mean axial velocity contours for Case 4 ($\theta = 45^{o}$)

Figure 5.3.7 Measured mean axial velocity contours for Case 5 ($\theta = 45^{o}$)

Figure 5.4.1 The finite-difference grid (10 x 19 x 27 nodes)

Figure 5.5.1 Comparison of calculated and measured mean axial velocity contours for Case 2 ($\theta = 45^{o}$)

Figure 5.5.2 Comparison of calculated and measured mean axial velocity profiles for Case 2
Figure 5.5.3 Comparison of calculated and measured mean axial velocity contours for Case 3 ($\theta = 45^{\circ}$)
Figure 5.5.4 Comparison of calculated and measured mean axial velocity profiles for Case 3
Figure 5.5.5 Calculated mean axial velocity contours for Case 3 ($\theta = 0^{\circ}$)
Figure 5.5.6 Calculated mean radial velocity contours for Case 3
Figure 5.5.7 Calculated turbulence kinetic energy contours for Case 3
Figure 5.5.8 Comparison of calculated and measured mean axial velocity contours for Case 4 ($\theta = 45^{\circ}$)
Figure 5.5.9 Comparison of calculated and measured mean axial velocity contours for Case 5 ($\theta = 45^{\circ}$)
Figure 5.5.10 Relationship between upstream recirculation ratio and inlet mass flow ratio

CHAPTER 6

Figure 6.2.1 The three-dimensional water model with an annulus
Figure 6.6.2 The flow patterns from flow visualisation
Figure 6.6.3 The measuring locations
Figure 6.3.2 Measured mean axial velocity contours for $\theta = 0^{\circ}$ and $\theta = 45^{\circ}$ planes
Figure 6.3.3 Measured normal stress contours for $\theta = 0^{\circ}$ and $\theta = 45^{\circ}$ planes
Figure 6.4.1 The finite-difference grid (10 x 20 x 30 nodes)
Figure 6.5.1 Calculated mean axial velocity contours for $\theta = 0^{\circ}$ and $\theta = 45^{\circ}$ planes
Figure 6.5.2 Comparison of measured and calculated mean axial velocity profiles

Figure 6.5.3 Calculated mean radial velocity contours for $\theta = 0^{o}$ and $\theta = 45^{o}$ planes
Figure 6.5.4 Calculated turbulence kinetic energy contours for for $\theta = 0^{o}$ and $\theta = 45^{o}$ planes
Figure 6.6.1 Relationship between upstream recircualtion ratio and inlet mass flow ratio
Figure 6.6.2 Relationship between initial jet trajectory angles and inlet mass flow ratio
Figure 6.6.3 Relationship between primary jet to annulus mass flow ratio and inlet mass flow ratio

LIST OF TABLES

CHAPTER 1

Table 1.1 Experimental Approach
Table 1.2 Empirical Correlation
Table 1.3 Numerical Modelling

CHAPTER 2

Table 2.1 Water Rig Details
Table 2.2
  (a) Optical System Components
  (b) Calculated Optical System Parameters
Table 2.3 The Signal Processing Equipment
Table 2.4 Specifications of the Rotating Diffraction Grating

CHAPTER 3

CHAPTER 4

Table 4.1 Influence of Geometrical Modifications on Jet Behaviour

CHAPTER 5

Table 5.1 Flow Rates for Measured Cases
Table 5.2 Location of Measured and Calculated Velocities
Table 5.3 Variation in Recirculation Ratio for Cases 3 to 8

CHAPTER 6

Table 6.1 Primary Port Flow Variation for Three Grid Sizes
Table 6.2 A Parametric Study

NOMENCLATURE

Symbol	Meaning
A	Area of control volume face
a	Coefficient in finite-difference equations
b	Coefficient in finite-difference equations
C_μ C_1 C_2	Constants in turbulence model
D	Characteristic diameter of model
d_{ph}	Diameter of photomultiplier pin hole
d_x d_y d_z	Dimensions of scattering volume ellipsoid
E	Constant in "law of the wall"
e	Constant used in fraction $(\frac{1}{e^2})$ of maximum laser light intensity
F	Weighting factor used in finite-difference equations
f_D	Doppler frequency
f_s	Shift frequency
K	Proportion of primary jet mass flow that recirculates upstream
K	Turbulence kinetic energy
K	Order of diffracted beams
ℓ	Local length scale
l_1	Distance between collecting lens and photomultiplier pin hole
l_2	Distance between measuring volume and collecting lens
M	Magnification of collecting lens
$\dot{m}$	Local mass flow rate

Symbol	Meaning
N	Number of lines on diffraction grating
N_f	Number of fringes in scattering volume
N_{ph}	Number of fringes in measuring volume
Pe	Local Peclet number
p	pressure
p_c	Normalised pressure
$\dot{q}$	Local mass flux
R	Characteristic radius of model
R_{AV}	Proportion of total mass flow rate that recirculates upstream
r	radial dimension
S_ϕ S_u S_p	Linearised source terms
s	Distance between lines on diffraction grating
$\bar{T}_{AV}$	Average slot jet resultant velocity
U	Axial velocity
$\bar{U}_{AV}$	Average slot jet axial velocity
$\overline{u^2}$	Axial normal stress
V	Radial velocity
$\bar{V}_{AV}$	Average slot jet radial velocity
W	Circumferential velocity
X_i	Coefficient in TDMA recurrence formula
x	Axial dimension
Y_i	Coefficient in TDMA recurrance formula
y	Radial dimension
y^+	Characteristic parameter used in "law of the wall"

Greek symbol	Meaning
$\alpha_{initial}$	Initial trajectory angle
α_{AV}	Average slot jet trajectory angle (= $\tan^{-1}$ (V_{AV}/U_{AV})
Γ_{ϕ}	Exchange coefficient
Δx	Increment in axial direction
δ_{ij}	Kronecker delta
ε	Turbulence energy dissipation rate
ε_{W}	Value of ε at wall
κ	von Karman constant
λ	Wavelength of laser light source
μ	Dynamic viscosity
ν	Kinematic viscosity
ν_{t}	Eddy viscosity
ρ	Density
σ_{F}	RMS finite transit time broadening
σ_{g}	RMS velocity gradient broadening
σ_{i}	RMS instrument broadening
σ_{k}	Constant Prandtl number in turbulence kinetic energy equation
σ_{ε}	Constant Prandtl number in energy dissipation rate equation
τ_{W}	Wall shear stress
ϕ	Dependent variable
ψ	Half angle between anemometer beams
ω	Rotational speed of diffraction grating

Superscript	Meaning
u,v,w,p k,ε,ϕ	Notation for each variable
$*$	Uncorrected value
$'$	Correction value or fluctuating value
$-$	Time averaged value

Subscript	Meaning
N,S,E,W	Nodal positions
L,R,P	
i,j,k	Indices of co-ordinates
inlet	Inlet value
ph	Pin hole
u,v,w,p	Notation for each variable
k,ε,ϕ	

CHAPTER 1

INTRODUCTION

1.1 OBJECTIVES

The work in this thesis is intended to contribute to the development and exploitation of primitive variable numerical models in the design of practical gas-turbine combustion chambers. The desirability of the modelling approach has been expressed elsewhere, e.g. (Jones et al, 1977) (Bruce et al, 1979) and is now an established research tool in combustion processes. The credibility of numerical modelling and degree to which it is exploited by designers is, however, subject to demonstration, and has recently heralded a series of exact comparisons between measurements, in simple combustion chambers, and calculations using a numerical model (Jones et al, 1977; Jones and Priddin, 1978; Bruce et al, 1979; and Swithenbank et al, 1980).

Deficiencies between measured and calculated values of flow variables have fallen broadly into two categories, chamber aerodynamics and combustion modelling. This thesis deals with the former deficiency by examining, in detail, the comparison between measurements and calculations of the isothermal flow in model combustion chambers that still retain important details of real chambers. The objectives may be summarised as:

(i) To measure the distribution of the main velocity component using laser Doppler anemometry in a series of two and three-dimensional water models of combustion chambers so as to provide reliable data for comparison with calculations.

(ii) To use a primitive variable numerical model to calculate the flow variables in the water models and assess its accuracy and performance.

In order to relate these objectives to design practice the following section briefly describes the background to combustion chamber design and design criteria.

1.2 COMBUSTION CHAMBERS AND DESIGN CRITERIA

1.2.1 Chamber Design

The evolution of the gas-turbine combustion chamber in aircraft engines may be conveniently described by reference to three basic chamber shapes: tubular, tubo-annular and annular.

(i) The tubular chamber, illustrated in Figure 1.1, was the first type to be used extensively in gas-turbine engines. The combustion section of an engine would comprise eight or ten chambers arranged around a common centre between compressor and turbine. Each chamber consisted of a flame tube, annular casing and fuel inlet device. Compressor air was delivered through a separate diffuser and the separate outlet nozzles were located on a ring before the turbine. To facilitate ignition each chamber was connected.

Although this type of chamber was not the optimum choice for either weight or flow area ratio its early use was dictated by the testing facilities of the day where only relatively small airflows, suitable only for dimensionally small chambers, could be generated. In present day aircraft gas-turbine engines, the tubular combustion chamber is no longer used although it is widely used in industrial applications, e.g. for electrical power generation in offshore installations (Elmhal et al, 1980). In these applications the tubular chamber engines, which may be de-rated aircraft gas-turbines (McKnight, 1979), still have some advantages where easy maintenance is at a premium. For example, close inspection of turbine blades can be made by removing one chamber only (Pilkington and Carlisle, 1968).

(ii) The tubo-annular chamber, illustrated in Fig. 1.2, was a compromise, between the tubular and the full annular chamber, by improving the flow area ratio and also decreasing the assembled weight. However, the task of designing the chamber was substantially more difficult due to the irregular shape of the regions around the flame tubes. With the advent of adequate air flow rates for testing facilities this type of chamber was superceded by the full annular chamber.

(iii) The full annular chamber is the optimum shape for low weight, compactness (i.e. short length) and ignition distribution. An example is illustrated in Figure 1.3. The chamber can be fabricated as a single component and is very much simpler than either of the previous designs.

1.2.2 Fuel Injection

Two basic types of fuel injection device are used in contemporary aircraft gas-turbines; these are the swirl-atomiser and the vaporiser:

(i) The swirl-atomiser, Figure 1.4, uses an air swirler, which imparts a circumferential momentum to the incoming air. This creates a depression on the centre-line between the base plate and the plane of the primary jets and causes some of the primary jet air to travel upstream and recirculate. The recirculation stabilises the flame by decreasing the velocity and introducing hot reaction products to form a source of continuous ignition. The fuel is atomised under high pressure and projected in a cone shaped spray from the centre of the swirler so as to mix with the swirler air to form a combustible mixture (Clare et al, 1961) and (Bryan et al, 1969).

(ii) The vaporiser, Figure 1.5, acts by pre-mixing some of the air from the diffuser exit, with fuel from a jet, under low pressure. This mixture is then projected upstream from the vaporiser from a point within the primary zone; thus the vaporiser body extends into the primary zone, as shown. This arrangement causes a depression on the centre-line between the vaporiser body and the plane of the primary jets. The recirculation is caused by part of the primary jet air flowing upstream and further strengthened by the "pumping" action of the vaporiser flow (Parnell and Williams, 1969).

1.2.3 Basic Design Criteria

The basic aerodynamic design criteria of a typical combustion chamber may be summarised with reference to zones (Figure 1.6) as follows:

(i) The annulus zone should pass a uniform distribution of air to the primary and dilution ports (and cooling rings)at highest Mach number consistent with stable port entry flow,to minimise pressure loss and achieve maximum flame tube cooling.

(ii)The primary zone of the chamber should provide a stable recirculation pattern giving efficient burning of the fuel and air mixture without excessive temperature gradients. The formation of carbon-monoxide and oxides of nitrogen are sensitive to the local aerodynamics and temperature in the region as is the completeness of fuel combustion (unburnt hydrocarbons) and are important from an efficiency and pollution consideration (Friswell, 1972) and (Sawyer, 1972).

(iii)The dilution zone of the chamber should mix excess air so as to give a circumferentially uniform gas temperature distribution with a specified radial temperature profile for optimum turbine blade life.

The conciseness of these criteria belies the difficulties and considerable effort required of the combustion chamber designer who, in addition, is subject to variations in both compressor and turbine design. Research aimed at providing the designer with reliable guidelines has encompassed a diverse range, some of which is reviewed in the following section.

1.3 COMBUSTION CHAMBER RESEARCH

Considerable research into gas-turbine combustion chamber design and performance has been undertaken by both industry and research institutions over the last thirty-five years. The investigations have been both theoretical and experimental and have encompassed isothermal, air and water flows, as well as reacting flows. The degree of sophistication of both theoretical and experimental work has increased throughout the period due to improvements in measuring and computational equipment. The different research approaches may be categorised roughly under three main headings: experimental, empirical correlation and numerical modelling. The headings are also in approximate chronological order and will now be discussed separately.

1.3.1 Experimental Research

Very few recent published papers by industry on detailed combustion chamber flows may be found in the literature for confidentiality reasons. The data that does exist has concentrated on model combustion chambers, usually with simplified geometries and running at atmospheric pressure,for use as comparative data. The work cited in Table 1.1 ranges from isothermal to combusting flows mainly in practical chambers and has been chosen as representative of current design, and development practice.

A significant proportion of the combustion designers' time is used in determining the variations in overall performance of a chamber when altering, for example,the geometry. This aspect is important when the chamber is undergoing development or subject to variations in components due to the discovery of a more economic manufacturing method or production tolerances. The traditional approach has been to produce the particular variation in the chamber and to compare its performance, with an established standard, by experiment. The range of experimental options extend from the inexpensive water-model flow visualisation up to the expensive , high pressure combustion test with full instrumentation. It is this dependence upon

Table 1.1 Experimental Approach

Reference	Type of Study	Remarks
Poulston and Winter (1957)	3-d isothermal study with water and air.	Approximate water velocities determined from flash-light photography of seeded flow. Air flow directions determined by wool tufts.
Hiett and Powell (1962)	3-d isothermal and reacting study with liquid fuel at atmospheric pressure	Air flow velocities, isothermal and reacting, measured with probe. Temperature distribution measured with thermocouples. Simple chamber design without primary ports and low combustion intensity as used by Poulston and Winter (1957).
Gerrard (1961)	3-d isothermal study with water	Describes water flow rig, flow visualisation and scaling effects. One radial traverse of axial velocity given for flame-tube and annulus upstream of primary ports. Production-type chamber.
Clark et al (1963)	3-d isothermal study with air and water; reacting study with gaseous and liquid fuels at atmospheric pressure.	Compares water and air (with concentration tracers) and reacting flows in a production-type chamber. Emphasises similarities between isothermal and reacting flows and temperature/concentration patterns.
Youssef (1968)	3-d isothermal and reacting flows using gaseous fuel at atmospheric pressure	Compares measurements of velocity, pressure and temperature for three radial planes upstream of the primary ports in an industrial type chamber. Similarities shown between isothermal and reacting profiles.

experimentation and running tests that has encouraged a design approach based upon empirical data.

1.3.2 Empirical Correlation

This calculation approach is based upon the synthesis of simple laws and experimental data to produce overall estimates of important parameters such as pressure drop in the primary zone or average outlet temperature. The method of designing a chamber using empirical theory has been outlined by others (Tacina and Grobman, 1969) and (Odgers, 1979) in detail. The input information required by the calculation includes flame tube and annuli dimensions, size and position of entry ports, air flow, inlet total pressure, inlet fuel-air ratio, inlet total temperature etc. Briefly the calculation proceeds by estimating the flow through ports and annuli using discharge coefficients determined by experiment (see, for example, Dittrich and Graves, 1956 and Dittrich 1958); overall mass continuity is imposed by summation and adjustment in an iterative cycle. Arbitrary definitions of primary and recirculation ratios and the assumption that the primary zone is a stirred reactor (uniform pressure, temperature and fuel-air ratio where mixing and burning occur instantaneously) allow further estimates of pressure loss and temperature within the flame tube. Methods using this type of calculation are summarised in Table 1.2.

These methods have been criticised (Odgers, 1979) as not providing an accurate assessment of the flow, especially in regions where three-dimensional effects are strong, i.e. the primary zone. A further criticism is the difficulty of establishing the limitations of the various empirical estimates, for example, when designing a new chamber. These defects have given rise to a more general numerical approach based upon fundamental fluid mechanics knowledge and physical modelling.

1.3.3 Numerical Modelling

The numerical modelling approach is based upon the solution of the Navier-Stokes equations which govern fluid flow. These equations, which

Table 1.2 Empirical Correlation

Reference	Type of Study	Remarks
Tacina and Grobman (1958,1969)	Influence of tubular and annular chamber geometry on pressure loss and air flow distribution using empirical relations	Parametric graphical results correlating airflow fractions, pressure ratio, area ratio, total temperature etc. for tubular and annular chambers. Emphasises similarity between tubular and annular flow trends.
Verduzio and Campanaro (1969)	Determination of primary jet recirculation ratio	Compares upstream recirculation ratio in a simple tubular combustion chamber with a simple empirical analysis; parametric study of port number and size included.
Adkins (1978)	Determination of influence by compressor	Simple empirical model predicts variations in flame tube flow caused by compressor exit profile distortions.
Odgers (1979)	Description of design approach using empirical models	Describes the approach to chamber sizing and initial development. Discusses relevance of a range (0-3-dimensions) of models. Concludes that primary zones require 3-d models.

with suitable physical models, constitute a closed set of partial differential equations, are solved numerically using a finite-difference technique. This involves discretising the combustion chamber volume to form a grid or mesh of small control volumes to which the equations are applied. This approach is relatively new for complex combustion chamber calculations although an early example (Livesey et al, 1960) was used to examine combustion chamber entry flows. Due to the nature and limitations, of the solution procedure, physical aspects of the flow such as turbulence (see Chapter 3) and combustion have to be modelled and require some empirical input. Examples of numerical modelling applied to combustion chambers are given in Table 1.3.

Two recent review papers have attempted to assess the numerical modelling approach to combustion chamber flows. The review by McDonald (1979) discusses problem areas such as large flow gradients, dense grid distributions, singularities within the flow and the extent to which numerical modelling is capable of producing a reliable solution. The review by Lilley (1979) covers a wide range of combustion flows examining the impact of numerical modelling in each field. Emphasis is also placed upon ensuring numerical modelling is geared to the needs of the designer and the importance of relevant model experiments to highlight numerical model deficiencies.

1.4 ASSESSMENT

The degree to which each of these research approaches are used by combustion chamber designers,varies. Traditional design techniques show reliance upon a great deal of experimentation, some empirical correlation and very little numerical modelling. This is significant and can, in part, be attributed to the way in which recent research has attempted to solve combustion chamber flows. This has been to oversimplify the geometrical configurations of combustion chambers to facilitate comparisons with numerical models and, therefore, from the designers' point of view,

Table 1.3 Numerical Modelling

Reference	Type of Study	Remarks
Jones et al (1977)	3-d comparison of numerical model with reacting flow in a small research chamber at high pressure. Gaseous fuel.	Velocity and chemical species were measured using a probe. Numerical calculations resulted in over-estimation of CO causing low temperature and combustion efficiency estimates.
Serag-Eldin (1977)	3-d isothermal and reacting flows	Numerical model tested against experiments by Youssef (1967) and Serag-Eldin (1977) in a simplified combustion chamber. Favourable agreement was obtained for isothermal flow but poor agreement in the primary zone for reacting flows. Extensive measurements were not made.
Elliman et al (1978)	2-d isothermal and reacting flows	Velocity and chemical species measured using a probe. Level of agreement between measurements and calculations with numerical model varied depending on location. Discrepancies in agreement caused by combustion model and false diffusion.
Jones and Priddin (1978)	3-d studies of gaseous and liquid fuelled reacting flows in two model chambers	Comparison of probe measurements with numerical results show discrepancies in over-estimation of recirculation lengths and combustion species: CO, HC and NO.
Hirzinger and Tichtinsky (1979)	3-d study of isothermal flow in a simplified annulus and flame tube	The numerical model used an integral technique to study isothermal flow. Vector diagrams of velocity solution show implausible results.

Table 1.3 (Cont...)

Reference	Type of Study	Remarks
Jones and McGuirk (1979)	2-d isothermal and reacting (gaseous fuel) study and a 3-d reacting (liquid fuel) preliminary study.	Comparisons of probe measurements in the 2-d axisymmetric chamber to numerical results showed an under-estimation of recirculation lengths.
Novick et al (1979) and (1979a)	2-d study of isothermal and reacting (premixed gas/air) flows	Comparisons between measurements and numerical calculations (using a procedure based on Gosman and Pun, 1973) for reacting flows is confined to one temperature map which shows good agreement. The geometry of the chamber is altered to show effects of swirl, recirculation zone amplification and laterally induced secondary air supply.
Bruce, Mongia and Reynolds (1979)	Extensive 3-d study of isothermal and reacting flows	Using a combination of empirical correlation and three-dimensional numerical modelling two, reverse flow combustion chambers were designed. Development time was reduced compared to traditional methods.
Green and Whitelaw (1980)	2-d study of isothermal water flow	Investigation of annulus/flame tube interaction using a simplified 2-d axisymmetric chamber. L.d.a. measurements and numerically calculated velocities show 5%-17% agreement depending on location.

detract from the potential usefulness of the technique in solving the immediate problems.

An important example is the absence of annuli which play an important role in combustion chamber flows. Although model chambers may be constructed, without annuli, allowing the modeller to impose simple boundary conditions, practical relevance diminishes, especially when deficiencies in aerodynamic and combustion predictions still result. At this stage, therefore, it would be opportune to separate the aerodynamic from the combustion modelling for further independent study. This is important for the aerodynamics, as the limits of applicability of the numerical model may be tested to gain knowledge of how complex a geometry can be modelled and whether the model is capable of resolving geometrical changes. Further research on combustion modelling can address the tasks of modelling finite-rate reactions and turbulence/combustion interaction.

1.5 PRESENT CONTRIBUTION

The work in this thesis contributes towards the calculation of combustion chamber flows using a finite-difference numerical model. In particular, the work examines the extent to which reliable isothermal calculations of aerodynamics can be made in combustion chambers with realistic geometrical configurations. In order to test the accuracy of the numerical model the flows in a series of three water-model experimental chamber geometries were measured using a non-obtrusive measuring technique. The series consists of the following:

(i) A two-dimensional axisymmetric tubular chamber geometry with a slot primary port and an annulus.

(ii) A three-dimensional tubular chamber geometry with four circular primary ports, a centre-line jet or centre-line baffle baseplate port without an annulus.

(iii) A three-dimensional tubular chamber geometry with four circular primary and dilution ports, a centreline baffle entry port and an annulus.

Sufficiently detailed measurements were obtained to provide a reliable comparison with numerical calculations and to promote credibility of the approach. Further information is extracted from the calculations which are directly relevant to combustion chamber designers, for example, recirculation ratio and jet trajectory angles. Variations to geometries and input conditions are made to test the resolution of the numerical model and show the resulting influences on the flow.

1.6 OUTLINE OF THESIS

The thesis consists of seven chapters of which Chapters 2 and 3 give general information on the measurement and numerical techniques. Chapter 2 describes the water flow rig, its operation, associated equipment and the laser Doppler measuring technique, including an assessment of inaccuracies. Chapter 3 outlines the partial differential equation and the method of solution used by the numerical technique, including an assessment of the limitations in the physical models and numerical accuracy.

Chapter 4 describes the measured and calculated results in a two-dimensional axi-symmetric combustion chamber water model with annulus and slot primary port. Comparisons are made, between calculated and measured axial velocities,and the extent of agreement discussed. Further work on varying the geometry is performed using calculated results from the numerical model.

Chapter 5 describes the measured and calculated results in a three-dimensional combustion chamber water model (without an annulus) with four circular primary ports, two geometrical configurations and four inlet conditions. Comparisons are made, between calculated and measured axial velocities, and the extent of agreement discussed.

Chapter 6 describes the measured and calculated results in a three-dimensional combustion chamber water model with an annulus, centre-line baffle entry port, primary and dilution ports. Comparisons are made between calculated and measured axial velocities in this geometry and the extent of agreement discussed and compared to results of Chapter 5. Conclusions to the work, including recommendations for further work, are presented in Chapter 7.

CHAPTER 2

THE EXPERIMENTAL APPARATUS

2.1 INTRODUCTION

This chapter describes the rig used to arrange the water flow in each of the model geometries and the technique used to measure the mean velocity and normal stress distributions of the flow. The limitations in accuracy of the measuring technique are discussed briefly.

2.2 THE WATER FLOW RIG

A schematic diagram of the water flow rig is given in Figure 2.2.1. It comprised three tanks, a pump and connecting pipe work to provide a closed circuit water flow driven by a constant inlet head. The constant head tank (A) comprised an inlet pipe and gate valve (G) controlling the water flow from the pump, an outlet stub pipe and flange for attaching the test section, and a constant head tube (H) and overspill outlet (K). A collecting tank (B) was situated downstream of the test section and served to provide a small "back head" on the test section. This was accomplished by having the outlet level above that of the test section centreline. The outlet of the collecting tank was constructed so as to incorporate a smooth, flat gully which guided the water into the reservoir tank (C). The reservoir tank (C) was of a capacity such that the temperature rise over a long operating period was negligible and that little aeration of the water was created by the water flow from the collecting tank. Water was drawn by the pump from an outlet situated at the rear of the reservoir tank and pumped to the constant head tank. The only other connections to the reservoir tank were a by-pass inlet, designed to allow water to be pumped directly back into the reservoir tank and the overspill inlet from the constant head tube.

In operation the water was drawn from the reservoir tank by the pump and delivered to the constant head tank through valve (G). As the length of the constant head tube could be varied, and hence the inlet head to the test section, the provision for maintaining a minimal flow rate was facilitated by operation of the by-pass inlet valve (E) and line valve (F). This ensured that the pump operated efficiently and that overspill could be minimised. The test section, including the model, was bolted to the outlet stub flange of the constant head tank and was held by the collecting tank with a sliding bush. The test section was also provided with additional support to prevent sagging or being subject to vibration. The flow details of the rig are given in Table 2.1.

Table 2.1 Water Rig Details

Overall head (maximum)	0.8 m.
Water flow rate (maximum)	3.9 l/s.
Delivery tube dia.	0.05 m.
Reservoir tank capacity	1000 l.
Constant head tolerance	±0.002 m.

2.3 THE MEASURING TECHNIQUE

2.3.1 Introduction

Laser Doppler anemometry was used to measure the mean velocity and normal stress distributions within the flow. This technique has the advantage of being non-obtrusive and having an output that is linearly related to instantaneous velocity. Due to the small scale of the model a non-obtrusive technique was essential in order to determine accurately the details within the flow. Other non-obtrusive techniques such as ultra-sonic Doppler frequency devices are designed primarily for determining bulk mean flows and are not suitable for determining turbulence information since they lack accurate spatial resolution. Extensive descriptions of laser Doppler anemometers are given in the literature, see for example Melling (1975), Durst et al (1976), and therefore only a brief description will be given here specifically related to simple measurements in turbulent water flows.

For convenience, the anemometer will be considered as being composed of two systems, optical and signal processing.

2.3.2 The Optical System

The function of the optical system of a laser Doppler anemometer is to produce a frequency signal of light intensity corresponding to the frequency difference between two light waves scattered by moving particles in a medium. Historically, the first such system was a "reference beam" system described by Yeh and Cummins (1964) for measurements in a laminar water flow. The method used in the present measurements employed another system known as a "dual beam" or "fringe" system that has been found to be both particularly suited to measurements in water flows and to be easy to use (Durst and Whitelaw 1971). The basis of the dual beam anemometer is the intersection of two equally intense, coherent light beams to form a measuring probe known as the "scattering volume". Rigorously, the scattering volume is a region of interference between two electromagnetic waves producing areas of high and low energy within the region. Rudd (1969) proposed a model of the scattering region, shown as Figure 2.3.1(a) which simulates the scattering region by using light and dark fringes which can be considered to produce a fluctuating light intensity in the presence of a moving particle. A fringe spacing Δx can be determined from the crossing of the light beams, of wave length λ, at an angle 2ψ as follows:

$$\Delta x = \frac{\lambda}{2 \sin \psi} \tag{2.1}$$

As the light intensity of the beams are Gaussian in radial distribution the scattering volume is an ellipsoid in shape with boundaries usually defined as a fraction $(\frac{1}{e^2})$ of the maximum intensity, and shown in Figure 2.3.1(b). A particle passing through the scattering volume with velocity V, in the plane of the minor axes, produces a periodic variation in the scattered light intensity due to the interference of the light beams. The Doppler frequency f_D of the periodic scattered light intensity is given by:

$$f_D = {}^{V}/_{\Delta x} = \frac{2V\sin\psi}{\lambda} \tag{2.2}$$

Hence the velocity of the particle is linearly related to the frequency of the scattered light intensity and the constant of proportionality is uniquely defined by parameters that are independent of the flow. This applies to any light transmitting fluid that contains particles which are assumed to travel at a velocity equal to that of the fluid. It has been found that the natural contaminants found in water lie within a suitable size range for use as particles whose instantaneous velocity faithfully represents that of the water (Melling & Whitelaw 1973).

The elements of the optical system used for the present measurements are shown in Figure 2.3.2. and may be categorised into, a light transmission section, which forms the intersecting light beams and the light collection section, which collects the scattered periodic light intensity information and converts this to an electronic frequency signal for further processing. As the information is collected on the opposite side of the test section to the transmitting optics the whole system is known as being in a "forward scattering" mode. Light intensity information may be collected on the same side as the transmitting optics in the "backward scattering" mode however the amount of light scattered back is several orders of magnitude below that of the forward scattered light and is hence very much more difficult to process.

The transmitting section has the following elements:

(i) The laser as a source of light. The advantage of the laser over a thermal light source for Doppler anemometry is its high light intensity and superior spatial coherence. The instrument used for the measurements was a 5mW He-Ne laser with a light wave length of 632.8nm. The light beam was focussed using a short focal length lens to form a "beam waist".

(ii) In order to split the single beam of the laser into two beams use was made of a circular diffraction grating as described for example by Stevenson (1970).

This is not the most accurate method of splitting the beam as other methods, such as purposely constructed beam splitters using high quality prisms, do not suffer from as much light attenuation or inaccuracies which accrue from imperfections in the manufacture of gratings. However, its advantage is that as well as splitting a beam it can also be made to rotate and therefore provide a simple method of biasing the Doppler frequency. The desirability of biasing the Doppler frequency is to establish an unambiguous datum when measuring in turbulent recirculating flows where a velocity component may vary in magnitude and direction and the local turbulence intensity is high (>30%). The reasons for biasing or "shifting" the Doppler frequency are shown in Figures 2.3.3. A velocity probability distribution at a particular location in a flow is shown in Figure 2.3.3(a) which has a low mean value and a variance of sufficient magnitude such that there is a probability of both positive and negative instantaneous velocities occurring. The corresponding frequency probability distribution, without frequency shift, is shown in Figure 2.3.3.(b) where, due to the scalar properties of frequency information (i.e. the impossibility of a negative frequency) the frequencies corresponding to the negative part of the velocity probability distribution are added to those of the positive part of the velocity probability distribution. Hence Figure 2.3.3(a) could not be constructed from the unshifted frequency probability distribution of Figure 2.3.3(b);

this result has been shown experimentally by Durst et al (1974). By rotating the diffraction grating at a fixed steady speed, and by knowing the number of lines N on the grating, a predetermined shift frequency f_s may be added to the Doppler frequency to provide an unambiguous probability distribution as shown in Figure 2.3.3(c). The shift frequency f_s is determined from:

$$f_s = kN\omega \qquad (2.3)$$

where k = 0, 1, 2 .... known as the order of the beams (Figure 2.3.3(d)). The angle at which the split beams emerge ϕ_k and their relative intensity to the zeroth order beam are proportional and inversely proportional to the order of the beams chosen i.e.:

$$\phi_k = \sin^{-1}\left(\frac{k\lambda}{s}\right) \qquad (2.4)$$

where s is the distance between the lines of the grating and the intensity of the first order beams is 57% of the zeroth order beam intensity (Durst et al, 1976).

(iii) The transmitting lens focusses the divergent light beams, emerging from the diffraction grating, to form the scattering volume.

The collecting section, Figure 2.3.2 , comprises:

(i) The collecting lens which focusses a magnified image of the scattering volume on a mask placed in front of the photomultiplier tube so as to prevent signals from different particles contributing towards the photomultiplier signal.

(ii) The pinhole drilled in the mask in front of the photomultiplier tube reduces the amount of the scattering volume seen by the photomultiplier. This smaller volume is termed the measuring volume.

(iii) The photomultiplier converts the light frequency information into electronic frequency signals. This consists of low noise amplification of the electronic signal, caused by the reception of photons on the surface of the photocathode, to a level suitable for signal processing.

The optical geometry of the collecting system is concerned with the careful matching of each component in order to enhance the signal to noise ratio. For example the pinhole diameter d is chosen according to Durst et al (1976):

$$d_{ph} = \frac{N_{ph} M \lambda}{2 \sin \psi} \tag{2.5}$$

where N_{ph} is the number of fringes observed by the photomultiplier and M is the magnification of the collecting lens (l_2/l_1). It has been recommended (Durst et al 1976) that the optimum value of N_{ph} is about 80% of the total number of fringes in the scattering volume. The components and important parameters of the optical system used for the measurements are given in Tables 2.2(a) and 2.2(b).

Table 2.2(a) Optical System Components

Component	Make	Specification
Laser	Spectra-Physics	Power: 5mW Wavelength: 632.8nm He-Ne Beam Dia:0.65mm at $1/e^2$ points Beam Divergence: 1.7 milliradians at $1/e^2$ points
Diffraction grating	O.M.T.(Optics) Ltd.	(see Table 2.4)
Lenses		Transmitting: 150 mm plano-convex Collecting: 100 mm bi-convex

Table 2.2(b) Calculated Optical System Parameters

Number of fringes observed on oscilloscope	90
Beam angle	8.2^{0}
Scattering volume diameter ($^1/e^2$ intensity)	32.7 μm
Scattering volume length ($^1/e^2$ intensity)	230 μm
Fringe spacing	2.23 μm
Velocity to Frequency conversion	2.23 m/s.MHz

2.3.3 The Signal Processing System

The function of the signal processing system of a laser Doppler anemometer is to process the Doppler signal produced, via the photomultiplier, by the optical system into a form whereby it may be statistically analysed. A typical signal from the photomultiplier is shown in Figure 2.3.4 and displays the following characteristics:

(i) The signal frequency within each envelope is linearly proportional to the instantaneous velocity of the particle passing through the measuring volume.

(ii) The envelope size is a function of the size and position (within the measuring volume) of the particle.

(iii) The signal is discontinuous and has a "drop out rate" which is defined as the ratio of time without signal to total time.

(iv) The signal carries noise contributions from both the optical system and photomultiplier (shot noise).

The range of electronic devices that are capable of processing this type of signal includes: frequency analysers, frequency counters, frequency trackers, filterbanks and photon correlators. The details of each of these means of processing are described in Durst et al (1976) as are their respective advantages and disadvantages. In turbulent water flows the most convenient method of signal processing is by using a frequency tracker and this was used for all measurements. The general characteristics of a frequency tracker when used for measuring in water flows are:

(i) The output form is a real time demodulation of the photomultiplier frequency signal in voltage and is therefore suitable for further statistical processing.

(ii) The input signal is required to have a low drop out rate. Although frequency trackers are designed to detect signal drop out and to hold the previous measured frequency, high drop out rates bias any further statistical processes such as true integration to determine the mean frequency. The drop out rate in water flows is not normally significant, however, being usually of the order of 2%.

(iii) The maximum turbulence intensities ($\sqrt{\overline{f_D^2}}/\bar{f}_D$) that can be tracked without frequency shifting is usually limited to about 30%. This is due to limitations in tracking range, dynamic response and slew rate. A frequency tracker incorporates manually selected frequency ranges in discrete steps within its total frequency range and each "subrange" has a high and low limit which may be exceeded when tracking a signal with a high R.M.S. ($\sqrt{\overline{f^2_D}}$) fluctuation. The rate at which the tracker can follow a highly fluctuating signal is also limited by its dynamic response and maximum slew rate (i.e. the maximum rate of change of frequency with time that can be followed). These limitations can be usually avoided by using optical frequency shifting to reduce the overall "turbulence intensity" to less than 30% i.e.:

$$\frac{\sqrt{\overline{\bar{f}_D^2}}}{\bar{f}_D + f_s} < \frac{\sqrt{\overline{\bar{f}_D^2}}}{\bar{f}_D} \qquad (2.6)$$

It is possible for the analogue voltage output from a frequency tracker to be suitably digitised using an analogue-to-digital interface and the results statistically analysed by digital computer on-line (mainframe, mini- and micro-computer configurations are now common). However, for simple statistical quantities, such as those used in the measurements, additional electronic processing by a true integrator (for mean velocity) and an R.M.S. meter are sufficiently adequate. A schematic diagram of the processing equipment is given in Figure 2.3.4 , including the wave forms of the Doppler signal at each stage, and the overall characteristics and manufacture of each component is summarised in Table 2.3.

Table 2.3 The Signal Processing Equipment

Component	Make	Specifications
Photomultiplier	E.M.I.	Type 9558B
Frequency tracker	Cambridge Consultants Ltd.	Range: 100 Hz - 10 MHz (5) Slew Rate: 3×10^{-3} (CC01)
Cathode Ray Oscilloscope	Tektronix	Type 7603
True Integrator	DISA	Type 52B30
R.M.S. Voltmeter	DISA	Type 55D35 Frequency range 0.1 Hz - 400 KHz
Digital Voltmeter	Solatron	

2.3.4 The Method of Measurement

In order to traverse each of the models with the laser anemometer the optical components and the photomultiplier were mounted on a rigid mild steel optical bench incorporating two parallel, stainless steel bars which in turn was bolted to a three-dimensional traversing bed. The transmitting and collecting lenses, and the photomultiplier were each mounted in holders featuring both translational and rotational adjustment. The alignment procedure, an essential process for the minimisation of optical noise, was carried out by ensuring the laser beam parallel and centrally located on the optical bench and by placing each optical component in the position indicated (Figure 2.3.2). The three-dimensional traversing bed was adjusted so as to place the centre line of the light path at right angles to the test section using the symmetry of the light beam reflections to ensure perpendicularity. Final adjustments to the position of the photomultiplier were made by viewing the signal output directly on the oscilloscope display.

2.4 LIMITATIONS IN ACCURACY OF THE MEASURING TECHNIQUE

2.4.1 Introduction

The measurements made with a laser-Doppler anemometer contain inherent errors which can accrue from the incompatibility between the dimensions of the scattering volume and the length scales of the physical processes the fluid undergoes within it. These errors increase the variance of the Doppler frequency probability distribution, and hence increase the measured values of normal stress. For this reason they are known as "broadening errors". The most significant of these errors are: finite transit time broadening, mean velocity gradient broadening and instrument broadening; each of these are briefly discussed.

2.4.2 Finite Transit Time Broadening

Finite transit time broadening is a consequence of the phase incompatibility between particles entering the scattering volume and particles leaving during the formation of a single Doppler signal (Figure 2.4.1 a). This occurs because the Doppler signal has a finite time rate of formation proportional to the scattering volume dimension in the direction of the flow. Melling (1975) has shown that the broadening error in the RMS of the velocity fluctuations σ_F is proportional to the Doppler frequency f_D and may be evaluated as follows:

$$\frac{\sigma_F}{f_D} = \frac{1}{2\sqrt{2}\pi N_f} \tag{2.7}$$

which is in accordance with othe workers (e.g. George and Lumley 1973 and Edwards et al 1971, 1973). The maximum value of σ_F encountered in the measurements was 0.13% and determined by calculation.

2.4.3 Velocity Gradient Broadening

Velocity gradient broadening occurs when a mean velocity gradient exists across the scattering volume, and is only significant near walls; this may occur in both laminar and turbulent flows (Figure 2.4.1 b). Particles moving through the scattering volume at different lateral locations scatter light at varying frequencies independently of the turbulent velocity fluctuations. A simple method ofevaluating the broadening error has been proposed by Melling (1975) and agrees with the more rigorous equation of Berman and Dunning (1973) for small scattering angles. The error due to velocity gradient broadening σ_g is evaluated as follows:

$$\frac{\sigma_g^2}{\bar{f}_D^2} = \frac{dy^2}{V_o^2}\left(\frac{dV}{dy}\right)_o^2 \qquad (2.8)$$

The maximum value encountered in the measurements was 0.5%.

2.4.4 Instrument Noise Broadening

The main contribution towards instrument noise broadening comes from the rotating diffraction grating. The specifications of the diffraction grating used are given in Table 2.4.

Table 2.4 Specifications of the Rotating Diffraction Grating

Make	O.M.T. (Optics) Ltd.
No. of lines	18,000
Diameter	152mm
Concentricity	± 25μm
Surface flatness	6 μm
1st order beam attenuation	43%
Rotational speed range	5-5,000 rpm ± 1%

Deterioration in the quality of signals obtained with a rotating diffraction grating as compared to, for example, a beam splitter, stem mainly from imperfections in the manufacturing process (usually bleaching). Although mounted on a heavy brass flywheel and located with precision needle bearings the inherent vibrations cause errors which increase with rotational speed. An overall estimate of the broadening error σ_i

caused by the grating and random fluctuations in the motor speed has been given (Humphrey 1977) as $\sigma_i \simeq 0.01 f_s$ which corresponds, with the rotational speed used in the measurements, to 2.0%.

2.5 SUMMARY

This chapter has presented the layout and operation of the water flow rig used to supply the model geometries. A simple, dual beam, forward scatter laser anemometer has been described including reference to the layout and geometry of the optics, the mounting and the signal processing equipment. The accuracy of the laser Doppler technique has been discussed as has the more common broadening errors that affect the RMS velocity measurements.

CHAPTER 3

THE CALCULATION PROCEDURE

3.1 INTRODUCTION

The calculation approach is based upon formulating partial differential equations, describing incompressible, constant property flow, into finite-difference equations readily solvable using numerical methods. The formulation and numerical methods have been described in detail by several workers, see for example Gosman and Pun (1973), however, a brief description of each stage is included for completeness and to serve as background to the discussions on assumptions.

3.2 DESCRIPTION OF THE EQUATIONS

3.2.1 The Conservation Equations

The general equations that describe the steady flow of an incompressible, constant property fluid, expressed in Cartesian tensor form, are:

Mass conservation:

$$\frac{\partial U_i}{\partial x_i} = 0 \qquad (3.1)$$

Momentum conservation:

$$\frac{\partial U_i}{\partial t} + \frac{\partial}{\partial x_j}(U_i U_j) = -\frac{\partial p}{\partial x_i} + \nu \frac{\partial^2 U_i}{\partial x_j \partial x_j} \qquad (3.2)$$

Conservation of a Scalar Property:

$$\frac{\partial \Phi}{\partial t} + \frac{\partial}{\partial x_j}(U_j \Phi) = \frac{\partial}{\partial x_j}\left(\Gamma_\phi \frac{\partial \Phi}{\partial x_j}\right) + S_\phi \qquad (3.3)$$

These equations represent a closed set and, with the provision of boundary conditions and a suitable formulation into a numerical scheme, may be solved for both laminar and turbulent flows. However, in turbulent flows, fluctuations in the dependent variables have time and length scales which cover a range of several orders in magnitude for high Reynolds number flows. Direct use of eqns. 3.1 - 3.3 would necessitate the discretisation of the calculation domain into control volumes of the same order as the smallest length scales. For most engineering processes, involving turbulent flow, the necessary computational power required for a calculation, using this approach, is not available at present. The standard approach is to decompose eqns. 3.1 - 3.3 into mean and fluctuating components and to time average. For constant density flows the unweighted (density) decomposition and averaging are represented by:

$$U_i = \bar{U}_i + u_i \;;\; \Phi = \bar{\Phi} + \phi \text{ etc.}$$

where $$\bar{U}_i = \lim_{t\to\infty} {}^{1}/_{\tau} \int_{t_o}^{t_o+\tau} U_i \, dt$$

and $$\overline{u_i} = 0$$

The eqns. 3.1 - 3.3 may be re-written in averaged form to give:

$$\frac{\partial(\bar{U}_i)}{\partial x_i} = 0 \qquad (3.4)$$

$$\bar{U}_j \frac{\partial(\bar{U}_i)}{\partial x_j} = -\frac{1}{\rho}\frac{\partial \bar{p}}{\partial x_i} + \frac{\partial}{\partial x_j}\left(\nu \frac{\partial \bar{U}_i}{\partial x_j} - \overline{u_i u_j}\right) \qquad (3.5)$$

$$\frac{\partial}{\partial x_j}(\bar{U}_j \bar{\Phi}) = \frac{\partial}{\partial x_j}\left(\Gamma_\phi \frac{\partial \bar{\Phi}}{\partial x_j}\right) + S_\phi \qquad (3.6)$$

The decomposition and averaging procedure, due to the non-linearity of eqns. 3.1 - 3.3, produces a set of equations (3.4 - 3.6) that are no longer closed. Closure of the equations involves the determination of the Reynolds stress tensor $\overline{u_i u_j}$ which is dealt with in the next section.

3.2.2 The Turbulence Model

The exact transport equation for the Reynolds stress may be written, in general form (Hanjalic 1970), as follows:

$$\frac{D\,(\overline{u_i u_j})}{Dt} = (\overline{u_i u_k}\,\frac{\partial \bar{U}_j}{\partial x_k} + \overline{u_j u_k}\,\frac{\partial \bar{U}_i}{\partial x_k}) \qquad \text{(generation)}$$

$$- \frac{\partial}{\partial x_k}(\overline{u_i u_j u_k}) - \frac{1}{\rho}\,(\frac{\partial \overline{p u_i}}{\partial x_j} + \frac{\partial \overline{p u_j}}{\partial x_i}) \qquad \text{(turbulent diffusion)}$$

$$+ \overline{p\,(\frac{\partial u_i}{\partial x_j} + \frac{\partial u_j}{\partial x_i})} \qquad \text{(pressure rate of strain)}$$

$$+ \overline{\nu(u_i\,\frac{\partial^2 u_j}{\partial x_k^2} + u_j\,\frac{\partial^2 u_i}{\partial x_k^2})} \qquad \text{(viscous action)} \quad (3.7)$$

The solution of this equation depends upon the knowledge of the triple correlation ($\overline{u_i u_j u_k}$) which, again, if formulated into a transport equation would require knowledge of even higher order correlations. Assumptions and models are, therefore, necessary to close eqns. 3.4 - 3.6 at some level which must depend upon the complexity of the whole calculation.

Calculation of $\overline{u_i u_j}$, with a second order closure, using eqn. 3.7 and a model for the triple correlation (which requires the calculation of a further transport equation for the turbulence energy dissipation rate $\varepsilon \equiv \nu\,\overline{\frac{\partial^2 u_i}{\partial x_j^2}}$) involves seven transport equations for a three-dimensional flow and is, therefore, computationally very expensive.

Selection of a first order closure of eqns. 3.4 - 3.6, where eqn. 3.7 is not directly solved, relies upon the "eddy viscosity" concept (Boussinesq,1877) where the Reynolds stress is related to the mean rate of strain via:

$$- \overline{u_i u_j} = \nu_t\,(\frac{\partial \bar{U}_i}{\partial x_j} + \frac{\partial \bar{U}_j}{\partial x_i}) - \frac{2}{3}\,k\;\delta_{ij} \qquad (3.8)$$

where ν_t is an isotropic eddy viscosity and δ_{ij} is the Kronecker delta.

The Reynolds stress, therefore, depends upon a prescription of ν_t which varies throughout the calculation domain. The variation is assumed to follow the Prandtl-Kolmogorov formula:

$$\nu_t = C_\mu k^{\frac{1}{2}} \ell \tag{3.9}$$

where C is an empirical constant, k is the kinetic energy of turbulence ($\equiv \frac{\overline{u_i^2}}{2}$) and ℓ is a length scale characterising the energy-containing motions.

A transport equation for k may be derived (Kolmogorov 1942) from the momentum equation (3.2) and has been modelled by Rodi (1970) as:

$$\begin{aligned} \bar{U}_i \frac{\partial k}{\partial x_i} &= \frac{\partial}{\partial x_i}\left(\frac{\nu_t}{\sigma_k}\frac{\partial k}{\partial x_i}\right) && \text{(turbulent diffusion)} \\ &+ \nu_t \frac{\partial \bar{U}_i}{\partial x_j}\left(\frac{\partial \bar{U}_i}{\partial x_j} + \frac{\partial \bar{U}_j}{\partial x_i}\right) && \text{(generation)} \\ &- \nu\, \overline{\left(\frac{\partial u_i}{\partial x_j}\right)^2} && \text{(viscous action)} \end{aligned} \tag{3.10}$$

The viscous action term in eqn. 3.10 is defined in mean quantities by:

$$\varepsilon \equiv \nu\, \overline{\left(\frac{\partial u_i}{\partial x_j}\right)^2} \tag{3.11}$$

where ε is the rate of dissipation of turbulence energy. The length scale may be related to ε (Jones 1971) by:

$$\varepsilon = k^{3/2}/\ell \tag{3.12}$$

so that the equation (3.9) becomes:

$$\nu_t = c_\mu k^2/\varepsilon \tag{3.13}$$

A transport equation for ε has been modelled from exact derivations (Harlow and Nakayama 1968) and discussed (Rodi 1970), the equation gives:

$$\bar{U}_i \frac{\partial \varepsilon}{\partial x_i} = \frac{\partial}{\partial x_i} \left(\frac{\nu_t}{\sigma_\varepsilon} \frac{\partial \varepsilon}{\partial x_i} \right) + \varepsilon/_k \left[C_1 \nu_t \frac{\partial \bar{U}_i}{\partial x_j} \left(\frac{\partial \bar{U}_i}{\partial x_j} + \frac{\partial \bar{U}_j}{\partial x_i} \right) - C_2 \varepsilon \right] \qquad (3.14)$$

where C_1 and C_2 are empirical coefficients. The full set of empirical coefficients is given below:

$$C_\mu = 0.09; \quad C_1 = 1.44; \quad C_2 = 1.92; \quad \sigma_k = 1.0; \quad \sigma_\varepsilon = 1.3.$$

The two modelled equations 3.10 and 3.14 constitute the high Reynolds number version of the k-ε model. Although a low Reynolds number version exists (Jones and Launder 1973) it incurs a high penalty in increased grid fineness due to the necessity of calculating in the laminar region). The high Reynolds number version requires special treatment at wall boundaries. The regions immediately adjacent to the walls, where the dependent variables undergo rapid changes and the flow is laminar, have to be bridged via "wall functions" which are based upon physical reasoning and empirical data.

The relationship between velocity and shear stress near a wall is approximated by using the "law of the wall" (Schlichting,1968) where:

$$U = \frac{({}^{\tau_w}/_{\rho})^{\frac{1}{2}}}{\kappa} \ln \left(\frac{E \rho y ({}^{\tau_w}/_{\rho})^{\frac{1}{2}}}{\mu} \right) \qquad (3.15)$$

κ and E are empirical constants and y is the normal distance from the wall. The application of eqn. 3.15 to the boundary conditions for the dependent variables is described in section 3.2.4.

3.2.3 The Finite-difference Formulation

The finite-difference forms of the partial differential equations governing the flow are derived with reference to a suitable discretised calculation domain which extends to the boundaries of the flow. The method of discretisation uses a "staggered" grid where flow variables: velocity, pressure, etc. are stored at nodal points within the grid. The staggered arrangement allows pressures and scalar quantities (i.e.

turbulence kinetic energy and energy dissipation rate) to be stored at nodes placed between the velocity storage nodes thereby facilitating the formulation of the finite-difference equations. However, it also necessitates the adoption of different control volumes for the velocities and pressure (Fig. 3.1).

The finite-difference equations express the laws of conservation (transport) for each variable within a cell. For a general variable ϕ the finite-difference equation is derived by integrating eqn. 3.6 over a control volume, which in steady, two-dimensional form becomes:

$$\int_{vol}\left[\frac{\partial(\rho\ \bar{U}\phi)}{\partial x}+\frac{\partial(\rho\ \bar{V}\phi)}{\partial y}\right]\ dvol-\int_{vol}\left[\frac{\partial}{\partial x}\left(\Gamma_\phi\ \frac{\partial\phi}{\partial x}\right)+\frac{\partial}{\partial y}\left(\Gamma_\phi\ \frac{\partial\phi}{\partial y}\right)\right]dvol$$

$$=\int_{vol}\left[S_\phi\right]dvol \qquad (3.16)$$

or, in finite-difference form:

$$A_e\ \dot{q}_e\ \left[(1-F_e)\ \phi_E+F_e\ \phi_p\right]\ -A\ \ \dot{q}_w\ \left[F_w\ \phi_w+(1-F_w)\ \phi_p\right]$$

$$+A_n\ \dot{q}_n\ \left[(1-F_n)\ \phi_N+F_n\ \phi_p\right]-A_s\ \dot{q}_s\ \left[F_s\ \phi_s+(1-F_s)\ \phi_p\right]$$

$$=S_u^{\phi}+S_p^{\phi}\ \phi_p \qquad (3.17)$$

where A_e is the EAST face area of the control volume

$\dot{q}_e$ is the EAST face mass flux (= $\rho_e\bar{U}_e$)

F_e is the EAST weighting factor for the differencing.

The type of differencing used is the "hybrid" scheme (Spalding, 1972) and consists of a combination of upstream and central differences, either being chosen,on the basis of the ratio of convective flux to diffusive flux (Peclet No.), i.e.

$$F_e = \frac{1}{2} + \frac{1}{Pe_e} \quad \text{for } |Pe_e| < 2 \qquad \text{(central)}$$

$$F_e = \begin{cases} 1 & \text{for } Pe_e \geqslant 2 \\ 0 & \text{for } Pe_e \leqslant -2 \end{cases} \qquad \text{(upstream)} \qquad (3.18)$$

$$\text{where } Pe_e = \frac{\dot{q}_e \Delta_x}{\Gamma_e}$$

The source term given in eqn. 3.17 has been integrated over the control volume and linearised; the values S_u^{ϕ} and S_p^{ϕ} are deduced from physical input to the calculation (e.g. wall friction, kinetic energy generation etc.). The transport equation for ϕ in finite-difference form (eqn. 3.17) may be rearranged and, employing the continuity equation yields:

$$\left(\sum_{i=1}^{4} a_i^{\phi} - S_p^{\phi} \right) \phi_p = \sum_{i=1}^{4} a_i^{\phi} \phi_i + S_u^{\phi} \qquad (3.19)$$

where $\sum_{i=1}^{4}$ is the summation over neighbouring cells (north, south, east and west).

The transport equation for a velocity $\overline{U}$ is expressed as:

$$\left(\sum_{i=1}^{4} a_i^{u} - S_p^{u} \right) \overline{U}_p = \sum_{i=1}^{4} a_i^{u} \overline{U}_i + A_w (p_w - p_p) \qquad (3.20)$$

where the pressure gradient acting upon $\overline{U}_p$ enters the finite-difference equation as a "source" term. The determination of pressure is dealt with in section 3.2.5.

3.2.4 The Boundary Conditions

The transport equations 3.19 and 3.20 are closed and may be solved once the boundary conditions have been specified. The specifications vary according to the type of boundary and the dependent variable under consideration.

(i) Inlet Boundary

The values for each variable are assigned for each grid node situated at the plane of entry. These are supplied from some knowledge of the practical situation which is being modelled e.g. from experimental measurement.

(ii) Symmetry Plane

At a symmetry plane, or an axis of symmetry, the diffusion and convection fluxes are zero. For the axis of symmetry at y=0, for example:

$$\Gamma_\phi \Big|_{y=0} = 0$$

and $$\frac{\partial \phi}{\partial y}\Big|_{y=0} = 0$$

(iii) Cyclic Boundary

If the three dimensional calculation domain exhibits a periodic uniformity about an axis as shown in Fig. 3.2a then cyclic boundary conditions may be specified at the axes of the periodic section thereby reducing the size of the calculation domain. Cyclic boundary conditions imply (Fig. 3.2b) that:

$$\phi_1 = \phi_m$$

$$\phi_2 = \phi_{m+1}$$

which may be found by elimination within the solution procedure (section 3.2.5).

(iv) Solid Wall Boundary

At a solid wall boundary all velocities, the turbulence kinetic energy and the gradient of the energy dissipation are all zero viz.:

$$\overline{U} = \overline{V} = k = \frac{\partial \varepsilon}{\partial y} = 0. \qquad (3.21)$$

for a wall parallel to the x-direction. However, in turbulent flow, where the transport equations for k and ε are not solved within the viscous sublayer region adjacent to the wall, the influence of the wall is simulated by using wall functions outlined in section 3.2.2.

The wall functions are specified at nodes directly adjacent to the wall by modifying the exchange coefficients Γ_ϕ for each variable:

a) Velocity

For a velocity parallel to a solid wall boundary the "law of the wall" (eqn. 3.15) is used (if the proximity of the near-wall node allows a logarithmic velocity profile to be physically accurate) to specify a modified exchange coefficient i.e.

$$\Gamma_\phi = \frac{\mu \kappa y^+}{\ln(Ey^+)} \qquad (3.22)$$

where $y^+ \simeq \dfrac{\rho k^{1/2} C_\mu^{1/4} \Delta y}{\mu}$

For $y^+ > 11.5$, where the turbulent wall function is valid* the source term for the momentum equation for the velocity parallel to the wall is modified to:

$$S_u^\phi + S_p^\phi \phi_p - \frac{\Gamma_\phi A}{\Delta y} \qquad (3.23)$$

b) Turbulence Kinetic Energy

The generation of kinetic energy in the wall region is by use of a modified form of the generation term in equation 3.10 and is incorporated into the source term in approximate form:

---

* i.e. the three zones of the wall region (Hinze 1959): viscous sublayer ($0<y^+\leqslant 5$), buffer zone ($5<y^+\leqslant 30$), and inertial sublayer ($30<y+\leqslant 400$) are replaced by two zones: viscous ($0<y^+\leqslant 11.5$) and inertial ($11.5<y+< 400$)

$$S_u^k = \frac{C_\mu^{\frac{1}{4}} \rho k \bar{U}}{\Delta y \ln(Ey^+)} \qquad (3.24)$$

c) Energy Dissipation Rate

The near wall values of energy dissipation rate are prescribed using the definition of length scale near a wall:

$$\ell \equiv \frac{k^{3/2}}{\varepsilon} = C_\mu^{-3/4} \kappa \Delta y$$

Hence $$\varepsilon_w = \frac{C_\mu^{3/4} k^{3/2}}{\kappa \Delta y}$$

ε_w is fixed by altering the source term (eqn. 3.17) as follows:

$$S_u^\varepsilon = \alpha \varepsilon_w$$

$$S_p^\varepsilon = -\alpha$$

where α is a large number e.g. 10^{30} so that, when solved, all other terms in equation 3.19 are negligible, this is discussed in (v) below.

(v) Solid Boundaries within the Calculation Domain

The incorporation of solid boundaries within the calculation domain is accomplished by modifying the finite-difference equations so that, when solved, the result is appropriate to the value that the dependant variable would attain inside a solid boundary. For example all fluid velocities are zero within a wall, as is the turbulence kinetic energy. Pressure influences, for a steady calculation are assumed not to affect the geometry of the physical domain. The method used is to re-write eqn. 3.19 as:

$$\left(\sum_{i=1}^{4} a_i^\phi + \alpha \right) \phi_p = \sum_{i=1}^{4} a_i^\phi \phi_i + \alpha\phi \qquad (3.25)$$

where ϕ_w is zero or ε_w (in the case of energy dissipation rate) and α is a very large number ($\to\infty$). For example, the solution to (3.25), for a velocity located at a node P within a wall, would be:

$$\phi_p = \frac{\Sigma a_i^{\phi} \phi_i}{\Sigma a_i^{\phi} + \alpha} \simeq \frac{1}{\alpha}$$

It is necessary also to specify the wall functions for these internal walls in the same manner as for calculation domain boundary walls.

(vi) Outlet Boundary

At an outlet boundary it is assumed that zero gradient conditions exist in the outflow direction normal to the outlet plane.

3.2.5 The Solution of the Finite-difference Equations

The method of solving the finite-difference equations uses an implicit, iterative technique after Chorin (1968) and Harlow and Amsden (1971). The technique makes successive adjustments to the velocity and pressure fields by solving the conservation equations (in finite-difference form) for momentum and continuity (pressure-correction). The sequence for a two-dimensional calculation is, briefly, as outlined below:

(i) Apply the momentum equation to each velocity component using coefficients (diffusive, convective) and source terms determined from initial guesses or a previous iteration. For example, the solution to equation (3.20) is:

$$\bar{U}_p^* = \left[\sum_{i=1}^{4} a_i^u \, \bar{U}_i^* + A_w \, (p_w^* - p_p^*) \right] / \left(\sum_{i=1}^{4} a_i^u - S_p^u \right) \qquad (3.26)$$

where * denotes the "uncorrected" form of the variable. Similarly, for the other velocity:

$$\bar{V}_p^* = \left[\sum_{i=1}^{4} a_i^v \, \bar{V}_i^* + A_s \, (p_s^* - p_p) \right] / \left(\sum_{i=1}^{4} a_i^v - S_p^v \right) \qquad (3.27)$$

(ii) The extent to which the $\overline{U}^*$ and $\overline{V}^*$ fields do not satisfy cellwise continuity gives rise to a "mass source" S^P such that, applying the continuity equation (3.4):

$$S^P = \rho_e A_e \overline{U}_E^* - \rho_w A_w \overline{U}_P^* + \rho_n A_n \overline{V}_N^* - \rho_s A_s \overline{V}_P^* \qquad (3.28)$$

In order to reduce S^P to zero an equation may be written using "velocity corrections" $\overline{U}'_p$ and $\overline{V}'_p$ i.e.

$$-S^P \equiv \rho_e A_e \overline{U}_E - \rho_w A_w \overline{U}_P + \rho_n A_n \overline{V}_N - \rho_s A_s \overline{V}_S \qquad (3.29)$$

where $\overline{U}_p \simeq A_w (p'_w - p'_p)/(\Sigma a_i^u - s_p^u)$ (3.30)

$\overline{V}_p \simeq A_s (p'_s - p'_p)/(\Sigma a_i^v - S_p^v)$ (3.31)

A "pressure-correction" equation may be formed by substitution of eqns. (3.30), (3.31) into eqn. 3.29 to give:

$$\left(\sum_{i=1}^{4} a_i^p\right) p'_p = \sum_{i=1}^{4} a_i^p \, p'_i + S^p \qquad (3.32)$$

where $a_n^p = A_n^2 \rho_n/(\Sigma a_{i_N}^v - s_N^v)$ etc.

The solution of eqn. (3.32) may be used to correct the $\overline{U}^*$, $\overline{V}^*$ and p^* fields to give cell-wise continuity via:

$$\overline{U}_p = \overline{U}_p^* + \overline{U}'_p$$

$$\overline{V}_p = \overline{V}_p^* + \overline{V}'_p$$

$$p_p = p_p^* + p'_p$$

(iii) The convection and diffusion coefficients and source terms are determined for the scalar equations (turbulence kinetic energy and energy dissipation rate) and their respective equations solved.

(iv) The coupling between the scalar fields and the velocity fields is completed for subsequent iterations via the equation for ν_t (eqn. 3.13).

The equation for each variable, including the pressure-correction equation, reduces to the same algebraic form, which in two dimensions is:

$$\phi_p = \sum_{i=N,S,E,W} a_i \phi_i + b_p \qquad (3.33)$$

The method used to solve (3.33) is based on the alternating-direction-implicit scheme (ADI) proposed by Peaceman and Rachford (1955) where, in two-dimensions, one co-ordinate direction is treated implicitly whilst the coefficients for the other direction (the "off-line" coefficients) are formed from the most "recent" iteration. The sequence for the solution of (3.33) is in two steps which may be repeated for higher accuracy (usually only in the case of the pressure-correction equation); the steps are:

(i) $$\phi_p^{(1)} = a_N \phi_N^{(1)} + a_S \phi_S^{(1)} + \left[\sum_{i=E,W} a_i \phi_i^{(o)} + b_p \right] \qquad (3.34)$$

(ii) $$\phi_p^{(2)} = a_E \phi_E^{(2)} + a_W \phi_W^{(2)} + \left[\sum_{i=N,S} a_i \phi_i^{(1)} + b_p \right] \qquad (3.35)$$

The actual solution of (3.34) and (3.35) is by a form of Gaussian elimination called the Tri-diagonal Matrix Algorithm (TDMA) which enables the solution of a set of linear, simultaneous, algebraic equations. These relate the values of ϕ at adjacent points along a line by:

$$\phi_i = X_i \phi_{i+1} + Y_i \phi_{i-1} + Z_i \qquad (3.36)$$

where $1 \leqslant i \leqslant N$ and $X_N = Y_1 = 0$

By defining:

$$X'_i \equiv \frac{X_i}{1 - Y_i X'_{i-1}}$$

and $$Y'_i \equiv \frac{Y_i Y'_{i-1} + Z_i}{1 - Y_i X_{i-1}}$$

(3.36) becomes:

$$\phi_i = X'_i \phi_{i+1} + Y'_i \qquad (3.37)$$

allowing ϕ_i to be solved by successive substitution, the recurrence process starting with:

$$X'_i = Y'_i = 0.$$

3.3 LIMITATIONS OF THE CALCULATION APPROACH

The method of calculating turbulent flows outlined in the previous sections, has been applied to different flow situations by many workers. The ability of the method to accurately predict all flow variables, when compared to experimental data, has been shown to be limited for both two and three-dimensional, turbulent, recirculating flows (e.g. Vasilic-Melling 1977 and Durst and Rastogi 1979). The two main areas of criticism have centred upon the turbulence model and the finite-difference scheme used in the calculation procedure. Both of these points are discussed.

3.3.1 Limitations of the Turbulence Model

The most extensively tested turbulent, recirculating flows have been simple geometries where the recirculation regions are largely unconfined and developing wake regions have constituted a major part of the investigation (for example: Pope and Whitelaw 1976, Vasilic-Melling 1977, Durst and Rastogi 1979). The consistent under-prediction of recirculation lengths and peak turbulence kinetic energy levels has been attributed to the k-ε turbulence model and, in particular its inability to account for extra rates of strain imposed by curvature of the streamlines, and physically represent the interaction between the flow and wall boundaries.

The effects of "streamline curvature" in turbulent flows significantly alters the local turbulence structure and, in turn, the development of the mean flow (extensive review Bradshaw 1973). Most experimental investigations have been with two-dimensional curved wall boundary-layers (discussion by Irwin and Arnot-Smith 1975) and it has been observed that turbulent transport diminishes where the angular momentum of the flow increases with radius and vice versa. These effects upon the anisotropy of the normal stresses are not included in the standard k-ε turbulence model where the eddy viscosity concept assumes isotropy. Present knowledge of three-dimensional curved flows, where the plane of streamline curvature does not generally coincide with the plane of mean shear, is still underdeveloped.

Several ad hoc modifications to the k-ε turbulence model have been proposed for two-dimensional flows by some workers, resulting in the desired effect upon the turbulence transport. Launder et al (1977) proposed the modification to the energy dissipation rate equation (eqn. 3.14) decay term $-C_2\varepsilon^2/_k$ so that an increase in angular momentum with radius (i.e. curvature dependence) could increase the local dissipation rate and hence lower the turbulent transport. This modified form was applied to both curved wall boundary-layers and spinning discs. Militzer et al (1977) proposed a curvature dependent modification to the generation term of the kinetic energy equation (eqn. 3.10) so that an increase in angular momentum with radius would reduce the local generation of kinetic energy and have applied it to a flow from twin parallel jets. Leschziner and Rodi (1980) have proposed a modification to the k-ε model using a curvature dependent C_μ, the formulation for which is derived from an algebraic stress model (i.e. a model derived from the transport equations for the normal stresses by neglecting convection and diffusion terms). This modification has been applied to unconfined jet flows from an orifice with an integral baffle. These methods exhibit, for the unconfined flows investigated, better agreement with experiment than the standard k-ε model. However, their universal usage in recirculating flows is open to question due to the widely different methods of achieving the same physical result. Furthermore, the physical uncertainty of the exact behaviour of streamline curvature in three-dimensional flows precludes their use at the present time. For confined flows, where the physical boundaries or conditions dictate, for example, the mean size of the recirculation the defects of the standard k-ε model are not so great.

The other turbulence model related deficiency concerns the wall boundary treatment, which uses the empirically derived "wall function" described in section 3.2.4(iv), originally formulated for two-dimensional boundary-layer flows in the absence of a pressure gradient. These do not adequately describe the interaction between the high Reynolds number part of the flow and the wall for recirculating flows. These simple wall functions are based upon the assumption of a thin region, near the wall, of constant shear stress equal to the wall shear stress and a local velocity distribution as in a couette flow. More rigorous wall functions,have been postulated, for three-dimensional boundary-layer calculations (Van Den Berg 1975), where account is taken of the variation of the shear stress vector near the wall and the local pressure gradient. However, even these are only valid "when the deviations from the simple law are not large". Use of any of these laws for calculations at points involving separation along a wall surface, where they are not valid (Simpson et al 1976) will create errors in local mean velocity gradients through wrongly prescribed shear stress distributions.

3.3.2 Limitations of the Finite-difference Technique

The method of solving the partial differential equations governing the flow (eqns. 3.4-3.6) is by approximating them into algebraic (finite-difference) form. The choice of differencing (relating the flow variable value at a node to values at neighbouring nodes) is not straightforward for dominantly convective flows. The simplest, known as "upstream differencing" estimates the convection by assuming a stepwise variation in the value of a flow variable at the cell face between two nodes, depending upon the direction of the prevailing velocity between them. A more accurate scheme known as "central differencing" assumes a linear variation between two nodes when estimating convection.

Central differencing, however, when used in calculations of highly convective flows, leads to unstable numerical behaviour (Roache 1976). Upstream differencing, although stable in highly convective flows, is prone to an error (proportional to grid node spacing) due to the neglect of the gradient between the two nodes i.e. the estimate of the convecting flux contains a gradient type error in the form of an erroneous diffusional flux or "false diffusion". This false diffusion tends to locally smear the gradients of a flow variable, especially in flows with strong cross-stream gradients, by dominating the true physical diffusion, resulting in misleading predictions. The "hybrid scheme" (Spalding 1972) incorporates both upstream and central differencing, based on a study of their relative performance when compared to the exact solution to a one-dimensional temperature equation. The value of local Peclet number, the ratio of convective to diffusive fluxes, determines which type of differencing is employed in determining the convective flux. However, the weakness of upstream differencing in flows with strong cross stream gradients, namely false diffusion (Raithby 1976) is still prevalent with the hybrid scheme.

Other schemes have been reported which, for the unconfined recirculating flows examined (Militzer et al 1977, Leschziner 1979, Leschziner and Rodi 1980) have given improved accuracy over the hybrid scheme due to the reduction in false diffusion. The "skewed upstream" scheme (Raithby 1976a), although still essentially an upstream formulation, estimates the convection using a spacially weighted mass of the prevailing upstream velocity distribution. Hence the convection is sensitive to upstream and cross-stream velocity gradients improving the accuracy of the spatial distribution of the calculated variable and reducing false diffusion. Another scheme proposed by Leonard (1980) uses a "quadratic" formulation for convection using an extra upstream node which, in simple terms, produces a two term estimation for convection, free of false diffusion. The first is the normal central differencing term, whilst the second comprises an "upstream weighted normal curvature" term which has a stabilizing influence upon the first term. These schemes, although stable, can exhibit small under and overshoots in the solution requiring special care to ensure physically unrealistic values (e.g. negative kinetic energy values) are not produced during convergence. One disadvantage is the greater complexity in specification of boundary conditions and these methods are not readily applicable to geometries with wall boundaries specified within the calculation domain.

3.4 SUMMARY

A description of a finite-difference numerical model has been given with applications to three-dimensional, isothermal, flows. The approximated forms of all the dependant variable equations have been discussed along with assumptions and specification of empirical data required.

CHAPTER 4

A TWO-DIMENSIONAL MODEL WITH ANNULUS

4.1 INTRODUCTION

This chapter describes the measurements and calculations of the flow in a two-dimensional, axisymmetric model of a combustion chamber. This model is the first in a series of three which increase in complexity; each one being used to examine specific features of a combustion chamber flow. The model described in this chapter, although two-dimensional and axisymmetric, simulates some relevant features of practical combustion chambers. These include: primary zone recirculation, the influence of the annulus on the flow in the flame tube and the behaviour of the primary jets after impingement.

The model geometry and basic flow pattern structure is first described before examining the measurements of axial mean velocity and normal stress obtained. The sections following this deal with the accuracy of the numerical calculations when composed to measurement and the behaviour of other calculated variables such as: pressure, radial velocity and kinetic energy. The influence of modifications to the geometry is examined, using further calculations, before summarising this aspect of the work in the last section.

4.2 THE MODEL DETAILS

4.2.1 The Geometry

The two-dimensional, axisymmetric geometry is shown in Figure 4.2.1. It consisted of three, transparent cast acrylic tubes; the two smaller diameter tubes were held in line (one upstream of the other with a gap between) and concentrically within the third larger diameter tube. The upstream tube was closed at one end and held on a brass sting. The downstream tube was located by two rings which also acted as blockages to the annular passage further downstream. The whole test section was located in the water flow rig described in Chapter 2. Preliminary work included flow visualisation the results of which are described in the next section.

4.2.2 The Flow Pattern

The general flow pattern is shown schematically in Figure 4.2.2. From flow visualisation using hydrogen bubbles, produced by electrolysis well upstream of the test section, the following main characteristics were observed:

(i) The water flows around the outside of the upstream tube into the annulus and through the gap between the tubes to the centre of the test section.

(ii) The rings, which block the downstream annular passage, retain a large, slow moving recirculation region within the annulus.

(iii) The upstream closed tube retains a large toroidal recirculation region.

(iv) At the upstream edge of the downstream tube the flow detaches to form a small separation region; reattachment occurs a small (less than one gap width) way downstream.

(v) The flow, once downstream of the small separation region described above, continues to develop.

(vi) The Reynolds number of the flow based upon the average velocity and the diameter of the downstream tube was 4.4×10^4.

After flow visualisation the mean axial velocity and normal stress distributions were measured using laser-Doppler anemometry; these are described in the next section.

4.3. THE MEASUREMENTS

The measurements of mean axial velocity $\overline{U}$ and the normal stress $\overline{U^2}$ were taken using the laser Doppler anemometry and signal processing equipment described in Chapter 2.

The position of the measuring locations are indicated in Figure 4.3.1 and comprise: fourteen axial locations (three upstream of the gap, three within the gap and eight downstream) and fifteen radial points at each axial location. At some locations measurements were taken over the complete diameter to ascertain two-dimensionality of the flow. For example, at $^x/D = 3.79$ the maximum asymmetries in the velocity and normal stress profiles were found to be 3% of the maximum mean velocity and 5% of the maximum normal stress respectively. Further confirmation of the accuracy of the measurements was made by comparing the integrated velocity profiles across the radius of the flow, at several locations, to determine the maximum continuity error. This was found to be less than 5% of the total mass flow and attributed to errors in the integration. Measurements were not taken in the annular passage around the downstream tube as the signal frequencies (and hence velocities) were very low and not readily distinguishable from the uncertainty in the shift frequency imposed by the rotating grating.

The mean axial velocity and normal stress $\overline{u^2}$ profiles for each measuring location are given in Figure 4.3.2; the more important aspects of the flow are now described.

(i) At $^x/D = 1.64$ and 1.79, upstream of the gap, the velocity distribution in the annular passage shows a bias in the maximum velocity towards the inner tube wall which is consistent with turbulent annular flows (see, for example, Brighton and Jones 1964). The velocity distribution, across the radius, inside the inner tube shows a negative region at the centre with a positive region forming a toroidal ring around the wall. The normal stress profile shows a small increase near the wall in the positive mean velocity region. The normal stresses are much lower in the annular passage.

(ii) At $^x/D = 1.95$, at the extreme downstream edge of the upstream tube, the annular flow is about to enter the gap which is a low pressure region relative to the inlet, and the profile shows even higher velocities near the inner wall. The mean flow within the upstream tube has maintained a profile similar to those of $^{X}/D$ = 1.64 and 1.79 however, the normal stress near the inside wall has increased slightly.

(iii) $^{X}/D$ = 2.04 is the first axial location totally within the gap and shows: an increase in the magnitude of the central negative velocity region, the high velocity annular flow moving towards the centre and larger positive velocities (at $^{r}/R$ = 0.64). The centre of the normal stress profile remains approximately constant, however, the wall peak at $^{X}/D$ = 1.95 has reduced in magnitude and a further peak has developed near the outer tube wall.

(iv) At $^{X}/D$ = 2.13, midway within the gap, the negative central region persists although reduced in magnitude, showing the significant influence the upstream recirculation has on the flow in the gap region. Similarly, the trend of the mean velocity profile near the outer wall implies that the downstream annulus recirculation extends into the gap although no negative velocities were actually measured due to the proximity of the wall. The peak of the $\overline{U}$ profile, entering the gap from the upstream annulus, has broadened and decreased in magnitude. This trend continues until, at $^{X}/D$ = 2.25, the maximum $\overline{U}$ is midway across the radius and the negative central region has disappeared due to the start of the acceleration of the velocities into the downstream tube. The normal stress increases on the centre line between $^{X}/D$ = 2.13 and 2.25 the profile showing a minimum at a radius corresponding to the maximum $\overline{U}$ velocity.

(v) The $\overline{U}$ profile at $^{X}/D$ = 2.53 positioned near the upstream end of the downstream tube, shows the rapid increase in the $\overline{U}$ velocity as it enters the downstream tube. The increase in $\overline{U}$, on the centre line, due to the abrupt area reduction, is about 100% whilst the maximum

$\bar{U}$ has increased by 30%. The $\bar{U}$ measurements do not show any separation from the corner of the tube. Again, the normal stress profile is a minimum at a radius corresponding to the maximum $\bar{U}$.

(vi) The trends of the profiles at $^{x}/D = 2.33$ are similar to those at $^{x}/D = 2.43$, namely, the rapid acceleration of the mean velocities and the further movement of the position of maximum $\bar{U}$ towards the centre line. The increased normal stress near the wall indicates the presence of a shear layer.

(vii) Evidence of the separation is shown in the profiles at $^{x}/D = 2.55$ where $\bar{U}$, near the wall, is negative and creates a high gradient at $0.92 > {^{r}/_{R}} > 0.61$. The separation region and associated shear layer cause a significant increase in normal stress near the wall.

(viii) The $\bar{U}$ profile at $^{x}/D = 2.63$ shows the negative region near the wall and the high gradients of both $\bar{U}$ and normal stress as well as the further migration of the maximum $\bar{U}$ towards the centre and the rapid increase in the centreline velocity.

(ix) At $^{x}/D = 3.02$ and 3.33 $\bar{U}$ becomes positive near the wall after reattachment and the previous rapid increase in centre line reduces. This is again evident in the normal stress profile which broadens as the shear layer weakens.

(x) At $^{x}/D = 3.79$, which shows a full profile for both $\bar{U}$ and normal stress the maximum $\bar{U}$ is positioned at the centre line. The maximum normal stress is reduced in magnitude and starts to move towards the centre line. The profiles at the last measuring station, $^{x}/D = 4.25$ show the continuing development of the profiles.

The above description of the measured values of mean axial velocity and normal stress indicates the complexities within even a conceptually simple combustion chamber arrangement. The potential difficulties, as regards the calculation procedure, stem from mainly around the gap region where the incoming jet from the annulus interacts with three separate recirculation regions. The correct calculation of the flow downstream from the gap, therefore, depends strongly on the ability of the calculation procedure to adequately resolve the physical aspects in this complex flow region.

4.4 THE CALCULATION DETAILS

The finite-difference grid and its relation to the model geometry is shown in Figure 4.4.1. The axisymmetric nature of the geometry and boundary conditions require consideration of only one half of the model geometry for the calculation domain. The importance of grid node location is discussed in detail later in this section but the extent of the grid was five gap widths upstream, and six downstream, of the gap.

The boundary conditions for the calculation, the implementation of which was discussed in section 3.2.4, were mainly taken from experimental measurements as follows:

(i) Symmetry about the centre line was assumed.

(ii) Zero velocities at all solid surfaces (including internal walls)

(iii) Zero gradient ($\partial\phi/\partial x = 0$) for variables at the outlet (the solution was not sensitive to this condition at six gap widths downstream of the gap).

(iv) The inlet boundary conditions for velocity, in the annulus, were assigned values interpolated from the measured values.

(v) The inlet turbulence kinetic energy was deduced from the measured axial normal stress, assuming local isotropy.

(vi) The energy dissipation rate, at the inlet, was calculated using a mixing length formulation based on the dimensions of the annulus (eqn. 3.12).

The equations for velocity, pressure, turbulence kinetic energy and energy dissipation rate were solved using the numerical scheme outlined in Chapter 3. The iterative cycle of the solution procedure was terminated by a convergence criterion based upon the ratio of the magnitude of the overall continuity error and the total mass flow rate. The solution was considered to be converged when this ratio dropped below 0.5%.

The influence of the number and location of grid nodes was determined by performing calculations with different grid arrangements. The extent of this investigation was limited by the cost and availability of computer time but encompassed a range from 352 (22x16) to 1480 (37x40) grid nodes. The location at which the dependance of the solution on grid distribution proved most sensitive was $^{x}/D = 2.55$; profiles of axial velocity, for this location, are shown in Figure 4.4.2. Preliminary investigations with a 22x16 grid showed important discrepancies when compared to the measured profile; for example, the measured separation region was not predicted (Figure 4.4.2) and both maximum and centre line velocities were under-predicted by 35%. The method used to increase the accuracy within this region was to plot the local axial pressure profiles at $^{r}/R = 0.95$, for a series of calculations, to optimise the resolution of pressure gradients. An example of such a pressure profile is given in Figure 4.6.2 and shows the large pressure gradients in this region. The predicted axial velocity profile at $^{x}/D = 2.55$ for an optimised 28x30 grid distribution (Figure 4.4.2) gave substantial improvement in both qualitative and quantitative agreement, reducing the discrepancy in maximum velocity to 24%. The benefit of this approach is the increase in accuracy by local grid refinement, with a limited number of grid nodes, without depending upon experimental profiles. Further grid refinement (37x40 nodes) reduced the discrepancy to 17%, however this was gained only at substantial extra cost i.e. a tenfold increase.

The number of iterations required for convergence, at each level of grid fineness, was found to increase exponentially i.e. grids of 22x16, 28x30 and 37x40 nodes required 300, 600 and 1500 iterations respectively. The stability of the calculation also became progressively lower at each successive level and the under-relaxation parameters, factors limiting the maximum change each variable is allowed per iteration (Gosman and Pun, 1973), had to be decreased. Consequently the 28x30 grid distribution was chosen as the best compromise between accuracy and economy and used on all subsequent two-dimensional calculations. Typically the calculation required about 600 iterations taking 750 s and 46000 words storage on a CDC6600 computer.

4.5 COMPARISON OF MEASURED AND CALCULATED RESULTS

A direct comparison between measured and calculated radial profiles of mean axial velocity at four axial locations (corresponding to measuring locations $^{X}/D$ = 1.64, 2.13, 2.55 and 3.33) is given in Figure 4.5.1 and comprises the following features:

(i) At $^{X}/D$ = 1.64 the annulus flow velocity profile is calculated to within 5% of the measured velocity profile. The mean velocity flow profile within the upstream tube is in qualitative agreement with the measurements, however, both the maximum and minimum axial velocities are over-predicted, implying a larger upstream to downstream flow ratio than was measured. Due to the abrupt area change between the gap and the upstream tube, errors occurring in the gap flow profiles would be expected to be exaggerated within the upstream tube.

(ii) At $^{X}/D$ = 2.13 midway within the gap, the over-prediction on the centreline is again evident, contributing to centre line errors both upstream (over-predicted velocity) and downstream (under predicted velocity). The extreme end of the downstream annular recirculation region is shown clearly, in the calculations, to extend well upstream near the outer wall which was only indicated in the measurements by extrapolating them near the wall. The slight radially outward shift in the outer part of the calculated velocity profile may be due to the application of empirical wall functions within a separation region and, in so doing, causes further error downstream. Simpson et al (1977) have stated their doubts as to the validity of a logarithmic law, upon which the wall functions are based (Section 3.2.4), when used in a separate region.

This particular profile may also be expected to be subject to numerical diffusion (section 3.3.2) due to the high magnitude velocities and their non-alignment with the grid axes, however this was not found to be the case. The ratio of convective to diffusive flux for cells in this region, the cell Peclet number, was of the order |100| even for the finest grid distribution (37x40) and therefore potentially prone to numerical diffusion. In order to evaluate the extent of the numerical diffusion each term in the axial momentum equation, i.e. convection, diffusion and pressure gradient, was evaluated, using central differences, across the radius and the relative magnitudes of each compared (a similar approach to that of McGuirk and Rodi 1978). It was found that in general, the convection and pressure terms were two orders of magnitude higher than the diffusion terms and therefore concluded that in this region numerical diffusion was not significant.

(iii) Comparison of the measured and calculated velocity profiles at $^{x}/D = 2.55$ show good qualitative agreement, namely the prediction of separation on the wall and the radial position of maximum velocity. The underprediction of the maximum velocity (17%) is due to incorrectly calculating the radial position of the shear layer (i.e. too near the wall) resulting in a flattened velocity profile. The size of the separation region and the shear layer is again subject to uncertainties in the wall function treatment used. This is especially true in the separation region as, in order to adequately resolve the flow profile, several grid points have to be placed in close proximity to the wall giving a $y^{+}<10$ which strictly invalidates the wall functions where a requirement is $y^{+}>11.5$.

(iv) The discrepancies between measured and calculated mean velocity profiles at $^x/D = 3.33$ are, at the most, 10% of the maximum velocity; the calculation again underpredicts the measurements. This increase in accuracy, compared to $^x/D = 2.55$ is the result of lower velocity gradients and the absence of recirculation. The discrepancies at this station undoubtedly accrue from upstream influences, especially errors in predicting the size of the separation region and the radial position of the shear layer.

An overall comparison, between measured and calculated streamlines is shown in Figure 4.5.2. Each of the recirculation regions are well defined and indicate the complexity of the flow in the gap region.

4.6 CALCULATED RADIAL VELOCITY, PRESSURE AND KINETIC ENERGY

The calculated results described in this section, namely radial mean velocity and pressure do not have corresponding measurements for comparison and hence lack an accurate estimation of error. It is therefore necessary to assume the axial mean velocity comparisons of section 4.5 give a sufficiently representative measure of the overall accuracy of the calculations and to validate any further results from the same calculations.

The calculated contours of radial mean velocity are given in Figure 4.6.1. The largest velocities are concentrated in the downstream half of the gap, where the flow experiences an abrupt directional change. The maximum radial velocity occurs at the inner edge of the downstream tube. The influence of the separation from the outer corner of the upstream tube is shown both by the location of the $\overline{V} = 0.0$ m/s contour, which indicates radial outward flow at the upstream gap face, and by the 'lobed' shape of the $\overline{V} = -0.5$ m/s contour biassed towards the downstream part of the gap and centre region. The $\overline{V} = 0.0$ m/s contour, upstream and downstream border the positive radial velocity regions of the upstream cavity recirculation and the radially outward flow around the downstream separation point, respectively.

The calculated contours of normalised[*] pressure within the flow field are shown in Figure 4.6.2. The very high gradients located at the inner edge of the downstream tube are responsible for the sensitivity of the solution to the local discretisation of the calculation domain referred to in section 4.4. At this position the pressure field experiences a sharp discontinuity which requires adequate resolution by careful application of the finite-difference grid. The pressure distribution in the annulus, where the pressure at the outer wall (p_c=0.0) is greater than near the inner wall (p_c=0.2), explains the behaviour of the mean axial velocity profile in the annulus measured at successive stations (discussed in section 4.3(ii) and shown in Figure (4.3.2) as it approaches the gap i.e. the decrease in the velocities near the outer wall and increase in velocities near the inner wall. The pressure field within the inside tubes shows a stagnation point and consequent pressure rise on the centre line ($^x/D$ = 2.14), where the flow converges after entering the gap, and relatively small pressure gradients upstream and downstream of the gap.

The calculated contours of turbulence kinetic energy are shown in Figure 4.6.3 and indicate the region within the flow where the kinetic energy is the highest. This occurs in all the recirculation zones and at the jet stagnation point on the centre line ($\overline{U}$ = 0.0 m/s). Qualitative agreement on regions of high turbulence kinetic energy with measured normal stress may be made with reference to Figure 4.3.2 where the profiles show high values in the downstream tube, at the centre line stagnation point and in the gap region.

---

[*] normalised pressure $p_c = \dfrac{p - p_{inlet}}{\rho\, \overline{U}^2_{inlet}}$

4.7 FURTHER CALCULATIONS

Further calculations were made to investigate the influence, on the flow, of modifications to the geometry. The modifications were restricted to varying the annular passage width and the gap width (y_{pass} and x_{gap} respectively in Fig. 4.7.1). independently whilst maintaining a constant mass flow. The parameters used to measure the changes to the general flow were as follows:

(i) The percentage R_{AV} of the total mass flow that travels upstream into the upstream cavity. This parameter, which in practice is usually estimated from flow visualisation, is of interest as combustion efficiency is strongly affected by the amount of upstream recirculation.

(ii) The average resultant velocity $\overline{T}_{AV}$ of the jet issuing from the gap. This is determined as follows:

$$\overline{T}_{AV} = \sqrt{(\overline{U}_{AV}^2 + \overline{V}_{AV}^2)}$$

$$\text{and } \overline{U}_{AV} = (\sum_{i=1}^{n} \overline{U}_{i,R} \;.\; \Delta x_i)/(\sum_{i=1}^{n} \Delta x_i)$$

$$\overline{V}_{AV} = (\sum_{i=1}^{n} \overline{V}_{i,R} \;.\; \Delta x_i)/(\sum_{i=1}^{n} \Delta x_i) \quad .$$

where n varies according to the number of grid nodes distributed across the gap ($\sum_{i=1}^{n} \Delta x_i = x_{gap}$) and the radial position of the average resultant velocity is at $r = R$ (Figure 4.7.1).

Parameter $\overline{T}_{AV}$ is, therefore, the area weighted jet mean velocity entering the inner combustion region (flame tube) through the gap and α_{AV} the average trajectory angle of the jet. These are, again, parameters estimated from empirical data and flow visualisation.

Table 4.7 gives the values of R_{AV}, $\overline{T}_{AV}$ and α_{AV} for the standard (which has been described in detail in previous sections) and modified geometries. The gap width x_{gap} was decreased in two equal stages to a final value of 50% of the standard width. The annular passage width was varied in equal, linear amounts of±25% of the standard width; this, due to the area variation being proportional to the square of the linear variation giving an effective variation of +38% and -29%.

TABLE 4.1 Influence of Geometrical Modification on Jet Behaviour

Geom. detail varied	Dimensional variation %	Effective flow area variation (%)	$\bar{T}_{AV}$ ($^m/s$)	α_{AV} (°)	R_{AV} (%)
Standard	0	0	1.06	52.6	10.3
Gap width	(-25	-25	1.33	59.0	10.2
	(-50	-50	1.86	63.8	9.5
Annulus width	(+25	+38	0.98	60.0	7.4
	(-25	-29	1.06	53.3	13.5

Inspection of Table 4.1 shows that there is no simple correlation between the average trajectory of the incoming jet and the upstream recirculation for this flow geometry. For example, increasing the incoming jet velocity and trajectory angle, by successive decreases in the gap width, produces smaller values of upstream recirculation. Further it is not clear why small variations in flow angle and velocity produced by decreasing the annulus flow area by 29% results in a relatively large increase in upstream recirculation. In order to explain the variation in values of the parameters in Table 4.1 it is necessary to use the calculated results and examine the detailed structure of the flow.

(i) Decreasing the gap width by 25% produces a negligible change in the upstream recirculation even though both $\bar{T}_{AV}$ and α_{AV} are substantially increased implying a greater potential tendency to flow upstream. However the increase in penetration, indicated by the proximity of the radial velocity contours (Figure 4.7.2) to the centre line, produces a blockage at the upstream edge of the gap hence effectively preventing the positive direction flow from emerging out of the upstream cavity. This blockage tends to balance the (potentially) greater upstream flow due to the impingement of the jet at the centre line, resulting in little change in the upstream recirculation.

(ii) A further decrease in the gap, to 50% of the standard width, results in a smaller upstream recirculation. The penetration is shown in Figure 4.7.2 and, although greater than the standard penetration, is again accompanied by a reduction in axial flow from the outer radial region of the upstream cavity (where the flow area is greatest) due to the blockage effect of the jet. This effect is also shown (Figure 4.7.3a) in the radial profiles of axial velocity at an axial location in line with the upstream gap edge ($^X/D$ = 1.95) where the sharp decrease in axial velocity in the outer radial region is evident.

(iii) Increasing the annulus width substantially reduces the annular velocity as shown (Figure 4.7.4) in the radial profiles of axial velocity at an axial location just downstream of the gap edge ($^X/D$ = 1.96). The effect of this reduction is to displace the separation region, at the upstream gap edge, radially inwards producing a blockage to the positive flow emerging from the upstream cavity (Figure 4.7.4a). Furthermore, the reduced penetration (Figure 4.7.2) also serves to decrease the flow diverted upstream as the jet impinges.

(iv) Decreasing the annulus width and maintaining a constant flow rate increases the velocities in the annulus (Figure 4.7.4a) and produces a small increase in penetration as shown by the radial velocity contours (Figure 4.7.2). More importantly the shear layer and the associated separation region, produced at the outer upstream edge of the gap, does not protrude into the outer radial region of the inside tube and, hence, does not present any blockage to the positive direction flow emerging from the upstream cavity. This is clearly indicated in Figure 4.7.4. where the negative axial velocities are situated at a greater radius than for the standard case. These two factors contribute towards an increase in the upstream recirculation.

The foregoing analysis indicates that the inability to correlate the geometrical modifications with the averaged parameters for the incoming jet (i.e. α_{AV} and $\bar{T}_{AV}$) is due to the failure of averaged parameters to adequately describe the flow. By averaging across the gap width essential detailed information, such as the position of local separation regions which can exert a controlling influence upon the flow, is lost in the averaging process.

4.8 SUMMARY

This chapter has examined, in detail, the measurement and calculation of the isothermal flow in an idealised, two-dimensional, axisymmetric combustion chamber geometry. This geometry, the first in a series of increasing complexity, was chosen so as to highlight and possibly exaggerate areas requiring greater attention in both calculation and measurement, for future work, on more representative, three-dimensional geometries. One such area has been to ensure a fine grid distribution in regions with high gradients in order to adequately resolve the pressure field. Comparison between the measured and calculated variables have shown a variability dependent upon location and local gradients. For mean and axial velocity the calculations show underpredictions of 5-17%. Other flow variables calculated, i.e. radial velocity, pressure and kinetic energy that were not measured give further insight into the details of the flow.

Further calculations were performed varying two geometrical features, namely, the annulus passage width and the gap width (hole diameter in practical combustion chambers). The upstream recirculation ratio was chosen as a representative parameter for assessing the effect, on the flow, of geometrical changes. It was found that the largest variations in upstream recirculation ratio occurred when the annulus width was varied rather than the gap width. A simple explanation for this was not obtainable by considering an averaged jet velocity or trajectory but required a more detailed analysis using the axial and radial velocity distributions.

The work in this chapter has shown the plausibility of using a finite-difference technique for calculating the flow in a complex two-dimensional geometry. The level of quantitative agreement between calculation and measurement has been high enough to warrant extension to more realistic three-dimensional combustion chamber goemetries.

C H A P T E R 5

A THREE-DIMENSIONAL MODEL WITHOUT AN ANNULUS

5.1 INTRODUCTION

5.1.1 Limitation of Two-dimensional Study

The isothermal aerodynamics of gas turbine combustion chambers is subject to details in flow that a two-dimensional model,as described in Chapter 4, cannot fully simulate. Two important details lacking in the two-dimensional investigation were the effect of the fuel and air momentum on the primary zone flow field and the interaction of the primary jets with the mainstream flow near the chamber wall; these two aspects are now briefly discussed.

The practical methods of introducing the fuel and air into combustion chambers have been outlined in Chapter 1. The two-dimensional model, having a completely closed upstream section, was unrepresentative of the flow in the primary zone, as at any cross-section, the total mass flow is zero.

The method of providing the main primary air flow in the two-dimensional model was, again, unrepresentative of normal combustion chamber design where air injection is made through discrete, round holes, in the chamber wall. This has an important effect on the primary air flow where the combustion products flow out of the primary zone i.e. between the discrete primary jets. In a two-dimensional model this effect is not simulated, as a slot jet, effectively blocks the total circumferential area near the chamber wall.

5.1.2 Extension to Three-dimensional Flows

The limitations of a two-dimensional model may be removed by providing a through flow in the primary zone and discrete primary jets. A detailed description of the geometries, used in the work of this chapter, are given in section 5.2; however, it is worthwhile here to outline the intended achievements and expected difficulties of this work in relation to previous work and to practical combustion chambers.

The provision of discrete primary holes produces a three-dimensional flow which necessitates a great deal more effort in measurement and in computation. In contrast to two-dimensional work, measurements have to be taken on more than one plane, for example, in the plane of the jets and also between the jets. The calculation of a three-dimensional flow is more time consuming and expensive than a two-dimensional calculation and the number of finite-difference grid nodes is limited by the computer storage available. However, future use of numerical models by industry, requires that they are tested extensively against authentic, three-dimensional flows. For example, the two-dimensional work required special attention, at points where the jet entered the "flame tube", by placing a fine grid distribution where velocity and pressure gradients were largest. This operation is not so readily applicable in a three-dimensional calculation due to the limit on the total number of grid nodes.

The procedure of work used previously, i.e. flow visualisation, measurements, calculations, comparison of calculations with measurement and further calculations will be used for the three-dimensional work. It is further intended to examine the sensitivity of the numerical model to changes in geometry and boundary conditions from a standard case. Previously, section 4.7, the modifications to the standard two-dimensional geometry were made using calculations only; in this chapter the results of modifications will be substantiated by measurement to assure an accurate assessment. This is important from a practical standpoint due to the lack of tools available to the designer for quantifying the effects of production or development modifications.

5.2 DETAILS OF THE MODEL

5.2.1 The Geometry

The model geometry, shown in Figure 5.2.1, was designed to accommodate some of the complexities of a gas turbine combustion chamber, particularly the simulation of discrete primary jets. One important simplification, however, is the absence of an annulus which is used to supply the primary and dilution jets with cool air, in actual combustion chambers.

The model geometry comprised the following features:

(i) The main tube, which acts as a flame tube, carried the flow introduced through the baseplate and the primary jet tubes. The main tube was made in cast acrylic of high optical quality.

(ii) The baseplate was attached to the main tube using a flanged fixing and was machined to accept a small diameter transparent tube. The purpose of the small, centrally located, tube was to introduce a through flow into the primary zone simulating the effect of injected air and fuel.

(iii) The positions of the primary ports on practical combustion chambers determine the size and strength of the primary zone recirculation. Typically these are placed one flame tube diameter downstream of the baseplate. Consequently, the primary jet tubes were placed one main tube diameter downstream of the baseplate.

(iv) The water was supplied from the constant head tank described in Chapter 2 using flexible tubes and a flow separating plate. A valve was fitted to each tube to allow individual control of the flows to the baseplate and primary tubes.

The substitution of an annulus by tubes simplifies the determination of the inlet conditions as the flow in the tube, and the entry angle, may be accurately determined. This allows a simple application of boundary conditions to the calculation procedure whilst still ensuring a three-dimensional flow inside the main tube. Accurately determined boundary conditions are necessary because of the intention to both measure and calculate the main tube flow with various inlet conditions to test the sensitivity of the numerical model.

Further development of the geometry was found to be necessary after observations made using flow visualisation. Details of the flows are given in section 5.2.2 but, briefly, observations showed that the degree of recirculation in the primary zone was sensitive to the magnitude of the baseplate jet flow, and for some values, atypical flow patterns were produced. To reduce the sensitivity of the baseplate jet flow, a baffle (Figure 5.2.1) was positioned just downstream of the baseplate jet entrance so as to produce a radial jet.

5.2.2 Observed Flow Patterns using Flow Visualisation

The hydrogen-bubble technique, used in a similar manner as in the two-dimensional work in Chapter 4, allowed the flow patterns to be observed when the baseplate flow was altered. The results of altering the baseplate tube flow, when a baffle is not present, is discussed as follows:

(i) The general flow pattern is shown schematically in Figure 5.2.2(a) for planes in line ($\theta=0^{o}$) and between primary jets ($\theta=45^{o}$) where the mass flow rate in the baseplate tube is equal to the flow rate in one of the primary tubes (i.e. a velocity ratio of 1:1).

(ii) Observations showed the domination of the flow by the baseplate jet which travels downstream on the centre line.

(iii) The primary jets are forced downstream by the baseplate jet and none of the primary jet fluid reaches the primary zone.

(iv) Recirculation in the primary zone is caused solely by the abrupt enlargement from the baseplate tube to main tube.

By reducing the mass flow from the baseplate jet to one third of its former value, whilst maintaining the primary jet flow rates constant (i.e. a velocity ratio of 1:3.0) the flow patterns depicted in Figure 5.2.2(b) were observed. The main features are as follows:

(i) The flows through the primary jet tubes form four discrete jets each of which diverge as they enter the main tube. At approximately mid-radius the jets merge into each other forming a stationary region at the centre line where the flow divides and travels to the lower pressure regions upstream and downstream.

(ii) The simple jet, entering through the baseplate, travels downstream along the centre line of the primary zone until it impinges on the merged primary flow travelling upstream. The location between the baseplate and the primary jet centre line at which impingement takes place depends upon the relative strengths of the baseplate and primary jets.

(iii) A low baseplate jet velocity produces a large toroidal recirculation region in the primary zone, typical of the flow pattern observed in actual combustion chambers. The recirculation has an upstream velocity direction on the centre line and a downstream velocity direction in the outer radial regions near the wall of the main tube.

(iv) Significant three-dimensionality in the flow pattern is mainly restricted to the regions around the primary jets. On the upstream side, flow from the downstream directed part of the recirculation, in the plane of the primary jets ($\theta = 0^{0}$) moves circumferentially in order to flow between the jets ($\theta = 45^{0}$) and on downstream. On the downstream side of the jets the flow recombines, again by moving circumferentially.

The general flow patterns when a baffle is placed just downstream of the baseplate entry are shown in Figure 5.2.2(c). The qualitative differences between these and the simple jet entry flow patterns Figure 5.2.2(b) are restricted to the region nearest the baseplate. Here, the baseplate inlet flow travels radially out from behind the baffle and merges with the toroidal recirculation generated by the primary jets as before. As part of a combustion chamber model the baseplate entry flow from behind a baffle has two advantages over a simple axial jet; these are:

(i) The length of the toroidal recirculation in the primary zone is independent of the relative jet strengths and is determined solely by the distance between the baffle and the primary jet centre line. This allows a study of the effects on the flow over a range of jet velocities, without making unrealistic changes to the basic primary zone flow pattern.

(ii) The flow patterns caused by the presence of the baffle approximate to those found around vaporiser inlets as described in Chapter 1. This adds authenticity to the simulation which might only be achieved, otherwise, by resorting to a small swirler to create the centreline depression. Due to the difficulty of fabricating such a device, to sufficient accuracy, the baffle was considered to be the optimum choice.

5.3 THE MEASUREMENTS

5.3.1 The Range of Measurements

The range of mass flow rates of baseplate and primary jets investigated is summarised in Table 5.1. The Reynolds number for each case was based upon the bulk axial velocity in the main tube downstream of the primary jets.

Case 1 where the baseplate jet forced the primary jets downstream producing flow patterns of little relevance to combustion chambers (Figure 5.2.2(a)) was not subsequently calculated. The measurements that

Table 5.1 Flow Rates for Measured Cases

Case No.	Baffle	Mass Flow Rate (kg/s)		Reynolds No.
		Base Plate	Primary	
1	No	0.191	0.774	4.8×10^4
2	No	0.056	0.774	4.2×10^4
3	Yes	0.151	0.774	4.7×10^4
4	Yes	0.107	0.774	4.5×10^4
5	Yes	0.151	0.098	1.3×10^4

were taken indicated that the flow downstream of the primary jet plane was asymmetric and swirling and this is discussed briefly in the next section.

Measurements of mean axial velocity $\overline{U}$ and normal stress $\overline{u^2}$ were made on two circumferential planes for cases 2 to 5. The planes and measuring locations are shown in Figure 5.3.1. The plane midway between the primary jet tubes ($\theta = 45^o$) comprised twelve axial measuring locations each with nine radial measuring locations, distributed upstream (to the baseplate), and downstream (1.6 main tube diameters) of the primary jet tube centreline. The plane passing through the centreline of one primary jet tube ($\theta = 0^o$) comprised eight axial locations each with nine radial measuring locations. The reduction in the number of axial locations ($\theta = 0^o$) was caused by interference of the passage of the laser light beams just upstream and downstream of the primary jet tubes. The flow details measured for each geometry are discussed in the next section.

5.3.2 Measurements with Baseplate Jet Only (Cases 1 and 2)

As mentioned in the previous section, extensive measurements for Case 1 were not made due to the unsuitability of the flow patterns for representing a typical combustion chamber flow. One aspect, however, discovered with this flow was the asymmetric behaviour measured at $^x/D = 4.6$. This is shown in Figure 5.3.2(a) for axial velocity profiles for the baseplate jet alone, the primary jets alone and all jets running.

The profiles show symmetric behaviour to within 5% of the centreline velocity, for the base plate jet and primary jets alone but marked asymmetry when all jets are running. The evidence suggests the inability of the primary jets to bend downstream under the force of the baseplate jet and to still maintain symmetric behaviour. This anomaly could not be predicted using a numerical model, such as described in Chapter 3, due to the specification of symmetric boundary conditions.

The radial profiles for Case 2, where the baseplate jet is reduced to allow the primary jets to impinge and travel upstream, for mean axial velocity and normal stress are shown in Figures 5.3.2(b) and 5.3.2(c). The following features are exhibited:

(i) The mean velocity profile at $^x/D = 0.1$ indicates the weakness of the base jet which meets the upstream merged flow from the primary jets. The location of impingement is at approximately $^x/D = 0.12$. Surrounding the baseplate jet is a slow moving upstream flow, which is, in turn, surrounded by a downstream velocity indicating the large toroidal recirculation. The maximum normal stress occurs on the centre line where the highest velocity gradients are, due to the impingement of the jets just downstream.

(ii) At $^x/D = 0.2$ the strong upstream flow from the primary jets is evident from the maximum negative velocity occurring on the centre line. The maximum normal stress no longer lies on the centre line but is situated nearer to the maximum mean velocity gradient which occurs near mid-radius.

(iii) The mean velocity profiles at $\theta = 45^o$ and at $^x/D = 0.4$, 0.6 and 0.8 exhibit similar trends. The centreline upstream (negative) velocity increases as the primary jets are approached. The downstream (positive) velocity near the wall of the model also increases due to the acceleration of the flow around the blockages formed by the incoming primary jets. The normal stress maxima occur at approximately $^r/R = 0.6$ at the location of maximum mean velocity gradient.

(iv) At $^x/D = 1.0$, the axial location of the primary jets, the velocity at the centreline is small and negative, extending out to mid-radius, where the positive velocity of the flow between the primary jets is shown. The profile also shows that the primary jets merge with each other at about mid-radius as they travel towards the centreline. The maximum normal stress occurs at approximately this radial position.

(v) Further downstream, at $^x/D = 1.2$, the centreline mean velocity accelerates rapidly caused by the merged primary jet flow. The velocity near the model wall decreases as the flow area downstream of the jets increases. The maximum normal stress moves radially inward and increases in magnitude, this is due to the higher maximum velocity gradient.

(vi) Evidence of the recirculation region on the downstream face of the primary jet is shown at $^x/D = 1.4$ and $\theta = 0^o$, where the mean velocity is approximately zero. The centreline velocity reduces in magnitude as the flow develops and the normal stress maximum is indicated on the centreline.

(vii) Further downstream the trends remain constant, i.e. a slow decrease in the centreline velocity and normal stress whilst the velocity in the outer regions, at $\theta = 0^o$ and 45^o, increase as the flow develops further. At the final measuring station ($^x/D = 2.6$) the flow becomes axisymmetric.

Contours of mean axial velocity for $\theta = 45^o$ are shown in Figure 5.3.3 and highlight the following features:

(i) The baseplate jet experiences a rapid reduction in velocity due to impingement on the upstream travelling primary jet flow.

(ii) The area between the jets is the only means by which flow from the primary zone can travel downstream and this is indicated by the shape of the $\overline{U}$ = 0.25 m/s contour.

(iii) The velocity maxima, both negative and positive, lie adjacent to the cross-plane of the jets and their relative magnitudes indicate that a smaller proportion of the primary jet flow travels upstream.

Investigations using this particular geometry were not taken further due to the unrealistic dependance of the primary zone flow pattern on the relative mass flows of baseplate jet and primary jets. Further investigations were undertaken with a baffle placed centrally in front of the baseplate jet.

5.3.3 The Measurements Incorporating a Baseplate Jet and Baffle (case 3)

The radial profiles for both mean axial velocity and normal stress are shown in Figures 5.3.4a and 5.3.4b. Just upstream of the primary jets and on, further downstream, the general flow patterns closely resemble those with a baseplate jet only. Contrasting details in the flow i.e. those occurring near to the baseplate, are now examined in detail:

(i) At $^{x}/D = 0.1$ the mean axial velocity profile at $\theta = 45^{0}$ shows a small negative value on the centreline just downstream of the baffle (located at $^{x}/D = 0.08$). The face of the baffle produces an area near the centreline where the axial velocity is small. At a radius corresponding to the edge of the baffle the axial velocity is directed towards the baseplate before increasing in magnitude in a downstream direction in the outer radii near the main tube wall. The shape of the normal stress profile is different from the non-baffle case in that its maximum occurs at a radius near the wall. This is due to the abrupt turning of the flow from a radial to an axial direction between the wall and the edge of the baffle.

(ii) At $^x/D = 0.2$ the profile of mean axial velocity is similar to the non-baffle case although the negative region is radially larger. The normal stress profile also closely resembles that of the non-baffle case at this location.

An overall evaluation of the contrasts in flow pattern may be obtained by comparing contours of mean velocity for both cases (Figures 5.3.3 and 5.3.5). The downstream quantitative differences are caused mainly by the extra mass flowing in the main tube giving for example, a much larger $\bar{U} = 1.0$ m/s contour in the case with the baffle. Detailed variations in the primary zone flow are clearly shown in the case, the short length of baseplate jet produces an impingement region that does not extend far ($^r/R \simeq 0.2$) from the centre line. This allows the upstream travelling primary jet flow to surround the baseplate jet giving a maximum radial distribution of negative velocities of $^r/R \simeq 0.6$.

In contrast, the case with the baffle, produces a wider negative velocity region ($^r/R \simeq 0.8$), its peak occurring at the same axial location as the face of the baffle. Nearer the primary jet cross-plane the zero velocity contour is also at a greater radial distance, $^r/R \simeq 0.6$, as opposed to $^r/R \simeq 0.4$ for the non-baffle case, indicating that the area between the primary jets is less.

5.3.4 Further Measurements Incorporating a Baseplate Jet and Baffle (cases 4 and 5)

Measurements of mean axial velocity and normal stress were made for a further two cases where the relative mass flows of the baseplate jet and primary jets were varied from the standard case. Although, due to the presence of the baffle no variation in primary zone recirculation length was expected, a quantitative understanding of the sensitivity of the flow to separate variations in baseplate and primary jet flow was needed. This would provide a reliable comparison for corresponding calculations which are discussed in section 5.5.

The baseplate jet mass flow was reduced by approximately 30% (case 4) and contours of mean axial velocity for $\theta = 45^{\circ}$ are shown in Figure 5.3.6. In comparison with the standard case (Figure 5.3.5) the following points are highlighted:

(i) few changes to the overall flow pattern occur in quantitative terms even though the reduction in baseplate flow is significant. This indicates the domination of the primary jet flow in this particular model geometry.

(ii) Details of the flow such as the zero velocity peak near the baffle, the positioning of the velocity maxima about the cross-plane of the primary jets and the axial locations of the contours on the centre line all remain unchanged. The only variation is the slight reduction in the radial extent of the higher velocity contours.

In order to produce a significant effect a reduction of 90% (case 5) of the primary jet mass flow was made. Mean axial velocity contours for $\theta = 45^{\circ}$ are shown in Figure 5.3.7 and may be compared to those of the standard case (Figure 5.3.5).

(i) As expected the length of the primary zone recirculation does not alter, however qualitative changes to the flow are prevalent.

(ii) Due to the weakness of the primary jets the radial extent of the zero velocity contour is successively reduced as the location of primary jets are approached. This is in contrast to the standard case where the zero contour remains at approximately the same radius throughout the primary zone.

(iii) Near the baffle the zero contour is at its maximum distance from the centre line as for the other cases. However, the radial extent of the contour shapes for negative velocities are greater towards the baffle, whereas in all other cases, the bias was towards the primary jets. As a result, highest measured negative velocity occurred at ${}^{x}/D = 0.4$ instead of ${}^{x}/D \simeq 0.8$ as in the other cases.

(iv) The higher positive velocity contours just upstream of the primary jet cross-plane indicate that, again, due to the weakness of the primary jets the area between the jets through which primary zone flow can travel downstream, is much greater than in the other cases.

This last case is particularly useful for evaluating the numerical model as the qualitative effects, between it and the standard case, have come from a simple change to the inlet (boundary) conditions.

5.4 DETAILS OF THE CALCULATIONS

5.4.1 The Grid

The discretisation of the model geometry, to form the finite difference grid, is shown in Figure 5.4.1. The symmetry of the experimental model, and its boundary conditions, allows the calculation domain to be restricted to only a 90^{o} sector in the circumferential direction. The grid extends to an ${}^{x}/D = 4.0$ with the highest concentration of grid nodes located around the primary jet inlet; this aspect is discussed more fully in section 5.4.3. The baffle, when incorporated, lies within the calculation domain and is treated as an internal vertical wall in a similar manner to the internal walls used in the two-dimensional calculations (section 4.4).

5.4.2 The Boundary Conditions

The boundary conditions were taken mainly from experimental measurements and are of the same form as those given for the two-dimensional calculations except in the following instances:

(i) Mean velocity and normal stress profiles were measured in the base plate and primary tubes one tube diameter upstream of the actual entry points to the main tube. For the cases incorporating a baffle, the mean velocity profile was integrated, the mass flow determined and applied at the inner edge of the baffle as a mean inlet radial velocity.

(ii) The periodic nature of the flow over 90^0 sectors allowed the cyclic boundary conditions, described in section 3.2.4, to be used for all variables at the edges of the periodic domain.

The influence of the boundary conditions on the flows was found to be minimal. For example, a 30% reduction of the mass flow from the base plate entry point (with baffle) was found to have only a small quantitative and no qualitative effect on the flow field for both calculations and measurements. A 10% variation in the kinetic energy boundary conditions were found to have no effect on the calculated kinetic energy distribution due to the very high generation of kinetic energy, especially in the primary jet region. This aspect is discussed in the next section.

5.4.3 The Application of the Numerical Model

The same basic procedure adopted for the calculations of the two-dimensional case was again used for the three-dimensional calculations. This entailed the solution of equations for three mean velocities, pressure, turbulence kinetic energy and energy dissipation rate using the technique described in Chapter 3. A similar convergence criterion to that used previously, was used again, whereby the iterative process was terminated when the overall continuity error dropped below 0.5% of the total mass flow.

It was found in the two-dimensional flow that the region just downstream of the jet entry point had to be resolved using a high proportion of the total number of grid nodes to produce reasonable qualitative agreement of profiles further downstream. In contrast, a study of this aspect in the three-dimensional flows showed that even a coarse grid produced reasonable qualitative agreement further downstream; this is discussed in section 5.5, where comparisons between measurement and calculation are made and further in the discussion section (section 5.6).

The range of grid distributions used encompassed 1088 (8 x 8 x 17) to 5130 (19 x 10 x 27) grid nodes and required between 200 and 400 iterations for satisfactory convergence. Grid refinement is especially difficult in three-dimensions and has been discussed by Jones and McGuirk (1979a) in reference to a three-dimensional calculation of a round jet issuing into a confined cross-flow. They state that the present limitations on computer storage capacity denies the use of fine enough grid distributions to ascertain full confidence in a solution being independent. However, by comparing measurements to calculated results for three-dimensional complex flows the degree of acceptability of even a coarse grid may be demonstrated.

Other numerical influences, investigated for the two-dimensional study, were also investigated for the three-dimensional cases. Cell Peclet numbers, $\frac{\bar{U}\Delta x}{\nu_t}$, range from below $|2|$ to $|10|$ which are lower than those found for the two-dimensional case. This indicates that the number of regions where upstream differencing and numerical diffusion are prevalent is less than for the two-dimensional case. The generally lower cell Peclet numbers are caused primarily by the higher turbulent viscosities, ν_t, as both $\bar{u}$ and Δx are approximately the same as those in the two-dimensional case. The highest turbulent viscosities are located at $^x/D = 1.0$ where the primary jets meet at the centre line and are a result of the high generation of kinetic energy (see eqn. 3.13). With relevance to eqn. 3.10 the generation term for the modelled kinetic energy equation contains terms involving $\frac{\partial \bar{U}_i}{\partial x_j}$ which are very large at $^x/D = 1.0$. Even with this high turbulent diffusion, however, the primary zone was found to be dominated by pressure. This was determined, as before, by examining the relative magnitudes of the separate terms in the calculated axial momentum equation where the $\frac{\partial p}{\partial x}$ term dominates by at least two orders of magnitude.

Further discussion on the performance of the numerical model and its relevance to practical combustion chamber design is given in section 5.6 after the comparisons between measurement and calculation for cases 2 to 5 in the next section.

5.5 COMPARISON OF MEASUREMENTS AND CALCULATION

5.5.1 Results for Case with Baseplate Jet (case 2)

An overall evaluation of the degree of correspondence, between the measured and calculated axial mean velocities, may be gained by comparing the combined contours (Figure 5.5.1) for the plane between primary jets ($\theta = 45^o$). The following features are shown:

(i) The greatest degree of disagreement between measurements and calculation is concentrated near to the baseplate and stems mainly from the calculated position of jet impingement. In the measurements the axial position of impingement between the baseplate jet and the upstream travelling primary jets is at $^X/D = 0.12$. The calculated position, however, is at $^X/D = 0.34$.

(ii) The over-prediction of the length of the baseplate jet foreshortens the calculated negative velocity zone setting up a recirculation zone in the corner which does not exist in the measurements. As a result the higher velocity flow near the wall, typified by the $\overline{U} = 0.25$ m/s contour , is not calculated and the flow does not reach this velocity until $^X/D = 0.5$ as compared to $^X/D = 0.08$ in the measurements.

(iii) Nearer the cross plane of the primary jets the agreement between calculation and experiment substantially improves. The region of high axial velocity gradients at $^X/D = 1.0$ is well predicted across the whole radius.

(iv) Further downstream, as the flow develops, the calculation tends to over-predict the lengths of the high velocity regions, especially near the centre line.

The radial profiles of calculated and measured velocities are shown in Figure 5.5.2 which also introduces some measured and calculated velocities for the plane through the jets. Poor qualitative agreement is shown in, for example, the profile at $^x/D = 0.2$ where the calculations show recirculation in the outer region and a positive velocity on the centre line, both of which do not exist in the measurements.

Other profiles exhibit good quantitative agreement as the centre plane of the primary jets is approached. At the jet centre plane, the profile for $\theta = 45^o$ shows the flow between the jets near the wall in both calculations and measurements and is accurately predicted. For the $\theta = 0^o$ plane, although not substantiated by measurement, the calculated profile shows very little axial velocity over the entire radius which is evidence of the perpendicularity of the primary jet. The profile at $^x/D = 1.2$ for the $\theta = 0^o$ plane shows a recirculation region near the wall behind the jet. Although, again, unsubstantiated by measurement the profile just downstream at $^x/D = 1.4$ shows measurements near the wall of $\overline{U} \simeq 0.0$ which provides some evidence of reattachment of the recirculation zone behind the jet.

5.5.2 Results for Case with Baseplate Jet and Baffle (case 3)

As for the previous case, an overall evaluation of the degree of correspondence between measured and calculated axial mean velocities is shown by comparing the combined contours (Figure 5.5.3) for the plane between primary jets ($\theta = 45^o$). The following features are shown:

(i) In the absence of the baseplate jet on the centre line the profiles of velocity are calculated more accurately in the primary zone as regards centre line positioning.

(ii) The agreement across radial planes shows good qualitative trends in the positioning of the maximum negative velocity and shapes of the individual contours. However the radial extent of the $\overline{U} = 0.0$ m/s contour, adjacent to the baffle is calculated to be less than the measured value, as are the higher negative value contours, $\overline{U}$ = -0.5 m/s and $\overline{U}$ = -0.75 m/s.

(iii) Downstream of the primary jet cross plane the positive contours again, are calculated to occur at smaller radii than measured; although, for example, the centre line extent of the $\overline{U}$ = 1.0 m/s contour is well predicted.

Further qualitative analysis may be made by comparing radial profiles of calculated and measured axial velocity for both planes (θ = 0^o and 45^o), these are shown in Figure 5.5.4 and feature:

(i) The maximum disagreement occurs on the centre line just downstream of the primary jets i.e. $^X/D$ = 1.2. In this region the flow undergoes a high increase in velocity which is not matched quantitatively by the calculations.

(ii) Agreement between calculation and measurement improves both upstream and downstream of the primary jet centre plane which is subject to very high axial velocity gradients.

(iii) The behaviour of the flow on the θ = 0^o plane near the entry point of the primary jets shows very similar behaviour to that in the previous case (case 2). In this region, the axial velocity is reduced to a small positive value across almost the whole radius at $^X/D$ = 1.0 and sets up a small recirculation region behind the primary jet. This is shown by the negative velocity calculated near the wall at $^X/D$ = 1.2.

An example of calculated mean velocity contours for θ = 0^o plane is given in Figure 5.5.5. Details in this plane, although only substantiated quantitatively by measurement upstream and downstream of the primary jets, show some parallels with the two-dimensional axisymmetric chamber described in Chapter 4. For example:

(i) The small recirculation region located just downstream of the primary jet, Figure 5.5.5, is qualitatively similar to the one shown in Figure 4.5.2 (streamline contours).

(ii) The pronounced peak in the $\overline{U} = 0.0$ m/s contour just upstream of the primary jet is also a characteristic of the two-dimensional case.

Examples of other variables amplify the knowledge of the flow found from the measurements and are briefly discussed in the following sections.

5.5.3 Radial Velocity and Kinetic Energy Results for Case 3

The main contours of calculated mean radial velocity for Case 3 are shown, for both planes, in Figure 5.5.6 and exhibit the following features:

(i) Both planes show axisymmetric behaviour for $^{x}/D < 0.4$. In this region the high positive (i.e. radially outward) velocities are due to the inlet velocity from behind the baffle, issuing as a radial jet, and from the impingement of the merged primary jets against the baffle face. Between $^{x}/D = 0.2$ and 0.4 the flow moves radially inwards as indicated by the region of negative radial velocity attached to the wall in both planes.

(ii) Downstream, where the primary jets meet ($^{x}/D = 0.5$), the radial velocity contours are asymmetric. The $\theta = 45^{o}$ plane shows the radial extent of the jet impingement ($^{r}/R \simeq 0.5$) by the position and shape of the $\overline{V} = 0.0$ m/s contour. The flow that passes from the primary zone between the jets, in this plane, is seen to rise rapidly just downstream of the primary jets ($0.6 > {^{x}/D} > 0.8$). Downstream of the primary jets a further rise occurs, especially at mid-radius ($^{x}/D \simeq 1.2$). Both these effects are caused by the merged primary jet flows moving radially outward after impact.

(iii) In the $\theta = 0^o$ plane the jet contours of radial velocity are clearly shown. These are distorted from the contours associated with a jet into stagnant surroundings (Abramovitch,1963) by both being flattened and biassed downstream. Further downstream in this plane the radial velocities become positive at $^x/D = 1.7$ as the flow recombines. Small negative radial velocities at $^x/D > 2.0$ indicate flow development.

The main contours of calculated kinetic energy for Case 3 are shown, for both planes, in Figure 5.5.7 and exhibit the following features:

(i) Again, upstream and downstream of the primary jets the contours are approximately axisymmetric. However, at $1.2 > {}^x/D > 1.5$ the $k = 0.25\ {}^{m^2}/{}_{s^2}$ contour at $\theta = 45^o$ is at a greater radius indicative of the presence of the flow between the jets and the higher mixing in this region.

(ii) The classic jet profile (Rodi,1972) is shown in the $\theta = 0^o$ plane where the shear layers on either side of the jet core produce higher kinetic energy. The jet contours, as shown by the radial velocity contours, are distorted from those of a jet issuing into stagnant surroundings, especially at $^r/R < 0.5$. At $^r/R = 0.4$ the jet profile of the kinetic energy disappears as the jets merge producing a region of high kinetic energy on the centre line.

This and the previous section has concentrated on the standard three-dimensional flow case (case 3) incorporating a baffle and has shown the degree of agreement between measurements and calculation for mean axial velocity and further calculated contours of radial mean velocity and kinetic energy. The next section briefly describes the ability of the numerical model to predict the flow within boundary conditions varied from the standard case i.e. the prediction of cases 4 and 5.

5.5.4 Results for Cases with Baseplate Jet and Baffle (cases 4 and 5)

Comparisons between measurement and calculation for the other cases (cases 4 and 5) are shown in Figures 5.5.8 and 5.5.9. These are examined to ascertain whether the calculations have accurately predicted the correct changes to the flow field, as were measured. Considering case 4 (Figure 5.5.8), where the baseplate mass flow rate was reduced by 30%; the following points are shown:

(i) In the measurements, few changes to the overall flow pattern occurred and this trend is repeated in the calculation.

(ii) The slight reduction in the radial extent of the higher value velocity contours found in the measurements is also matched by the calculation. Although detailed contour shapes still differ, the manner in which they differ, is similar to the detailed differences explained in section 5.5.2 for case 3.

Considering case 5 (Figure 5.5.9), where a more significant variation was made to the flow by reducing the primary jet mass flow by 90%, the calculated mean velocities showed the following trends:

(i) The radial extent of the zero and negative velocity contours in the primary zone show a marked decrease as the cross plane of the primary jets is approached. This is in direct agreement with the measurements.

(ii) In the same manner, the location of the calculated negative velocity maximum is biassed towards the baffle as occurs in the measured case.

(iii) The higher positive velocity regions in the primary zone i.e. $\overline{U} = 0.2$ and 0.3 m/s are accurately calculated to be at $^{r}/R \simeq 0.84$ although they tend to be larger in length than those measured.

In order to quantify the overall changes to the flow by varying the inlet mass flow rates Table 5.2 shows a comparison between measured and calculated locations of centre-line axial velocity maxima, minima and zero velocity.

TABLE 5.2 Location of Measured and Calculated Velocities

Case No.	Position ($^x/D$) of Mean Axial Velocity						Inlet Mass Flow Ratio
	zero		maximum		minimum		
	meas.	calc.	meas.	calc.	meas.	calc.	
3	1.03	1.00	1.20	1.28	0.80	0.75	0.195
4	1.03	1.00	1.20	1.28	0.80	0.75	0.138
5	1.06	1.01	1.28	1.38	0.40	0.38	1.54

These values show that the measured variations in location are represented in the calculations and that to effect any significant variation requires a large modification to the inlet mass flow rates.

5.5.5 Further Calculations

The baseplate to primary mass flow ratios of Cases 3, 4 and 5 encompass a wide range i.e. 0.138, 0.195 and 1.54 respectively. These were chosen so as to test the sensitivity of the calculation scheme for changes in boundary conditions. However for a consistent parametric study, further calculations are required to show the trends in the flow for values of mass flow ratio between 0.195 and 1.54. The characteristic parameter investigated in the two-dimensional case was the recirculation ratio R_{AV}, this can be defined, in the context of the three-dimensional case,as the percentage of the primary jet and baseplate mass flow that travels upstream into the primary zone $\left(\frac{\dot{m}_r}{\dot{m}_b + \dot{m}_p}\right)$. This parameter is investigated for the three-dimensional cases that incorporate a baffle and these, together with other mass flow ratios (designated as Cases 6, 7 and 8) are shown in Table 5.3.

TABLE 5.3 Variation in Recirculation Ratio for Cases 3 to 8

Case No.	Mass Flow Rate (kg/s) Baseplate $\dot{m}_b$	Mass Flow Rate (kg/s) Primary Jet $\dot{m}_p$	Mass Flow Ratio $\dot{m}_b/\dot{m}_p$	Upstream Recirc. Ratio $\dot{m}_r/(\dot{m}_b + \dot{m}_p)$
4	0.107	0.774	0.138	0.257
3	0.151	0.774	0.195	0.224
6	0.151	0.302	0.50	0.155
7	0.151	0.151	1.00	0.106
8	0.151	0.121	1.25	0.087
5	0.151	0.098	1.54	0.068

These results are shown graphically in Figure 5.5.10 and show a successive reduction in the mass flow entering the primary zone as the strength of the primary jet is decreased. The variation is non-linear with the highest rates of reduction occurring for mass flow ratios less than 0.5. In practical combustion chamber design it is desirable that variations in mass flow ratio caused by, for example, flight conditions of an aircraft, should not affect the recircualtion strength which is closely related to combustion performance.

The extent to which the normal trajectory angle of the primary jets affects the upstream recirculation ratio is investigated in the next chapter where a similar exercise is performed with a model incorporating an annulus. In this case the injection angle is not fixed and is a function of the local pressure field around the primary port.

5.6 DISCUSSION AND SUMMARY

The previous section has described comparisons between measurement and calculations for two, three-dimensional configurations including variations in boundary conditions. In this section it is necessary to relate this work to previous work, calculations in general, and practical combustion chamber design.

The advances of the three-dimensional work, over that covered in two-dimensions has been an increase in physical realism, in using discrete jets, and a determination of the sensitivity of the numerical model to inlet and geometric boundary condition changes. This has shown that important qualitative variations can be predicted even though some qualitative discrepancies still exist. In the finest grid distribution, for the two-dimensional case, the remaining discrepancies were attributed to the wall functions used in determining the size of the recirculation region just downstream of the slot jet. The use of discrete jets, however, does not produce such a large blockage effect as flow can travel between the jets and, hence, the downstream recirculation zones are less influential physically. Therefore errors in downstream profiles, for the three-dimensional cases, are not mainly caused by the inaccuracies of the wall function treatment. However, errors do accrue from the turbulence model and from economic limitations on using very fine grid distributions. The two-equation turbulence model, as was discussed in Chapter 3, does not account for the streamline curvature effects on turbulence generation as the jets bend downstream and this will affect the calculated mean velocity profiles. The finest grid distribution used approximately three times the number of grid nodes than the finest two-dimensional grid; however each axial plane (27 x 19) within the three-dimensional grid used less nodes than for the two-dimensional grid (37 x 40). Therefore, the degree of pressure resolution in any one plane of the three-dimensional grid is inferior to the two-dimensional geometry and, consequently, greater inaccuracy is inevitable in any three-dimensional calculation. The three-dimensional calculations were run on an IBM 360 computer (because of the storage limitations of the CDC 6600 computer used for the two-dimensional calculation) requiring three times the storage capacity and a five fold increase in computer time. The absolute limit to the grid size is the storage capacity of the computer and therefore the use of very fine grid sizes must await more efficient computers. However, industry does own large computer facilities and can perform calculations to extract qualitative information with parametric studies.

Further calculations were performed to investigate the primary zone recirculation strength for various inlet mass flow ratios. This is an example of using the calculation procedure to provide data for a parametric study and a conventional design method. The study showed that a successive decrease in primary jet mass flow rate reduced the primary zone recirculation strength, however the relationship was not linear, the rate of reduction decreasing for higher mass flow ratios.

In conclusion, for this part of the work, the numerical model has been able to adequately calculate simplified three-dimensional flows with direct applications to practical combustion chambers. The single important omission is the effect of the annulus and it is to this aspect of combustion chamber design that the work in the next chapter is directed.

CHAPTER 6

A THREE-DIMENSIONAL MODEL WITH AN ANNULUS

6.1 INTRODUCTION

6.1.1 Incorporating the Annulus

The three-dimensional combustion chamber model introduced and discussed in Chapter 5 concentrated on the idealisation of the primary zone and the extent to which the complex flow interactions can be calculated numerically. Less idealistic experimental models, used by other workers (e.g. Jones et al, 1977), have provided data for corresponding numerical calculations. In these investigations both primary and dilution zones were simulated and the jets were assumed to enter the flame tube perpendicularly. In general, this has been a fair assumption because the jets were supplied, under pressure, from a large plenum chamber where the axial velocity of the flow is zero. However, in practical combustion chambers, the width of the annulus which surrounds the ports is relatively small and, consequently, there exists, within the annulus, a range of axial velocities from small values, downstream of the entrances to the ports, to high values between ports.

The flow in the annulus has been simulated one-dimensionally by Bruce et al (1980) where the ports are assumed to be slots of infinite length and the calculation requires the prescription of the local static pressure at each port. The outcome of this calculation is a set of mass flow rate and jet entry angle values for each port and these are subsequently used as boundary conditions for a three-dimensional numerical calculation. Although this approach increases the realism of the calculation the detailed flow structure in the annulus remains unknown and the dependence on prescribed local static pressures, which are not known a priori, subject the values of jet mass flow and entry angle to some uncertainty.

The work in this chapter increases the realism of the investigations made so far by measuring in the annulus to determine the degree of three-dimensionality of the flow; in the calculations, the annulus is incorporated within the calculation domain so that, again, the three-dimensional structure may be obtained without recourse to prescribing the pressure. Further to this, the individual port mass flow rates and jet entry angles are determined from the local calculated pressure distribution. In comparison to practical combustion chambers the geometry still remains idealised in that such devices as cooling film slots, plunged holes, nozzle guide vane bleed or exit nozzle contraction are omitted. However, this does not preclude them from future work and this is discussed in section 6.7.

6.1.2 Outline of the Work

The water model used for the experimental work is described in section 6.2 and differs from the simpler models of Chapter 5 by incorporating an annulus and dilution ports. Although still idealised in detailed design in not having, for example, film cooling slots or a nozzle, the model combines the influences of the main design zones described in section 1.2.3. The measurement procedure (section 6.3) is similar to that described previously in Chapters 4 and 5 where distributions of mean axial velocity and normal stress were measured using laser Doppler anemometry. One particular advantage over the non-annulus model of Chapter 5 is the accessibility near ports, even allowing measurements to be taken within the ports, due to the absence of primary tubes and flexible feed tubes.

The modifications to the calculation procedure (section 6.4) to accommodate the annulus are similar to the two-dimensionalcase described in Chapter 4. However, whereas in the two-dimensional case the total annulus flow entered the slot ports, in this case the flow in the annulus divides at the primary ports, some entering as primary jets the rest passing downstream in the annular passage to supply the dilution ports. The mass flow entering the primary ports is, therefore, determined solely by the calculated local pressure distribution and, consequently, is a severe test of the calculation procedure. Comparisons of calculated and measured mean axial velocity are given in section 6.5 with a description of the calculated distributions of mean radial velocity and turbulence kinetic energy. The sensitivity of the flow to changes in boundary conditions is assessed with reference to the primary zone recirculation strength and influences on the annulus flow distribution in section 6.6. A discussion, including the relationship between the model and a practical combustion chamber, and a summary are given in section 6.7 which completes the chapter.

6.2 DETAILS OF THE MODEL

6.2.1 The Geometry

The model, which was made of cast acrylic, is shown in Figure 6.2.1. The exterior tube, which formed the outer wall of the annulus, was flanged at each end and bolted to flanges on the delivery and exit tubes in the water rig. The model flame tube was bolted inside the exterior tube, at the downstream end, into an accurately machined slot ensuring an evenly spaced annular passage. The model flame tube consisted of a baseplate, a baffle, to simulate a fuel vaporiser inlet, and two sets of four equi-spaced plain circular holes representing primary and dilution ports. Plunged or chuted holes and film cooling rings were not incorporated due to limitations in the size of the model and the desirability of only adding a small number of complications each time. A central tube, connected to the upstream side of the baseplate, was used to provide the baseplate inlet with a proportion of the total water flow; the rest flowed into the annulus and through the primary and dilution ports. Downstream of the dilution ports the annulus was blocked so that neither cabin air bleed (on aircraft) nor nozzle guide vane cooling flow was simulated. The model was designed so that it could be rotated through 45^{o} intervals allowing velocity values to be measured on planes between ports ($\theta = 45^{o}$) and through the centres of ports ($\theta = 0^{o}$). A preliminary investigation was carried out using flow visualisation to identify the main flow patterns and these are described in the next section.

6.2.2 The Flow Patterns

The general flow patterns for each plane, $\theta = 0^{o}$ and 45^{o}, are shown schematically in Figure 6.2.2. Those in the primary zone are similar to the non-annulus cases (Figure 5.2.3) where the primary jets meet at the centre-line and flow upstream to the baffle. A recirculation region is formed in the primary zone in front of the baffle and flow travels downstream, out towards the flame tube wall, between the primary jets. In the dilution section, the jets do not penetrate to the centre of the tube due to the high momentum of the mainstream flow which bends the dilution jets downstream. Flow visualisation in the annulus was not possible because of the high velocities.

6.3 THE MEASUREMENTS

The measurements of mean axial velocity $\overline{U}$ and the normal stress $\overline{u^2}$ were obtained with the laser-Doppler anemometer and signal processing equipment described in Chapter 2. The position of the measuring locations are shown in Figure 6.3.1. The plane through the ports ($\theta = 0^{o}$) comprised eighteen axial measuring locations and twelve radial measuring locations. The plane between ports ($\theta = 45^{o}$) comprised twenty-three axial measuring locations and twelve radial measuring locations. Contours of mean axial velocity for both planes are shown in Figure 6.3.2; the more important aspects of the flow are now described:

(i) Regions in the flow upstream and downstream of the primary and dilution ports at radii less than $^r/R \simeq 0.4$ exhibit axisymmetric behaviour. For example, the $\bar{U} = 0.0$ m/s contour upstream of the primary jets ($0.0 > {}^x/D > 1.0$), the 1.5 m/s contour between primary and dilution jets ($^x/D \simeq 1.5$) and the 1.5 m/s contour downstream of the dilution jets are very similar in both planes. However in the annulus and at $^r/R > 0.5$ variation is extensive.

(ii) Near the inner flame tube wall in the primary zone the blockage to the downstream flow is shown by the shapes of the $\bar{U} = 0.75$ m/s and 0.5 m/s contour. The 0.75 m/s contour at $\theta = 45^o$ extends to $^x/D \simeq 0.8$, whereas in the $\theta = 0^o$ plane velocities of this magnitude do not occur beyond $^x/D = 0.5$. The flow travelling downstream between the primary ports is indicated by the $\bar{U} = 0.5$ m/s contour in the $\theta = 45^o$ plane. This contour in the $\theta = 0^o$ plane shows the influence of the primary jet as it enters the flametube.

(iii) The influence of the dilution jets on the main stream flow is indicated by the $\bar{U} = 1.0$ m/s contour at $^x/D = 2.0$ and further downstream. Although the dilution jets do not penetrate to the centre-line they produce a blockage that extends from the flame tube wall inwards. As a consequence the radial extent of the $\bar{U} = 1.0$ m/s contour at $^x/D \approx 2.0$ is smaller ($^r/R \approx 0.4$) in the $\theta = 0^o$ plane than in the $\theta = 45^o$ plane ($^r/R \approx 0.9$). Further downstream, however, the flow tends towards axisymmetry.

(iv) Asymmetries in the annulus flow tend to occur near the primary and dilution ports. Upstream of the primary ports the flow is axisymmetric, and remains so, until approximately one port diameter upstream. At this location some flow transfers from the $\theta = 45^o$ plane to the $\theta = 0^o$ plane; this is indicated by the reduction in width of the $\bar{U} = 1.0$ m/s contour at $^x/D \approx 0.8$. Just downstream of this location ($\theta = 45^o$)

the $\bar{U}$ = 1.0 m/s contour then increases in width indicating that an increase in velocity takes place between the primary ports. An increase in velocity is also shown in the $\theta = 0^o$ plane downstream of the primary ports where indicated by the $\bar{U}$ = 0.5 m/s contour. At the dilution port, the flow is again transferred from the $\theta = 45^o$ to the $\theta = 0^o$ plane where, due to the annulus blockage further downstream, a region of negative velocity is produced. The annulus, therefore feeds the dilution port from downstream as well as upstream.

(v) The division of mass flow between primary and secondary ports was determined by integrating the mean axial velocity profiles situated between the axial locations of the ports. Although subject to inaccuracies, due to the assumption of a linear variation between the $\theta = 0^o$ and 45^o planes, the division was approximately equal between primary and secondary ports.

In comparison with the non -annulus cases described in Chapter 5 the average primary jet trajectory angle is shallower i.e. the region of high axial velocity gradient, which characterises the jet on the centre-line, is at $^x/D = 1.2$ for the annulus case and at $^x/D = 1.05$ for the non-annulus cases. This implies a reduction in the average jet angle by 15^o to 20^o. The recirculation region just downstream of the primary port, where the jet separates from the edge of the port, behaves similarly to that in the non-annulus case i.e. producing, at these mass-flow ratios, much less blockage to the flow than the two-dimensional slot jet described in Chapter 4.

Contours of measured normal stress for both planes ($\theta = 0^o$ and 45^o) are shown in Figure 6.3.3. A greater degree of asymmetry is shown in the primary zone ($0 > {}^r/R > 0.6$) than was exhibited for contours of mean velocity. This may be due, in part, to some asymmetry in the inlet conditions from behind the baffle. Added to this, however, is the influence of the primary jet blockage ($\theta = 0^o$) which reduces the mean velocity in this plane ($^r/R > 0.8$) producing circumferential flow towards the $\theta = 45^o$ plane. On the centre-line, at the point where the primary jets meet, a region of high normal stress is exhibited in both planes. This occurs at same axial position ($^x/D = 1.2$) as the region of high mean axial gradients discussed previously. The primary jets produce high values of normal stress, especially towards the downstream side of the port. This is due to the separation of the jet from the chamber wall and the resulting shear layer; these effects were also measured in the previous two and three-dimensional investigations. The contours in the region between primary and dilution ports are broadly similar. The peaks in the $\overline{u^2} = 0.15\ m^2/s^2$ contour indicates the residual shear from the upstream primary jets as they merge in this region. The only significant upstream influence of the dilution jets, on the symmetry of the contours, occurs at $^x/D = 1.75$ where the higher normal stress values in the $\theta = 0^o$ plane are distributed over a wider radius. In the $\theta = 45^o$ plane the flow is not restricted by the dilution jets so far upstream and the normal stress does not rise until an axial station in the middle of the dilution port is reached. The dilution jets produce high values of normal stress similar to that of the primary jets although they are more evenly distributed in the port due to the lower overall axial velocity at this point. Downstream of the dilution ports there is a region of high normal stress in both planes due to the interaction of the mainstream with the dilution jets.

These measurements indicate that the water flow is representative of the aerodynamic behaviour in practical combustion chambers. Compared to the non-annulus case, the primary zone is fed via primary jets that have their mass flow rate and initial trajectory angle determined by the local pressure distribution at the primary port. The behaviour in the dilution section is characteristic of practical combustion chambers where a high rate of mixing is required to cool the combustion products to produce an even temperature distribution.

The behaviour of the flow in the annulus, itself, is also of direct relevance to the practical case, where the proportions of the mass flow for each port are determined,as are the detailed flow structures around the ports. These are particularly important in ascertaining whether low rates of heat transfer occur and, consequently, local regions of high temperature on the flame tube wall. The incorporation of the annulus, primary and dilution ports into the calculation scheme is described in the next section.

6.4 DETAILS OF THE CALCULATIONS

6.4.1 The Grid

The finite-difference grid is shown superimposed on the model geometry in Figure 6.4.1. As in the non-annulus cases, the symmetry of the model geometry and boundary conditions allows the solution domain to be restricted to a 90^0 sector in the circumferential direction. The solution domain extends three flame tube diameters downstream from the baseplate with the highest concentration of grid nodes located near the primary and dilution ports. The grid sizes used ranged from 1088 (8 x 8 x 17) to 6000 (20 x 10 x 30) grid nodes. In the radial direction, for the finest grid distribution, five grid nodes are used to define the annulus. Due to limitations of the cylindrical polar co-ordinate system, the primary and dilution ports are of square section with areas equal to those of the circular ports of the experimental model. This aspect is now briefly discussed, together with the influence of grid node distribution within each port.

Due to limitations on storage available the number of grid nodes investigated varied from two to twelve nodes per port. In order to assess the effect on typical flow parameters within the primary port, the values of primary to annulus mass flow ratio ($\dot{m}_b/\dot{m}_a$) and the initial primary jet angle

(α^o) were calculated for each and are displayed in Table 6.1.

Table 6.1 Primary Port Flow Variation for Three Grid Sizes

No. of nodes in Primary Port	Primary to annulus Ratio ($\dot{m}_b/\dot{m}_a$)	Initial Jet Angle (α^o)
2	0.331	62.3
6	0.445	69.1
12	0.451	69.9

The variation in the values shows that both the mass flow rate through the port and the jet trajectory angle vary by only small amounts for between six and twelve nodes in the port. However, although locally grid independent, the differences between the port shapes in the calculations (square) compared to the experiment (circular) will produce some disagreement between calculated and measured values in other regions within the model. A detailed study of port configurations and their influence on the jet coefficient of discharge (defined as the ratio of measured flow to theoretical flow through the port) has been made by Dittrich (1958). This work shows that for a wide range of annulus flow rates the difference in the coefficient of discharge for circular and square flush holes is only 1%; therefore it is unlikely that large errors in the calculation of $\dot{m}_b/\dot{m}_a$ contribute to inaccuracies elsewhere. However, the predictions of the spreading rate and shear layer regions are likely to be in error and cause inaccuracies within the primary zone. This is examined after comparisons have been presented in section 6.5.

6.4.2 The Boundary Conditions

The boundary conditions for the calculations were taken mainly from the measurements. The inlet values for the axial mean velocity and normal stress were measured in the annulus at $^x/D = 0.25$ on the two circumferential measuring planes ($\theta = 0^o$ and 45^o). As it was not known how the velocity varied between the planes the two sets of data were averaged and applied in the calculation for the whole 45^{o} sector. The inlet values for turbulence kinetic energy were calculated from the normal stress values, assuming isotropy and applied in a similar manner to the velocities. The boundary conditions for the energy dissipation rate were determined from the turbulence kinetic energy values assuming a length scale proportional to the annulus width (see eqn. 3.12). The boundary conditions for the baseplate were assigned, as in Chapter 5 for the non-annulus three-dimensional geometries with a baffle, from measurements taken upstream (2 diameters) in the baseplate tube and modified to reflect the change in flow area.

6.4.3 The Application of the Numerical Model

A similar procedure to that described in Chapter 5 for the non-annulus three-dimensional calculations was used here. Thus the equations for the three mean velocities, pressure, turbulence kinetic energy and energy dissipation rate were again solved using the technique outlined in Chapter 3.

The degree of grid fineness in the primary zone is similar to the non-annulus case but further downstream, and in the annulus, more nodes were necessary so as to define the dilution section and annulus. The finest grid distribution used, 6000 (20 x 10 x 30) grid nodes, required about 700 iterations to obtain a satisfactory converged solution (with continuity errors less than 0.5%). The increase in the number of iterations is due to the destabilising effect of solving the equations with internal walls and small ports which introduce more degrees of freedom that have to be decided internally by the solution (e.g. determination of the division between primary and dilution mass flow). The restricted linkage between the solution in the annulus and in the flame tube also increases the number of iterations required for convergence.

The magnitudes of the cell Peclet numbers in the flame tube and in the annulus, on the centre-line of the primary port all exceed $|2|$ in value in the axial and radial directions; hence upstream differencing is used in the calculation of the finite-difference coefficients. False diffusion is therefore likely, although this depends, as has been discussed before in Chapter 4, on the main flow direction not being aligned to any grid direction and the absence of pressure dominance in the momentum equations. An examination of the flow in this region, for these criteria, shows that whilst the primary jet, and hence the main flow, is not aligned with either the axial or the radial grid direction the pressure terms in both the axial and radial momentum equations are dominant. Therefore it is unlikely that false diffusion contributes anything to the overall inaccuracies in this region. These factors are discussed later (section 6.7) with reference to overall accuracy and the use of calculation techniques in the design of practical combustion chambers.

Further application of the calculations comprises a study of parameters important to practical combustion chambers and is discussed in section 6.6. This includes the variation in upstream recirculation, as was studied for the non-annulus cases, and also studies of jet trajectory angle and primary jet strength.

6.5 THE CALCULATED RESULTS

6.5.1 Comparison of Measured and Calculated Axial Mean Velocity

Calculated contours of mean axial velocity are shown in Figure 6.5.1 for planes between ($\theta = 45^o$) and through the jet centre-line ($\theta = 0^o$). These may be compared to the measured contours (Figure 6.3.2) to gain an overall estimation of agreement.

The calculated velocities in the primary zone (i.e. $0 < {}^X/D < 1.25$) agree qualitatively with the measured contours. However, quantitatively, a larger proportion of the primary jet flow travels upstream and, in the calculations, produces a larger recirculation region as shown by the $\bar{U}$ = 0.0 m/s contour which extends radially outwards by about 50% more than the measured contour. This effect is also shown by the radial positions of the $\bar{U}$ = 0.5 and 0.75 m/s contours. In the axial direction good qualitative agreement on the centre-line positions of the $\bar{U}$ = 0.0 and 0.5 m/s contours is shown. The main measured difference between the $\theta = 0^o$ and 45^o planes, namely the reduction in axial length of the $\bar{U}$ = 0.75 m/s contour, is also featured in the calculations.

The mean axial velocity contours in the annulus are in good qualitative agreement between measurement and calculation. In particular, the position and shapes of the $\bar{U}$ = 0.0 and 0.5 m/s contours near the dilution port ($\theta = 0^o$) are well predicted showing the region of backflow into the dilution port. Upstream, at the primary port, the contours are in qualitative agreement but show that, in the calculations, a greater proportion of the annulus flow travels downstream to the dilution port than was measured. Thus the calculated primary port mass flow is less than in the experimental case. In the $\theta = 45^o$ plane the measured and calculated contours, $\bar{U}$ = 0.5 and 1.0 m/s, agree although the detailed contour shapes (near the port) are not predicted. The region between the primary and dilution zones ($1.25 < {}^x/D < 1.75$), again, shows only qualitative agreement between measurement and calculation. The calculated axial velocities at the centre-line are underpredicted whilst the outer radial regions tend to be overpredicted. This is a direct result of the lower calculated primary port flow and the higher proportion of recirculating flow. The calculated contours in the dilution zone, and further on downstream, also exhibit lower centre-line velocities and higher velocities in the outer radial regions. This is due to the higher proportion of flow through the dilution ports, predicted in the calculation, than was the case in the experiment.

The effect of errors in calculating the primary port mass flow is also exhibited in the radial profiles of axial mean velocity, some of which are shown in Figure 6.5.2. The profile at $^{x}/D = 0.5$ shows the over-prediction of the centre-line mean axial velocity which extends radially outwards, particularly for the $\theta = 45^{o}$ plane. The profile at $^{x}/D = 1.0$, the primary jet centre-line, shows the greatest disagreement in the port and annulus; a finer grid distribution in the port did not improve the agreement and must be attributed to the local differences in port shape, this is discussed in section 6.7. In the primary port the axial velocity is under-predicted, whilst in the annulus the axial velocity is over-predicted. The profile at $^{x}/D = 1.5$, lies between the primary and dilution zones and shows an under-prediction of the centre-line axial velocity by about 40%; this is directly attributable to the calculated lack of primary jet mass flow. The profile in the annulus, for the $\theta = 0^{o}$ plane indicates the over-prediction of the mass flow in the annulus, downstream of the primary port. At the centre-line of the dilution port ($^{x}/D = 2.0$) the profile shows, again, the underpredicted centre-line axial velocity and over-predicted velocities near the flame tube wall. Further downstream at $^{x}/D = 2.33$ the over-predicted dilution jet mass flow is shown at $^{r}/R \simeq 0.7$ where the measured axial velocity is smaller. The calculated centre-line value of the axial velocity is about 20% below that of the measured value.

Other, more general parameters, used by combustion chamber designers may also be determined from the calculations and estimated from the measurements to further test the degree of agreement. For example, the average primary jet trajectory angle can be defined by the position, on the centre-line, of the maximum velocity gradients; for the measurements this was given as $^{x}/D = 1.2$ (in section 6.3), for the calculations this occurs at $^{x}/D \simeq 1.1$. Another important parameter is the division in mass flow between primary and dilution jets. Estimation from measurements gives the primary jet mass flow m_p = 55% ($\pm$5%) of the total mass flow whereas the calculated value of m_p = 45%. These parameters will be examined for further calculations in section 6.6.

6.5.2 Calculated Results for Radial Velocity and Turbulence Kinetic Energy

The calculated contours of mean radial velocity are shown in Figure 6.5.3. These illustrate, clearly, the primary and dilution port jets in the $\theta = 0^o$ plane and that, whereas the primary port jets impinge on the centre-line causing a negative region in the $\theta = 45^o$ plane, the dilution jets do not impinge on the centre-line. These contours may also be compared to the radial velocity contours calculated in the previous work. The contours for the two-dimensional slot jet (Figure 4.7.2) show that the maximum radial velocity occurs directly adjacent to the downstream lip of the slot. In the present case the maximum radial velocities tend to occur between the centre and the downstream lip of the port. The contours for the non-annulus three-dimensional case (Figure 5.5.6) show similar features to the present case in the primary zone near the baffle. However, the larger trajectory angle of the primary jet is clearly contrasted.

The calculated contours of turbulence kinetic energy are shown in Figure 6.5.4 and indicate the main regions of turbulence energy production. High production is characteristic of regions of mixing in combustion chambers; in the primary zone, high rates of mixing ensure fast fuel breakdown and in the dilution zone, high rates of mixing produce flat temperature profiles at the chamber exit. These are, as found from the previous studies, on the centre-line of the primary jet (extending into the port) and also at the flame tube centre-line where the jets impinge. The same distribution, although at smaller magnitudes, occurs in the dilution zone; this has also been shown in the work by Bruce et al (1980). The calculated contours of turbulence kinetic energy may also be compared to the measured contours of axial normal stress (Figure 6.3.3). Although in a three-dimensional, recirculating flow these two quantities are not directly comparable, some qualitative agreement between them should be apparent where the axial normal stress is high. For example, both sets of contours show a maximum region on the centre-line where the primary jets impinge including the greater radial extent in the $\theta = 45^o$ plane compared to the $\theta = 0^o$ plane. Also the behaviour in the primary and dilution ports of the calculated ($k = 0.05\ m^2/s^2$) and measured ($\overline{u^2} = 0.1\ m^2/s^2$) contours is very similar, extending, in both sets of contours, out into the annulus.

6.6 FURTHER CALCULATIONS

The parametric study performed for the non-annulus cases, for various inlet mass flow ratios, was restricted to investigating the upstream recirculation ratio, only, due to the fixed initial trajectory angle of the primary jet. In the present case, investigations of several important features, of interest to combustion chamber designers, can be made by varying the ratio between baseplate and annulus (and hence primary jet) mass flows. These features include: upstream recirculation ratio, mass flow division between primary and dilution ports, length of primary zone and initial trajectory angles for primary and dilution jets. The inlet mass flow ratios ($\dot{m}_b/\dot{m}_p$), defined as for the non-annulus cases as the ratio of baseplate to primary jet mass flow rate, cover a similar range to that of the non-annulus cases in order to facilitate comparison.

The inlet mass flow ratio for each calculation is given in Table 6.2 where the individual cases are named A, B, C and D; Case B corresponds to the case measured and calculated in sections 6.3 to 6.5. Each parameter given in the table is represented graphically in Figures 6.6.1 to 6.6.4.

Table 6.2 A Parametric Study

Case	$\frac{\dot{m}_b}{\dot{m}_p}$	$\dot{m}_a$ (kg/s)	$\frac{\dot{m}_r}{\dot{m}_p + \dot{m}_b}$	$\alpha_{initial}$		$\frac{\dot{m}_p}{\dot{m}_a}$
				pri.	dil.	
A	0.36	0.442	0.178	71.0	80.9	0.449
B	0.60	0.442	0.126	69.9	80.4	0.445
C	1.03	0.442	0.092	67.8	79.2	0.439
D	1.56	0.442	0.092	65.5	77.7	0.435

Figure 6.6.1 shows the variation in upstream recirculation mass flow ratio $\left(\frac{\dot{m}_r}{\dot{m}_p + \dot{m}_b}\right)$ with increase in inlet mass flow ratio. In contrast to the non-annulus cases, the rate at which the recirculation ratio decreases is approximately zero for $\dot{m}_b/\dot{m}_p = 1.0$ to 1.5. The initial primary and dilution jet trajectory angles ($\alpha_{initial}$) for each case are shown plotted in Figure 6.6.2 together with the primary jet trajectory angles for the non-annulus cases. The decrease in jet angle for increasing values of $\dot{m}_b/\dot{m}_p$ is similar for both primary and dilution jets. This is in contrast to the non-annulus cases, where there is less variation in primary zone length, due to the fixed inlet jet trajectory angle. The primary jet to annulus mass flow ratio ($\dot{m}_p/\dot{m}_a$) decreases for increasing $\dot{m}_b/\dot{m}_p$ so that the dilution jet mass flow increases at the expense of the primary jet (Figure 6.6.3).

The results above indicate that the mass flow rate of the primary jet, and its trajectory angle, both decrease for values of $0.36 < \dot{m}_b/\dot{m}_p < 1.5$ implying a reducing capacity to recirculate upstream into the primary zone. However, in contradiction, the upstream recirculation ratio for values $1.0 < \dot{m}_b/\dot{m}_p < 1.5$ do not decrease but remain approximately constant. Therefore an increasing proportion of the upstream recirculation must be contributed by the baseplate flow being recirculated back from downstream of the cross-stream plane used to integrate the recirculating mass flow rate (Figure 6.6.1).

6.7 DISCUSSION AND SUMMARY

In relation to previous work, in both two and three-dimensions, the work in this chapter has introduced a further increase in physical realism by incorporating the annulus and both primary and dilution ports. The annular two-dimensional work provided some insight to combustion chamber flow behaviour but was hampered by the unrealistic slot jet in simulating a row of discrete jets. The non-annular three-dimensional work, although significantly more realistic due to the provision of discrete jets, lacked the sensitivity of practical chamber flows because of the fixed initial trajectory angle of the primary jets. The work in this chapter has removed these restrictions.

In comparing the perforance of calculations for the three-dimensional geometries, both with and without an annulus, the annulus geometry requires up to twice the number of iterations to achieve the same state of convergence. This has been attributed to the presence of internal walls and small ports that reduce the linkage between the solution in the annulus and in the flame-tube. The agreement between calculated and measured mean axial velocities has also deteriorated from a maximum centre-line error of 30% for the non-annulus case to 40-45% for the case with an annulus; however, these values are given as an approximate comparison and should not be taken out of context. Three-dimensional flows cannot be characterised by one simple parameter and therefore an appreciation of the inaccuracies between a calculated and a measured flow must be based on a comprehensive view. The main reason for the deterioration in agreement for the geometry with an annulus stems from the primary ports. The shape of the ports used in the calculations is square whereas in the experimental model they were circular. This is a limitation of the grid system and, although (as noted in section 6.4.1) the coefficients of discharge for each port shape are almost identical, the velocity profiles and spreading rates of a sqaure and a round three-dimensional jet will not be the same. The outcome of this difference is the over-prediction of the mass flow flowing into the primary zone causing an under-prediction of the downstream centre-line velocity (over and above that of the non-annulus cases).

The work in this chapter has shown that calculations of the overall isothermal flow distributions for a modern combustion chamber are feasible but await further improvements to the accuracy and efficiency of the calculation scheme; this aspect is discussed later. The practical uses of the calculation scheme, in its present state of development, is limited to qualitative investigations of major combustion chamber components. For example, parametric studies may be undertaken for the overall flow within the flame tube including cooling film slots and exit nozzle provided that the port entry conditions are accurately known. This is especially important and has been highlighted in the parametric studies of Chapter 5 and of the present chapter where significant qualitative variations in the upstream recirculation behaviour were shown to be different depending on the port entry conditions. The specification of, for example, primary jet entry angles of 90^0 for a practical combustion chamber (regardless of what the actual angle might be) will not produce meaningful calculated results.

The limitations to more extensive use of the calculation scheme for predicting, for example combusting flows and wall temperatures with little quantitative error, concern each of the component parts of the calculation scheme, i.e. the grid system, the differencing scheme, the solution algorithm and the combustion and turbulence models. It is expected that some of the deficiencies can be remedied in a short timescale but some require extensive research. The use of cartesian or cylindrical polar grid systems with simply shaped boundaries severely limits the application of the calculation scheme to modern combustion chambers which, due to the constraints imposed upon engine manufacturers, are made in a wide variety of complex shapes. It is therefore necessary to use a grid system capable of describing an irregular three-dimensional boundary without discarding the convenience of the orthogonal co-ordinate system used at present; this must be accomplished without incurring substantial extra storage. The present differencing scheme, which was upstream coefficients in regions where the cell Peclet number is greater than |2|, is numerically stable but does introduce false diffusion. In some regions of combustion chamber flows the dominance of pressure usually dictates that any numerical diffusion is negligible in equations of velocity or turbulence kinetic energy, however, looking ahead to combusting flows, equations for temperature or chemical species mixture fraction in these regions (which do not have pressure gradient or equivalent source terms) will be dominated by false diffusion. Some schemes that eliminate or severely reduce false diffusion have been outlined in Chapter 3, of these the most promising improvement would be the use of a "skewed" upstream scheme which takes into account values at a greater range of nodes (Raithby 1976a). In order not to incur the higher cost of increased computational running time this scheme should be used as well as improved equation solvers such as those suggested by McDonald (1979). These suggestions could be incorporated into the calculation scheme in a short time scale, the combustion and turbulence models require much longer. Research into finite-rate reaction combustion models is still in progress and requires substantial testing on simple flows, such as diffusion flames, before incorporation into the present scheme. As has been stated,a radically new turbulence model is a long term prospect and care must be exercised before discarding the conceptually simple but easily applicable and economic eddy viscosity models. Further investigation into the physical basis of streamline curvature in complex three-dimensional flows would reduce the ad hoc nature of some of the schemes, described in Chapter 3, already proposed for two-dimensional geometries.

CHAPTER 7

CONCLUSIONS

7.1 CONTRIBUTIONS OF THE WORK

The main contributions of the work, presented in this thesis, are outlined as follows:

(i) Detailed measurements, of axial mean velocity and normal stress, were taken for flows in a range of water model combustion chambers. The measuring technique used a laser Doppler anemometry system in forward scatter mode with a rotating diffraction grating. Each water model in the range was designed to feature the main elements of practical combustion chambers, starting with a very simple two-dimensional, axisymmetric model and building up, finally, to a three-dimensional model with primary and dilution ports and an annulus. The measurements were taken so as to provide data for comparison with a numerical calculation technique.

(ii) A numerical calculation technique has been modified to accommodate internal walls in the calculation domain and applied to each of the model combustion chamber geometries. The calculation technique was used to predict the internal flow variables of: mean velocity, pressure,turbulence kinetic energy and energy dissipation rate for each of the geometries using, in the main, measured boundary conditions. The degree of agreement between measured and predicted axial velocity has been assessed in each case. The effects of varying the local geometry or boundary conditions on the flow structure has been discussed so as to illustrate, in a simple manner, the benefits of the technique for design and research of practical combustion chambers.

In detail, the conclusions for each of the models is outlined below:

(i) The two-dimensional, axisymmetric model was used to test, initially, the viability of using both the measuring and calculation techniques on a geometry with an annulus. The degree of agreement between measured and calculated axial velocity (maximum 17% error) was found to depend upon the resolution of steep pressure gradients adjacent to the slot. Expected numerical errors, such as false diffusion, were investigated but were not found to be significant due to pressure dominance in the region of the slot, the main area of interest. A detailed investigation of the effects of the slot and annulus width showed that an increase in annulus width or a decrease in slot width reduced the upstream recirculation strength, whilst a decrease in annulus width increased the recirculation strength. These effects were caused by separation regions set up at the leading edge of the slot.

(ii) A simple, three-dimensional model was designed to introduce discrete primary jets, and a baseplate inlet flow, in order to increase the practical relevance of the geometry. An annulus was not incorporated so as to ensure a controlled entry angle for the primary jets and this was achieved by using perpendicularly mounted tubes. Two types of inlet baseplate flow were investigated, a simple axial jet and a baffle. One set of measurements was made for the simple jet and three sets, with different inlet conditions, were made for the baffle baseplate inlet to provide data for assessing the sensitivity of the calculation procedure. The calculated mean axial velocities were in good qualitative agreement (maximum quantitative errors of 30%) with the measurements in all cases showing the ability of the calculation procedure to predict the effect of local varaitions on the flow structure. A parametric study of the effect of varying the ratio of baseplate mass flow to primary jet mass flow ($\dot{m}_b/\dot{m}_p$) and showed that an increase, in the range $0.14 < \dot{m}_b/\dot{m}_p < 1.54$, reduced the recirculation ratio $\frac{\dot{m}_r}{\dot{m}_b + \dot{m}_p}$ monatonically from 0.26 to 0.07.

(iii) The most complex three-dimensional model comprised an annulus, a baseplate baffle and primary and dilution ports. This configuration represented a good approximation to a simple combustion chamber where the "design zones" primary, dilution and annulus are all incorporated. The agreement between measured and calculated mean axial velocity was qualitatively satisfactory but quantitative agreement (maximum 45% error) was inferior to that of the non-annulus cases. The reason for the added inaccuracy stemmed from the over-prediction of the upstream flow from the primary jet which distributes the flow more evenly across the flame tube radius (for axial locations between the primary and dilution ports) than was measured. The cause of this discrepancy has been attributed to the representation of circular ports by square ports in the calculation and its affect on the jet structure. A similar parametric study to that performed for the non-annulus geometry, was undertaken to investigate: recirculation strength, initial jet entry angle, primary zone length and primary jet flow rate for values of $\dot{m}_b/\dot{m}_p$ in the range $0.36 < \dot{m}_b/\dot{m}_p < 1.56$. In contrast, for the case with an annulus the recirculation ratio $\frac{\dot{m}_r}{\dot{m}_b + \dot{m}_p}$ decreased for values of $\dot{m}_b/\dot{m}_p$ in the range $0.36 < \dot{m}_b/\dot{m}_p < 1.0$ but remained at a constant value ($\simeq 0.09$) thereafter. All the other parameters indicated a successive weakening of the primary jet for higher values of $\dot{m}_b/\dot{m}_p$, therefore the "extra" mass flow in the recirculation zone was baseplate flow being recirculated back across the plane of integration. In practical terms this would mean that for higher values of $\dot{m}_b/\dot{m}_p$ less cool air from the primary jet would be recirculated and instead a higher proportion of combustion products would recirculate.

In all cases the level of qualitative agreement can be regarded as being high enough to warrant further work and, in some cases, limited application in the design procedures of practical combustion chambers.

7.2 FUTURE WORK

Several categories of future work are envisaged for the application of laser Doppler anemometry and numerical calculation techniques in the design of practical combustion chambers.

The use of water and cold air models, in the design of new combustion chambers and for chamber development, is well established and investigations are usually based on flow sketches or pitot tube and static pressure measurements. However, some modifications to details within the combustion chamber produce variations in the flow that require a great deal more resolution than that afforded by sketches or pressure measurements. It is in this application where prudent use of laser Doppler anemometry can provide quantitative results on which to base future design decisions. A useful by-product of this approach is to provide data for subsequent comparisons with corresponding calculations.

The immediate application of the calculation technique to combustion chamber design is limited by its assumption of simply shaped boundaries and by inaccuracies caused by numerical error and the turbulence model. Unfortunately the time scales for removing these limitations differs widely; for example, a grid system using irregularly shaped boundaries, capable of describing modern combustion chambers, can be tested and developed within a few months. However, the reduction of numerical error with the use of "skewed" upwind differencing, which incurs greater computational cost, should be implemented together with more efficient equation solvers so that overall the calculation is no more expensive. The time scale for improving or replacing the turbulence model could be in terms of years as research into streamline curvature effects and "wall functions" is still in progress. If the limitations are accepted and the designer uses the predictedresults as qualitative guidance then parametric studies for simply related features of the combustion chamber can be made. For example, the effects on the local flow field of a variety of port configurations (i.e. baffles, chutes, scoops, etc.) could be calculated where empirical information is not available.

R E F E R E N C E S

ABRAMOVITCH,G.N.(1963)
"The Theory of Turbulent Jets".
M.I.T. Press

ADKINS, R.C. (1978)
"The effect of compressor exit flow distribution on air placement in annular combustors".
J. of Engineering for Power, 100, 444.

BERMAN, N.S. and DUNNING, J.W. (1973)
"Pipe flow measurements of turbulence and ambiguity using laser Doppler velocimetry".
J. Fluid Mech. 61, 289.

BOUSSINESQ, J. (1877)
"Theorie de l'ecoulement tourbillant".
Mem. Acad. Sci. 23, no.46

BRADSHAW, P. (1973)
"The effect of streamline curvature on turbulent flows".
AGARD, no. 169

BRIGHTON, J.A. and JONES, J.B. (1964)
"Fully developed turbulent flow in annuli"
J. Basic Engineering, 86, 835.

BRUCE, T.W., MONGIA, H.C. and REYNOLDS, R.S. (1979)
"Combustor Design Criteria Validation"
USARTL-TR-78-55, 1-3

BRYAN, R., GODBOLE, P.S. and NORSTER, E.R. (1969)
"Some observations of the atomising characteristics of air-blast atomisers".
Proc. Int. Propulsion Symp., Cranfield.

CHORIN, A.J. (1968)
"Numerical solution of the Navier-Stokes equations".
Math. Comp. 22, 745.

CLARE, H., GARDINER, J.A. and NEALE, M.C. (1961)
"Study of fuel injection in air breathing combustion chambers".
AGARD Manual on Experimental Methods in Combustion Research.

CLARKE, A.E., GERRARD, A.J. and HOLLIDAY, L.A. (1963)
"Some experiences in gas turbine combustion chamber practice using water flow visualisation techniques.
9th Int. Combustion Symp., New York.

DITTRICH, R.T. and GRAVES, C.C. (1956)
"Discharge coefficients for combustor-liner air-entry holes" I.
NACA TN 3663

DITTRICH, R.T. (1958)
"Discharge coefficients for combustor-liner air-entry holes" II.
NACA TN 3924.

DURST, F., MELLING, A. and WHITELAW, J.H. (1976)
"Principles and Practice of Laser Doppler Anemometry"
Academic Press.

DURST, F., and RASTOGI, A.K. (1979)
"Turbulent flow over two-dimensional fences".
2nd Symp. on Turbulent Shear Flows, London.

DURST, F. and WHITELAW, J.H. (1971)
"Integrated optical units for laser anemometry"
J. Phys. E: Sci. Instrumen. 4, 804.

DURST, F., WIGLEY, G. and ZARÉ, M. (1974)
"Laser Doppler anemometry and its application to flow investigations in the environment of vegetation".
Report No. SFB 80/EM/41, University of Karlsruhe.

EDWARDS, R.V., ANGUS, J.C., FRENCH, M.J. and DUNNING, J.W. (1971)
"Spectral analysis of the signal from the laser Doppler flow meter: time independent systems".
J. Appl. Phys. 42, 837.

EDWARDS, R.V., ANGUS, J.C. and DUNNING, J.W. (1973)
"Spectral analysis of the signal from the laser Doppler velocimeter: turbulent flows"
J. Appl. Phys. 44, 1694.

ELMHAL, G., FERM, S. and SVENSSON, S.O. (1980)
"Industrial type gas turbines for offshore applications".
J. of Engineering for Power, 102, 297.

ELLIMAN, D.G., FUSSEY, D.E. and HAY, N. (1978)
"Prediction and measurements of a turbulent, axisymmetric, ducted diffusion flame".
Int. J. of Heat and Mass Transfer, 21, 1393.

FRISWELL, N.J. (1972)
"Emissions from gas turbine type combustors"
Emissions from Continuous Combustion Systems, 161, Plenum Press.

GEORGE, W.K. and LUMLEY, J.L. (1973)
"The laser Doppler velocimeter and its application to the measurement of turbulence".
J. Fluid Mech. 60, 321.

GERRARD, A.J. (1961)
"Methods of flow visualisation by means of water"
AGARD manual on Experimental Methods in Combustion Research

GOSMAN, A.D. and PUN, W.M. (1973)
"Calculation of recirculating flows"
Lecture notes, Mech. Engineering Dept., Imperial College, London.

GREEN, A.S. and WHITELAW, J.H. (1980)
"Measurements and calculations of the isothermal flow in axisymmetric models of combustor geometries".
J. Mech. Engineering Sci. 22, 119.

HANJALIC, K. (1970)
"Two-dimensional asymmetric turbulent flow in ducts".
Ph.D. Thesis, University of London

HARLOW, F.H. and AMSDEN, A.A. (1971)
"A numerical fluid dynamics calculation method for all flow speeds"
J. Comp. Phys. 8, 197.

HARLOW, F.H. and NAKAYAMA, P. (1968)
"Transport of turbulence energy decay rate"
LA-3854, Los Alamos Science Lab., University of California.

HIETT, G.F. and POWELL, G.E. (1962)
"Three-dimensional probe for investigation of flow patterns"
The Engineer, 213, 165.

HINZE, J.O. (1959)
"Turbulence: an introduction to its mechanism and theory"
McGraw-Hill, New York.

HIRSINGER, F. and TICHTINSKY, H. (1979)
"Modelisation de zone de combustion en regime instationaire"
AGARD Conf. Proc. No. 275.

HUMPHREY, J.A.C. (1977)
"Flow in ducts with curvature and roughness"
Ph.D. Thesis, University of London.

JONES, W.P. (1971)
"Laminarisation in strongly accelerated boundary layers"
Ph.D. Thesis, University of London.

IRWIN, H.P.A.H. and ARNOT-SMITH, P. (1975)
"Prediction of the effect of streamline curvature on turbulence"
Physics of Fluids, 18, 624.

JONES, W.P., CLIFFORD, W.C., PRIDDIN, C.H. and DE CHAIR, R. (1977)
"A comparison between predicted and measured species concentrations and velocities in a research combustor"
AGARD PEP, Paper 41, Symp. on High Temp. Problems in Gas Turbine Engines. Ankara.

JONES, W.P. and LAUNDER, B.E. (1973)
"Prediction of low Reynolds number phenomena with a two-equation model of turbulence"
Int. J. of Heat and Mass Transfer, 16, 1189.

JONES, W.P. and McGUIRK, J.J. (1979)
"Mathematical modelling of gas turbine combustion chambers"
AGARD Conf. Proc. No. 275.

JONES, W.P. and McGUIRK, J.J. (1979a)
"Computation of a round jet discharging into a confined crossflow"
2nd Symp. on Turbulent Shear Flows, London.

JONES, W.P. and PRIDDIN, C.H. (1978)
"Predictions of the flow field on local gas composition in gas turbine combustors"
17th Int. Combustion Symp. Leeds.

KOLMOGOROV, A.N. (1942)
"Equations of turbulent motions of an incompressible turbulent fluid"
Izv. Akad. Nauk SSSR Ser. Phys. 6.

LAUNDER, B.E., PRIDDIN, C.H. and SHARMA, B.I. (1977)
"The calculation of turbulent boundary layers on spinning and curved surfaces"
J. of Fluids Engineering, 99, 231.

LEONARD, B.P. (1980)
"The QUICK algorithm"
Computer Methods in Fluids, Pentech.

LESCHZINER, M.A. (1980)
"A comparison between three finite-difference schemes for the computation of steady-state recirculating flows"
Report No. SFB 80/T/149, University of Karlsruhe.

LESCHZINER, M.A. and RODI, W. (1980)
"Calculations of annular and twin parallel jets using various discretization schemes and turbulence-model variants"
Report. No. SFB 80/T/159, University of Karlsruhe.

LILLEY, D.G. (1979)
"Flowfield modelling in practical combustors: a review"
J. of Energy, 3, no.4, 193.

LIVESEY, J.L., JONES, P.K., PARKER, E. and SHAW, J.P. (1960)
"Aerodynamics of tube-type gas turbine combustion chamber entry sections"
J. of Mech. Engineering Science, 2, no.3, 202.

McDONALD, H. (1979)
"Combustion modelling in two and three dimensions - some numerical considerations"
Prog. Energy Combust. Science, 5, no.2, 97.

McGUIRK, J.J. and RODI, W. (1978)
"A depth-averaged mathematical model for the near field of side discharges into open channel flow"
J. Fluid Mech. 86, 761.

McKNIGHT, D. (1979)
"Development of a compact gas turbine combustor to give extended life and acceptable exhaust emissions"
J. of Engineering for Power, 101, 349.

MELLING, A. (1975)
"Investigation of flow in non-circular ducts and other configurations by laser Doppler anemometry".
Ph.D. Thesis, University of London.

MELLING, A. and WHITELAW, J.H. (1973)
"Measurements in turbulent water flows by laser anemometry"
Proc. of 3rd Biennial Symp. on Turbulence in Liquids, Rolla, 115.

MILITZER, J., NICHOLL, W.B. and ALPAY, S.A. (1977)
"Some observations on the numerical calculation of the recirculation region of twin parallel symmetric jet flows"
1st Symp. on Turbulent Shear Flows, Penn. State University.

NOVICK, A.S., MILES, G.A. and LILLEY, D.G. (1979)
"Numerical Simulation of combustor flowfields: a primitive variable design capability".
J. of Energy, 3, no.2, 95.

NOVICK, A.S., MILES, G.A. and LILLEY, D.G. (1979a)
"Model parameter influences in gas turbine combustor design"
J. of Energy, 3, no.5, 257.

ODGERS, J. (1979)
"Combustion modelling with gas turbine engines, some applications and limitations"
AGARD Conf. Proc. No. 275.

PARNELL, E.C. and WILLIAMS, M.R. (1969)
"A survey of annular vaporising combustion chambers"
Proc. Int. Propulsion Symp., Cranfield.

PEACEMAN, D.W. and RACHFORD, H.H. (1955)
"The numerical solution of parabolic and elliptic differential equations"
J. Soc. Indust. Appl. Math. 3, 28.

PILKINGTON, G. and CARLISLE, D.R. (1968)
"Combustion aspects of industrially applied aero gas turbines"
Symp. on Technical Advances in Gas Turbine Design, Proc. I. Mech. E. 183, 3N, 9.

POPE, S.B. and WHITELAW, J.H. (1976)
"The calculation of near wake flows"
J. Fluid Mech. 73, 9.

POULSTON, B.V. and WINTER, E.F. (1957)
"Techniques for the study of air flow and fuel droplet distribution in combustion systems"
6th Int. Combustion Symp., Connecticut.

RAITHBY, G.D. (1976)
"A critical evaluation of upstream differencing applied to problems involving fluid flow"
Comp. Meth. in Appl. Mech. and Engineering, 9, 75.

RAITHBY, G.D. (1976a)
"Skew upstream differencing schemes for problems involving fluid flow"
Comp. Meth. in Appl. Mech. and Engineering, 9, 153.

ROACHE, P.J. (1972)
"Computational Fluid Dynamics"
Hermosa Pub., New Mexico.

RODI, W. (1970)
"Basic equations for turbulent flow in cartesian and cylindrical co-ordinates"
Report No. BL/TN/A/36 Mech. Engineering Dept., Imperial College, London.

RODI, W. (1972)
"The prediction of free turbulent boundary layers by use of a two-equation model of turbulence".
Ph.D. Thesis, University of London.

RUDD, M.J. (1969)
"A new theoretical model for the laser Dopplermeter".
J. Phys. E: Sci. Instrum. 2, 55.

SAWYER, R.F. (1972)
"Experimental studies of chemical processes in a model gas turbine combustor"
Emissions from Continuous Combustion Systems, 243, Plenum Press.

SCHLICHTING, H. (1968)
"Boundary-Layer Theory"
McGraw-Hill, New York.

SERAG-ELDIN, M.A. (1977)
"The numerical prediction of the flow and combustion in a three-dimensional can combustor"
Ph.D. Thesis, University of London

SIMPSON, R.L., STRICKLAND, J.H. and BARR, P.W. (1977)
"Features of a separating, turbulent boundary layer in the vicinity of separation"
J. Fluid Mech. 79, 553.

SPALDING, D.B. (1972)
"A novel finite-difference formulation for differential expressions involving both first and second derivatives"
Int. J. Num. Meth. in Engineering, 4, 551.

STEVENSON, W.H. (1970)
"Optical frequency shifting by means of a rotating diffraction grating"
Appl. Optics, 9, 649.

SWITHENBANK, J., TURAN, A. and FELTON, P.G. (1980)
"Three-dimensional two-phase mathematical modelling of gas turbine combustors"
in Gas Turbine Combustor Design Problems, Hemisphere Pub. Corp.

TACINA, R.R. and GROBMAN, J. (1969)
"Analysis of total-pressure loss and airflow distribution for annular gas turbine combustors"
NASA TN D-5385

VAN DEN BERG, B. (1975)
"A three-dimensional law of the wall for turbulent shear flows"
J. Fluid Mech., 70, 149.

VASILIĆ-MELLING, D. (1977)
"Three-dimensional, turbulent flow past rectangular bluff bodies"
Ph.D. Thesis, University of London.

VERDUZIO, L. and CAMPANARO, P. (1969)
"The air recirculation ratio in can-type gas turbine combustion chambers"
Proc. Int. Propulsion Symp., Cranfield.

YEH, Y. and CUMMINS, H.Z. (1964)
"Localized flow measurements with an He-Ne laser spectrometer"
Appl. Phys. Letters, 4, 176.

YOUSSEF, T.E.A. (1968)
"Experimental determination of the velocity and pressure profiles in the combustion zone in a model of a gas turbine combustion chamber"
S.A.E. Trans., 76, section 2, 1068.

FIGURES

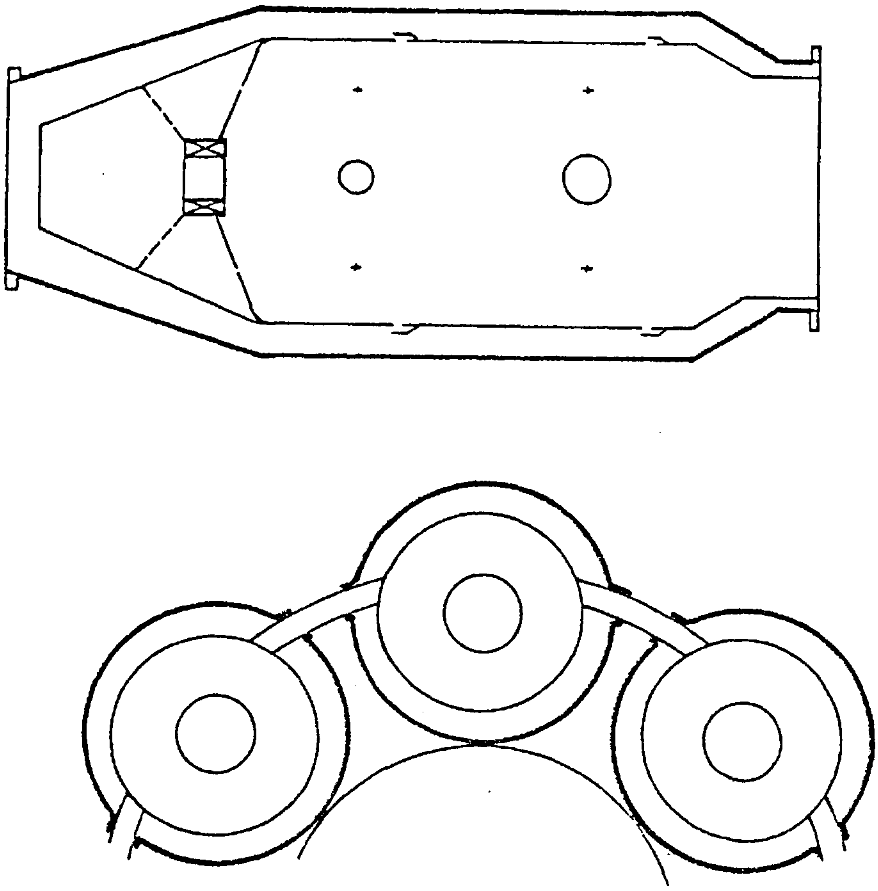

Figure 1.1 Tubular combustion chamber and arrangement

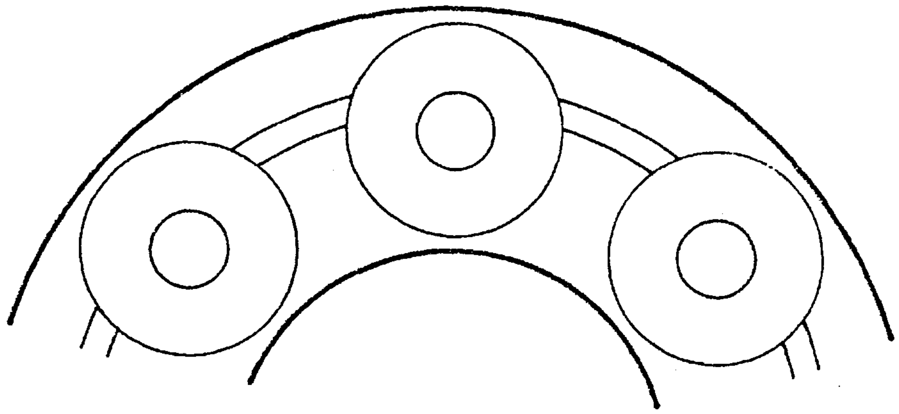

Figure 1.2 Tubo-annular arrangement

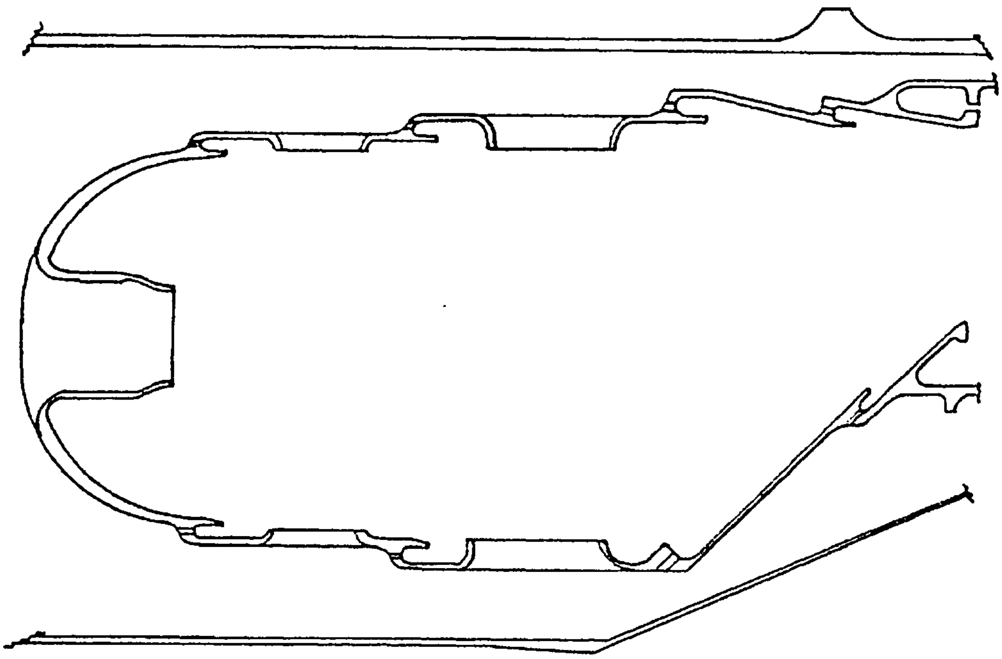

Figure 1.3 Annular combustion chamber

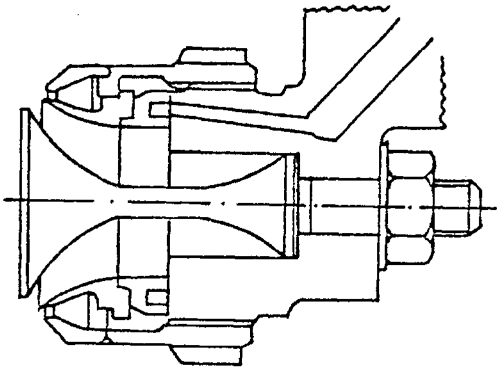

Figure 1.4 Swirl-atomiser fuel injector

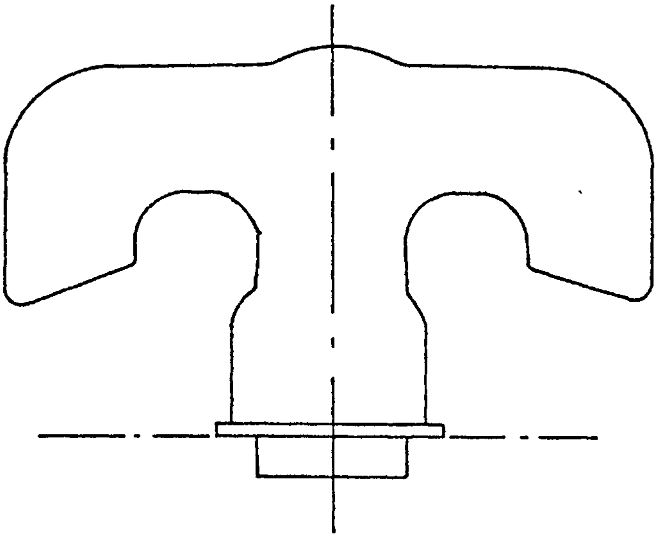

Figure 1.5 Vaporiser fuel injector

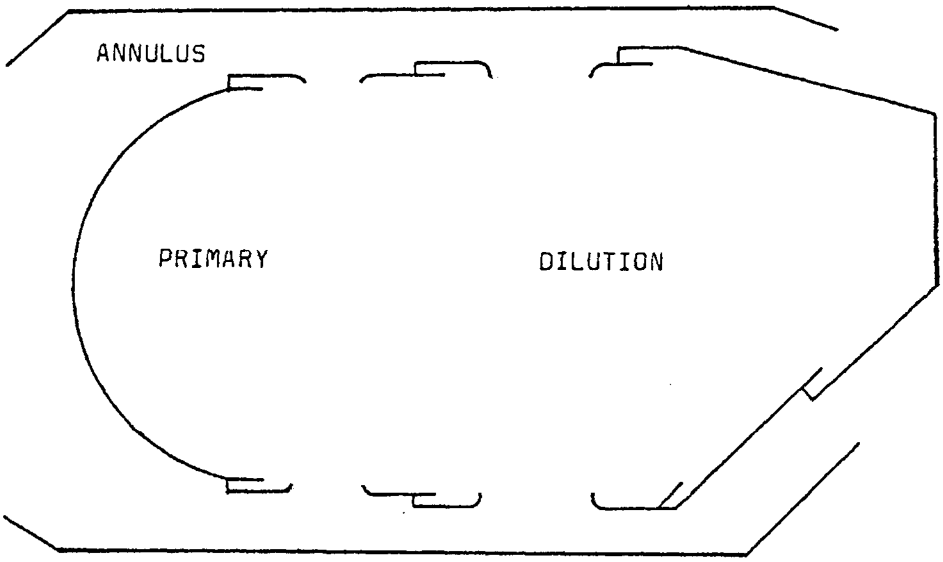

Figure 1.6 Combustion chamber zones

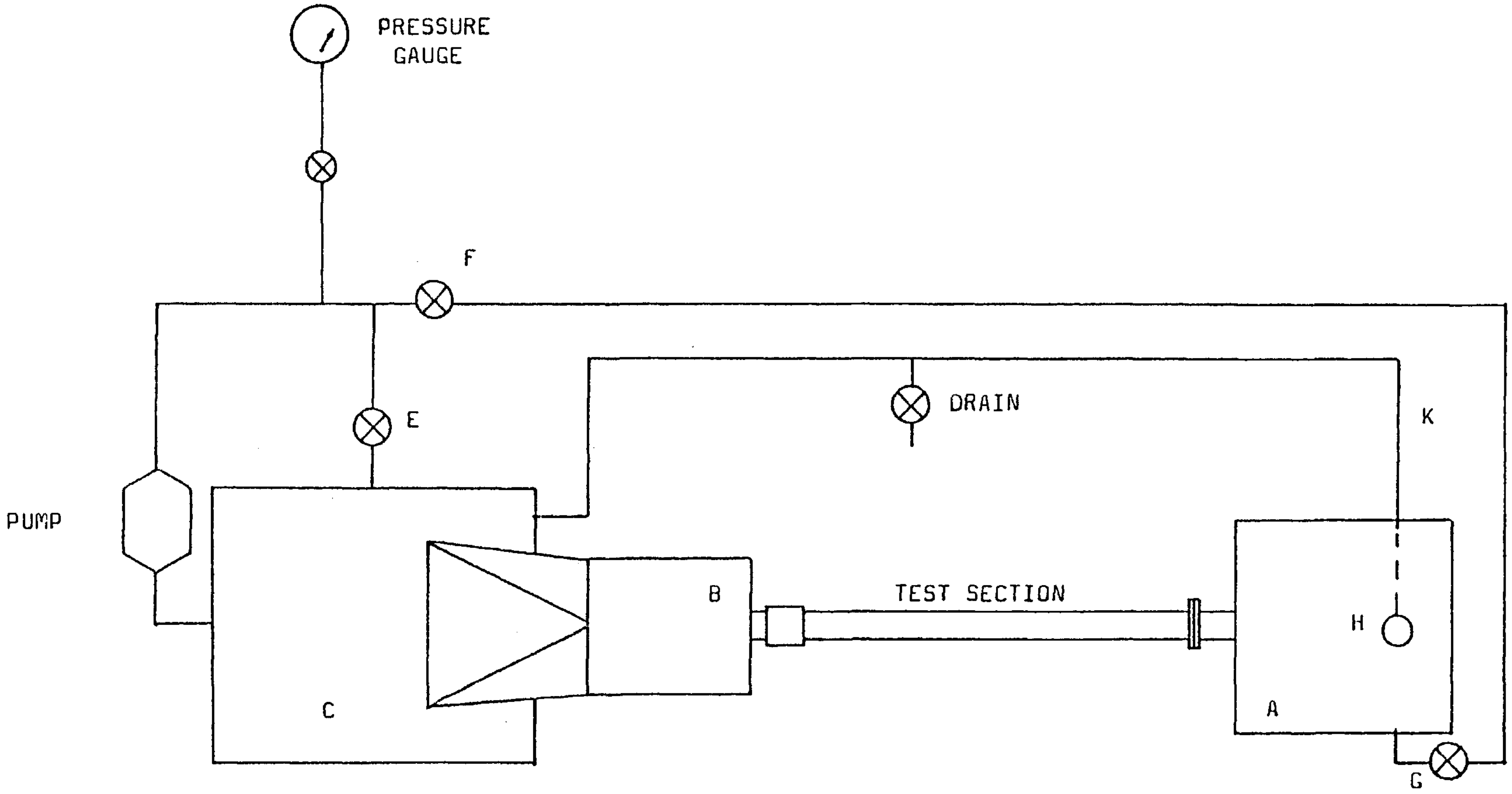

Figure 2.2.1 Plan view of water flow rig

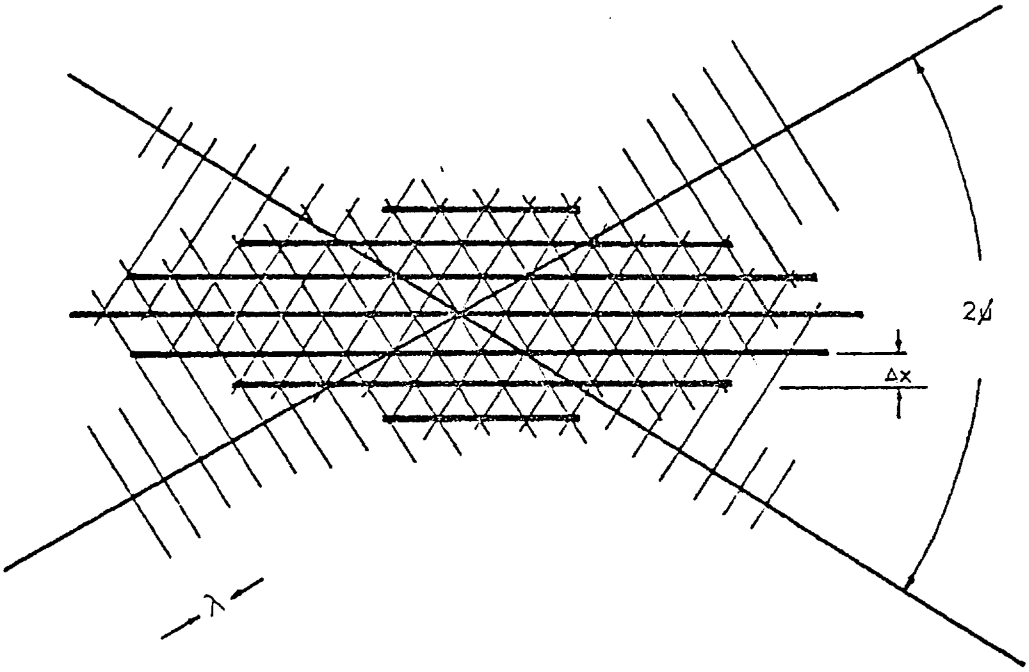

(a) Fringe model of scattering volume

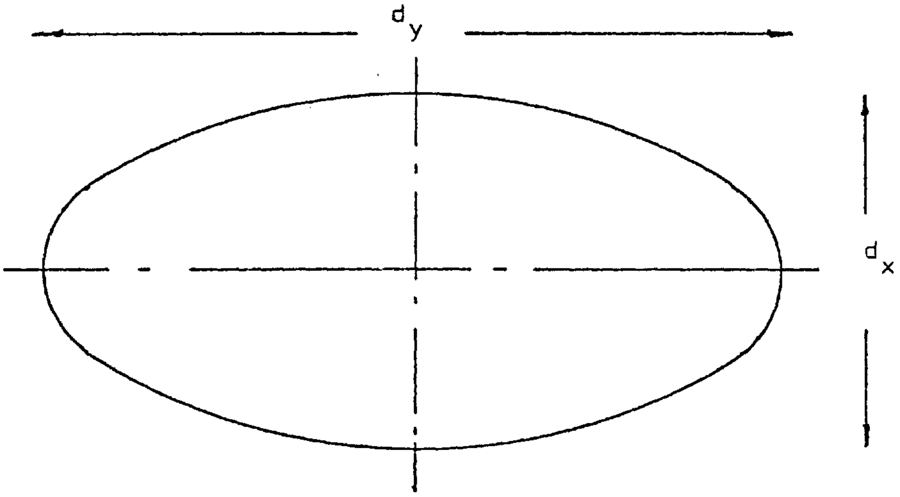

(b) Dimensions of scattering volume ellipsoid

Figure 2.3.1 The scattering volume

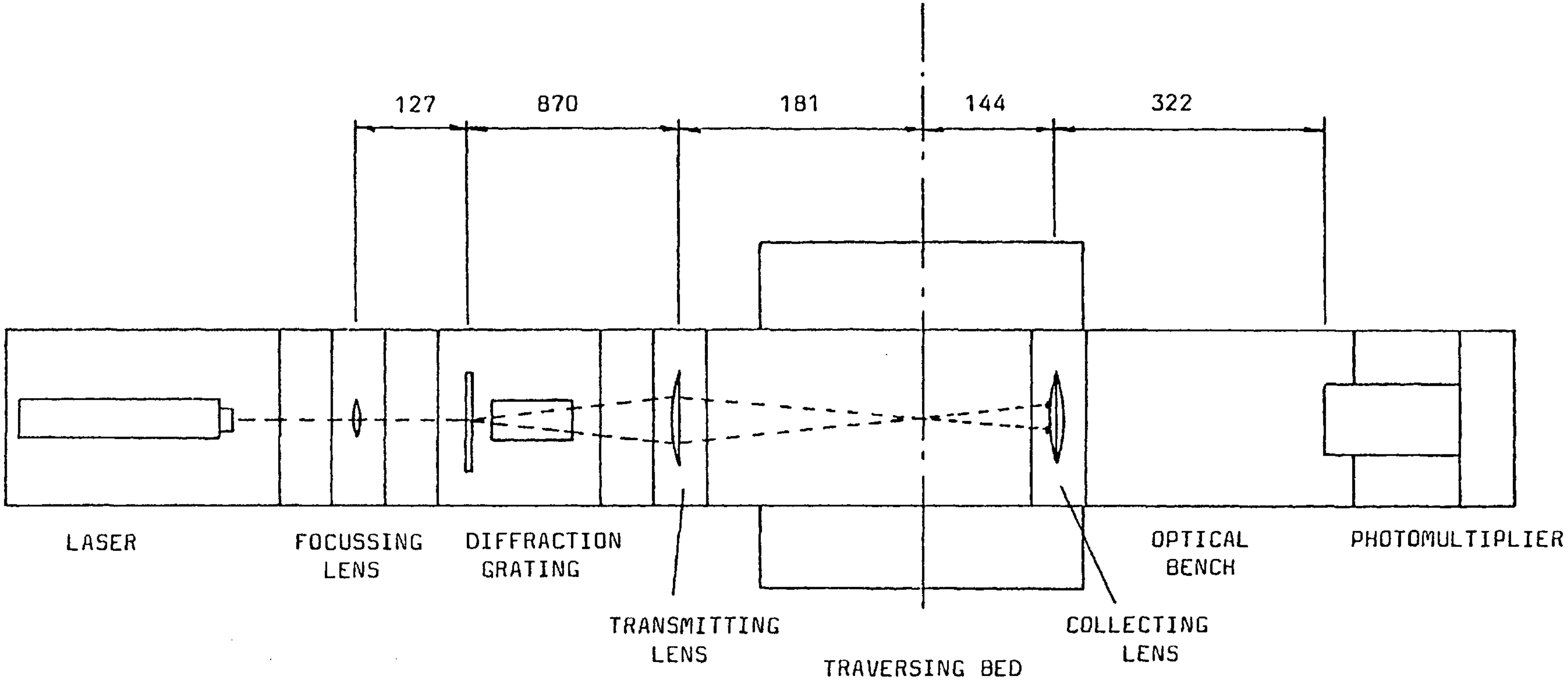

(dimensions in mm)

Figure 2.3.2 The measuring system

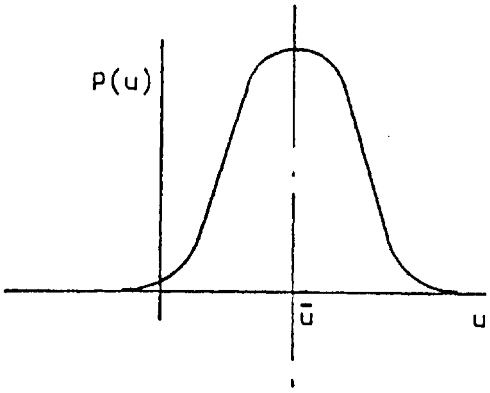

(a) Velocity probability distribution

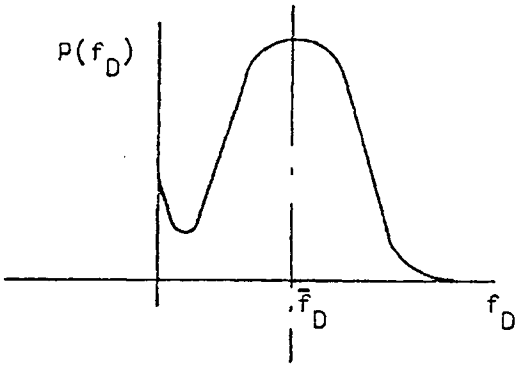

(b) Corresponding frequency probability distribution

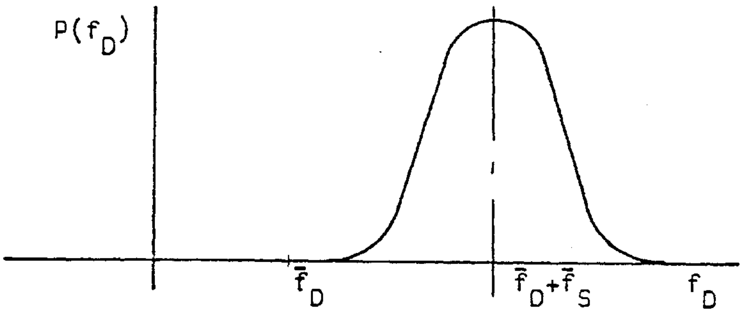

(c) Corresponding frequency probability distribution with frequency shift f_S

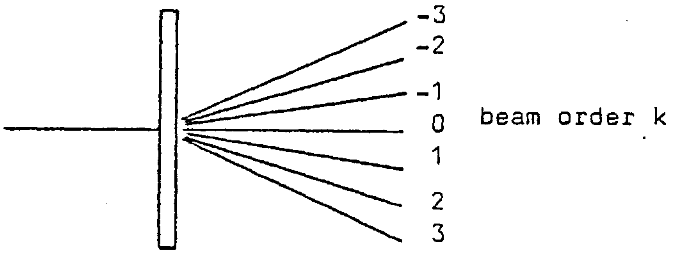

(d) Beam order of diffraction grating

Figure 2.3.3 Frequency shift effects and beam order

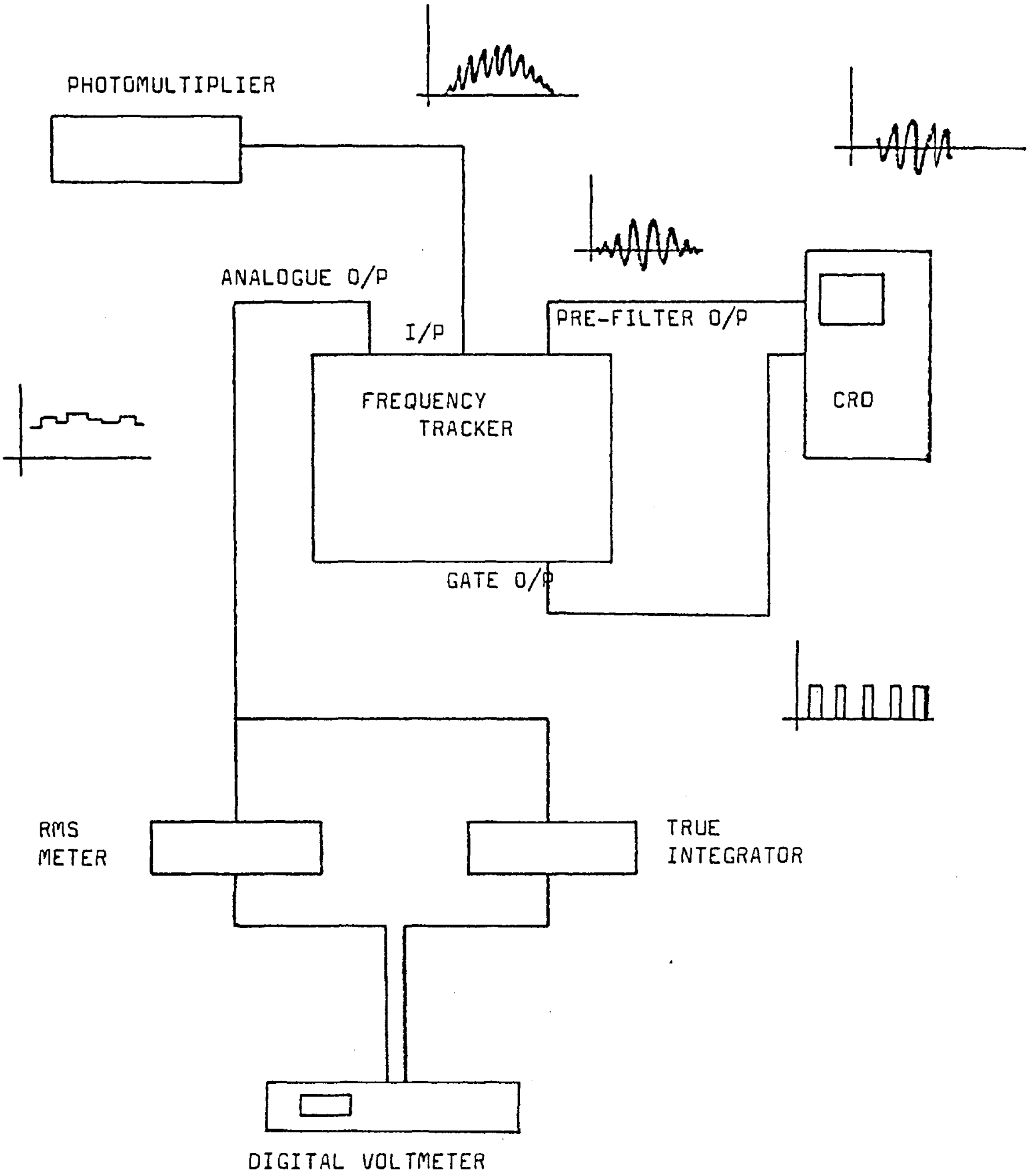

Figure 2.3.4 Schematic diagram of processing equipment and signal waveforms

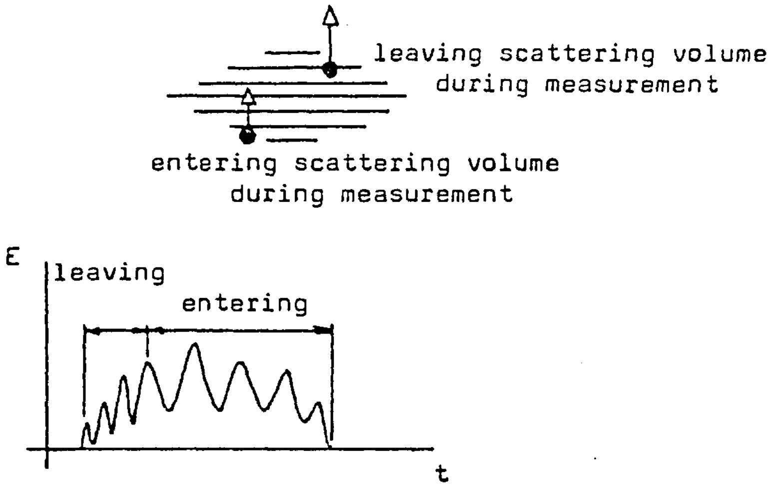

(a) Finite transit time broadening

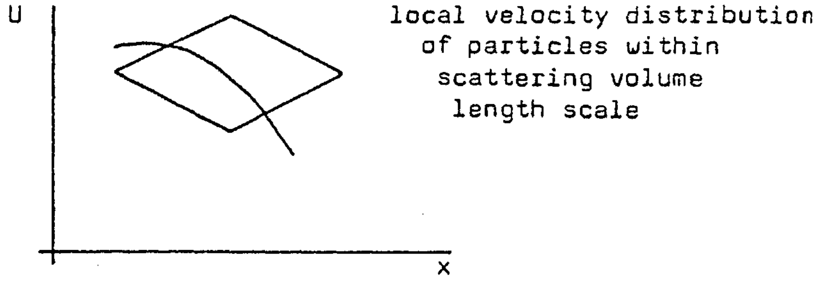

(b) Velocity gradient broadening

Figure 2.4.1 Common types of broadening

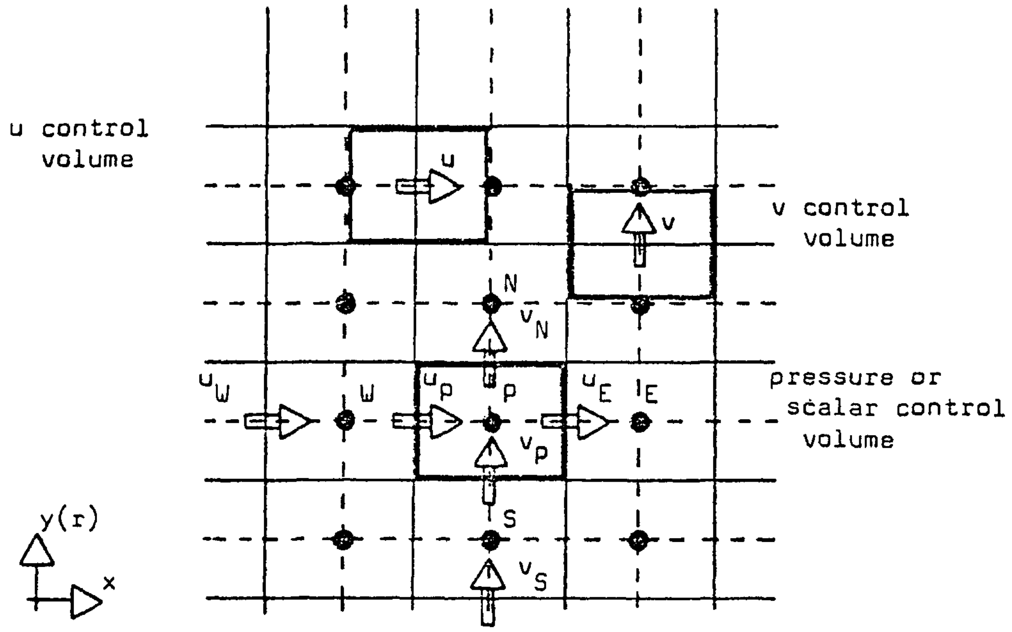

(a) u,v and scalar control volumes in x-y plane

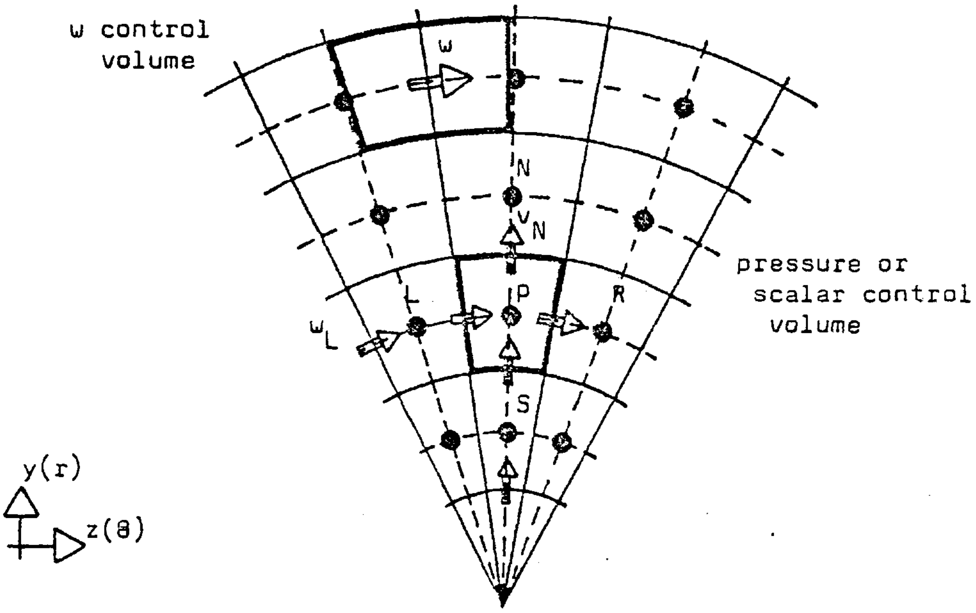

(b) w and scalar control volumes in y-z plane

Figure 3.1 Velocity and scalar control volumes for a three-dimensional calculation domain

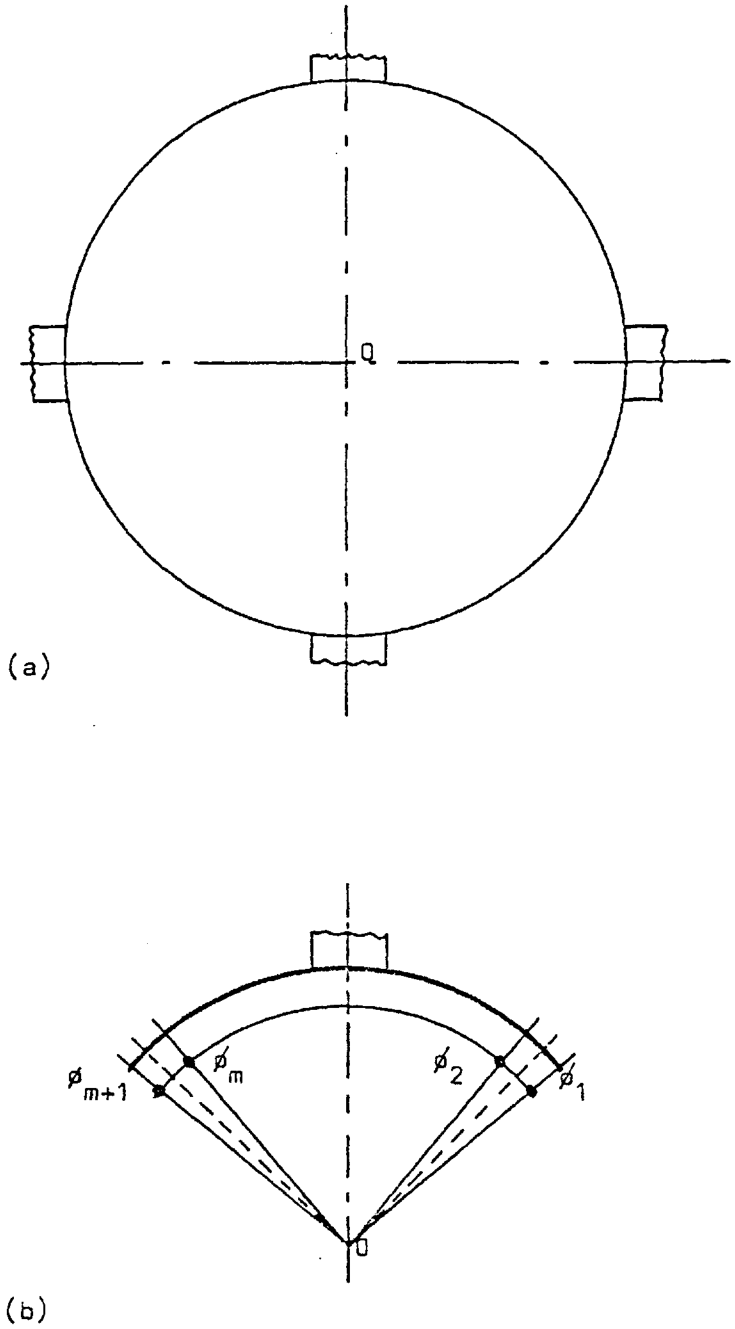

Figure 3.2 Cyclic boundary conditions

(a) Physical domain with periodic uniformity about 0

(b) Calculation domain with cyclic boundary conditions applied at periodic axes

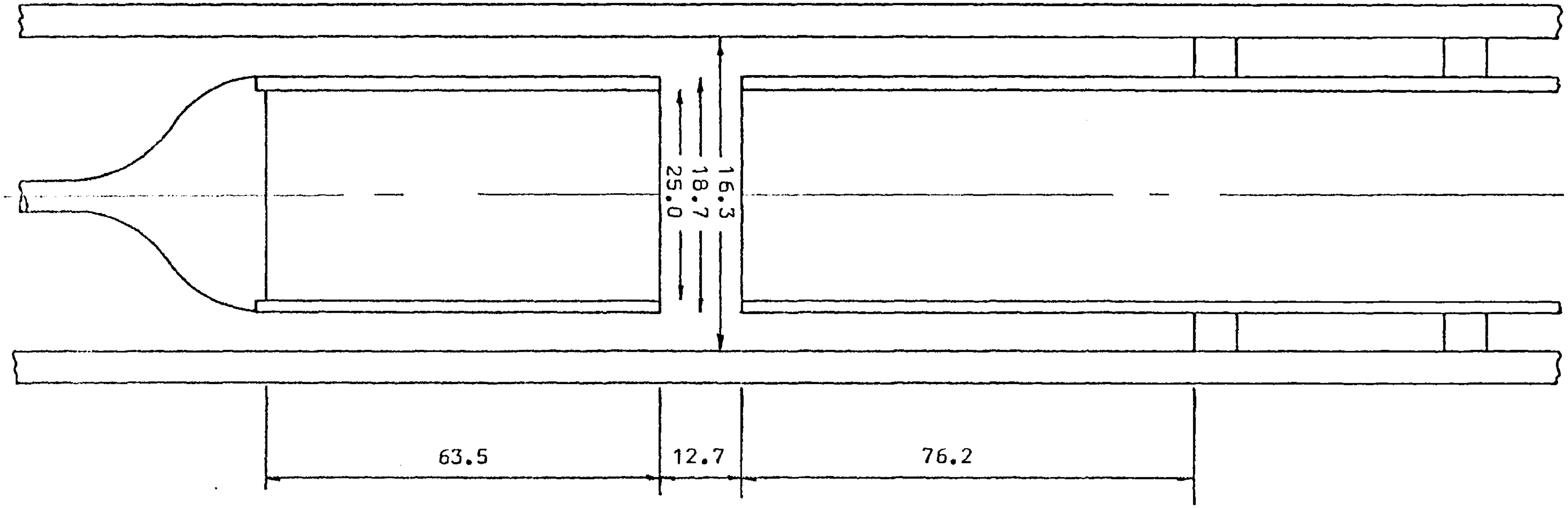

(dimensions in mm)

Figure 4.2.1 The two-dimensional axisymmetric model

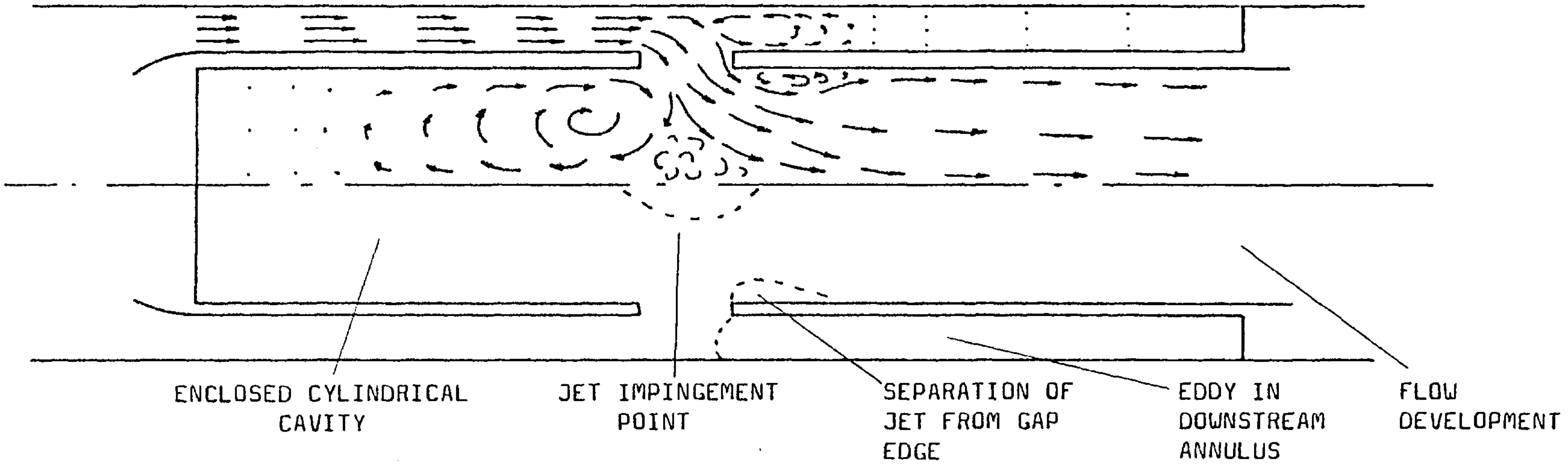

Figure 4.2.2 Flow pattern from flow visualisation

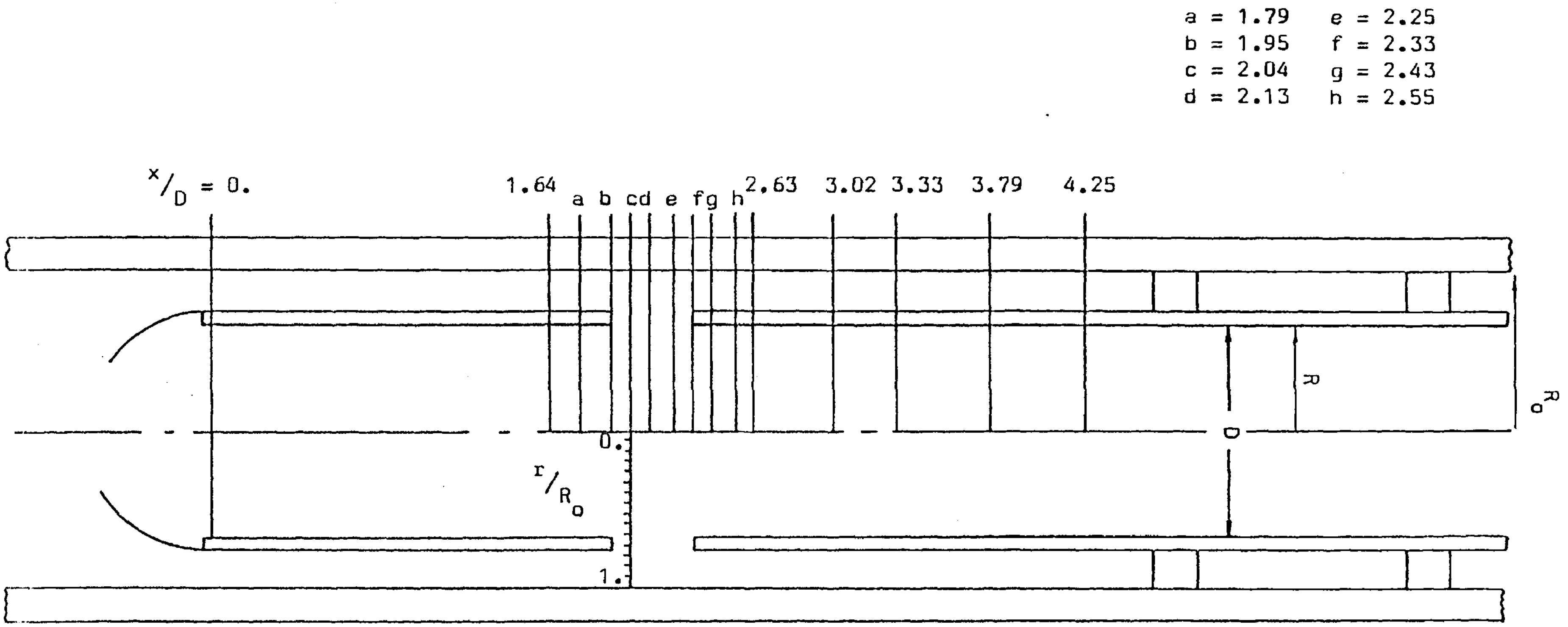

Figure 4.3.1 The measuring locations

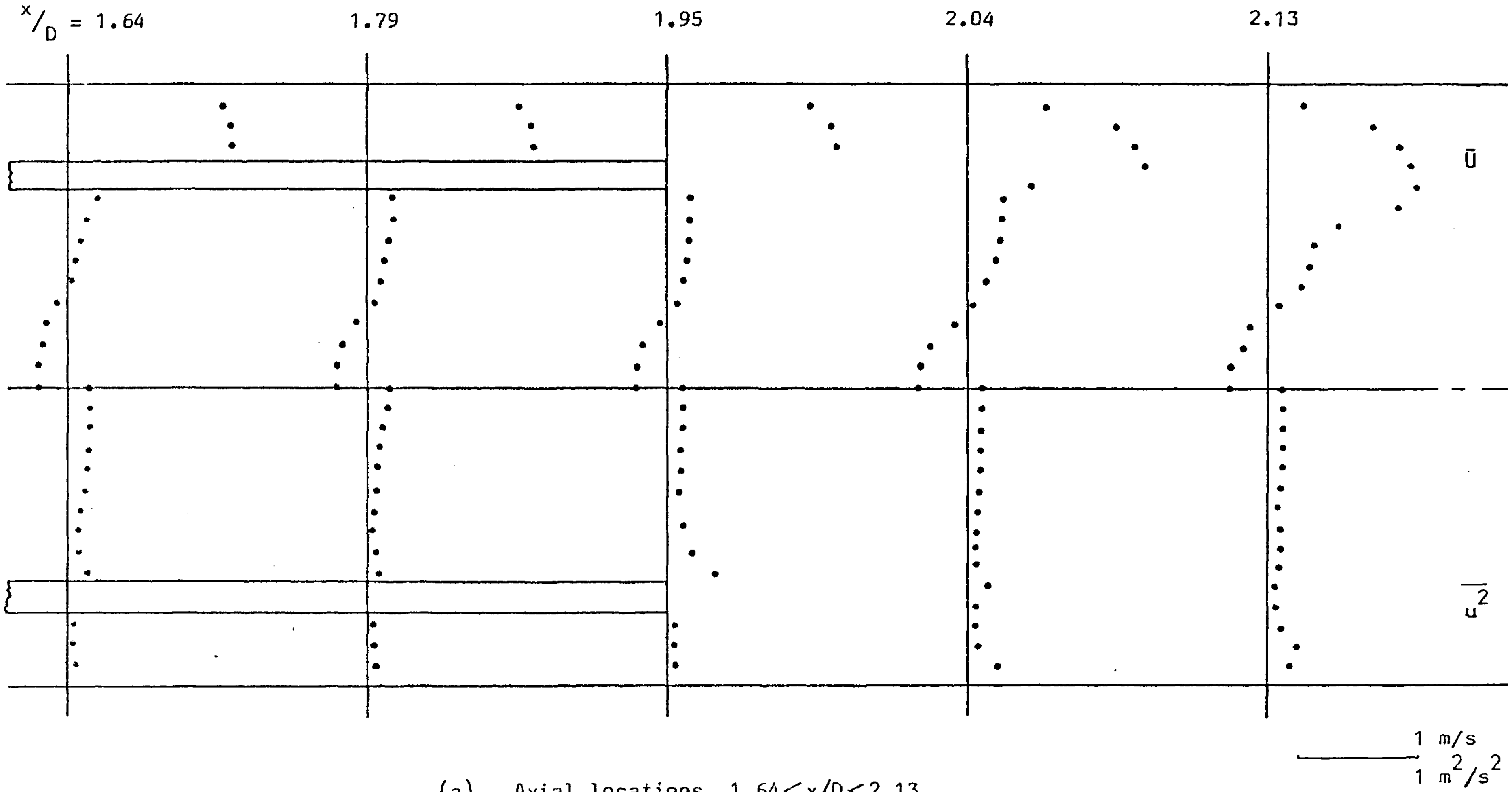

(a) Axial locations 1.64 ⩽ x/D ⩽ 2.13

Figure 4.3.2 Radial profiles of mean axial velocity and normal stress

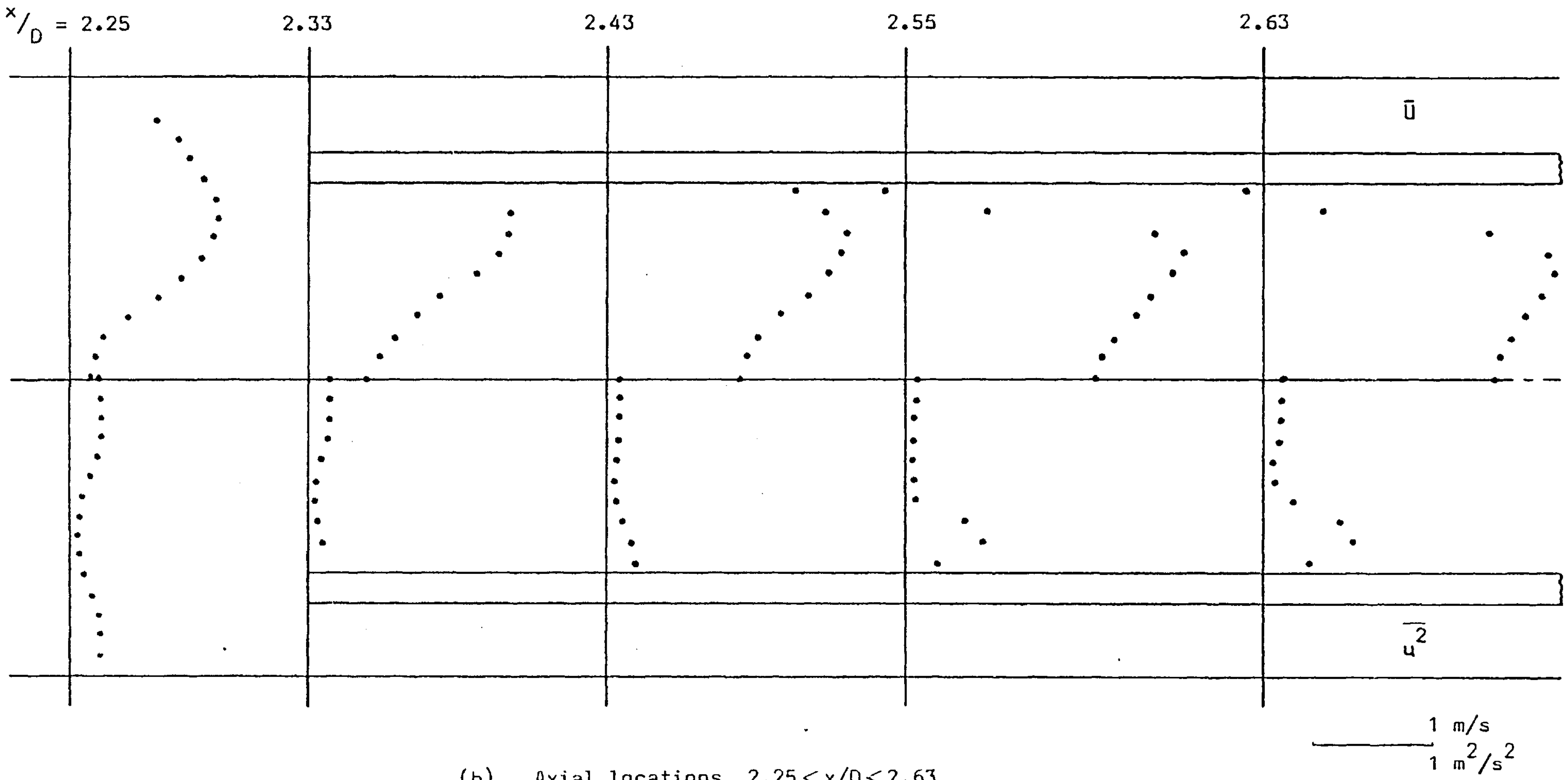

(b) Axial locations $2.25 \leqslant x/D \leqslant 2.63$

Figure 4.3.2 Radial profiles of mean axial velocity and normal stress

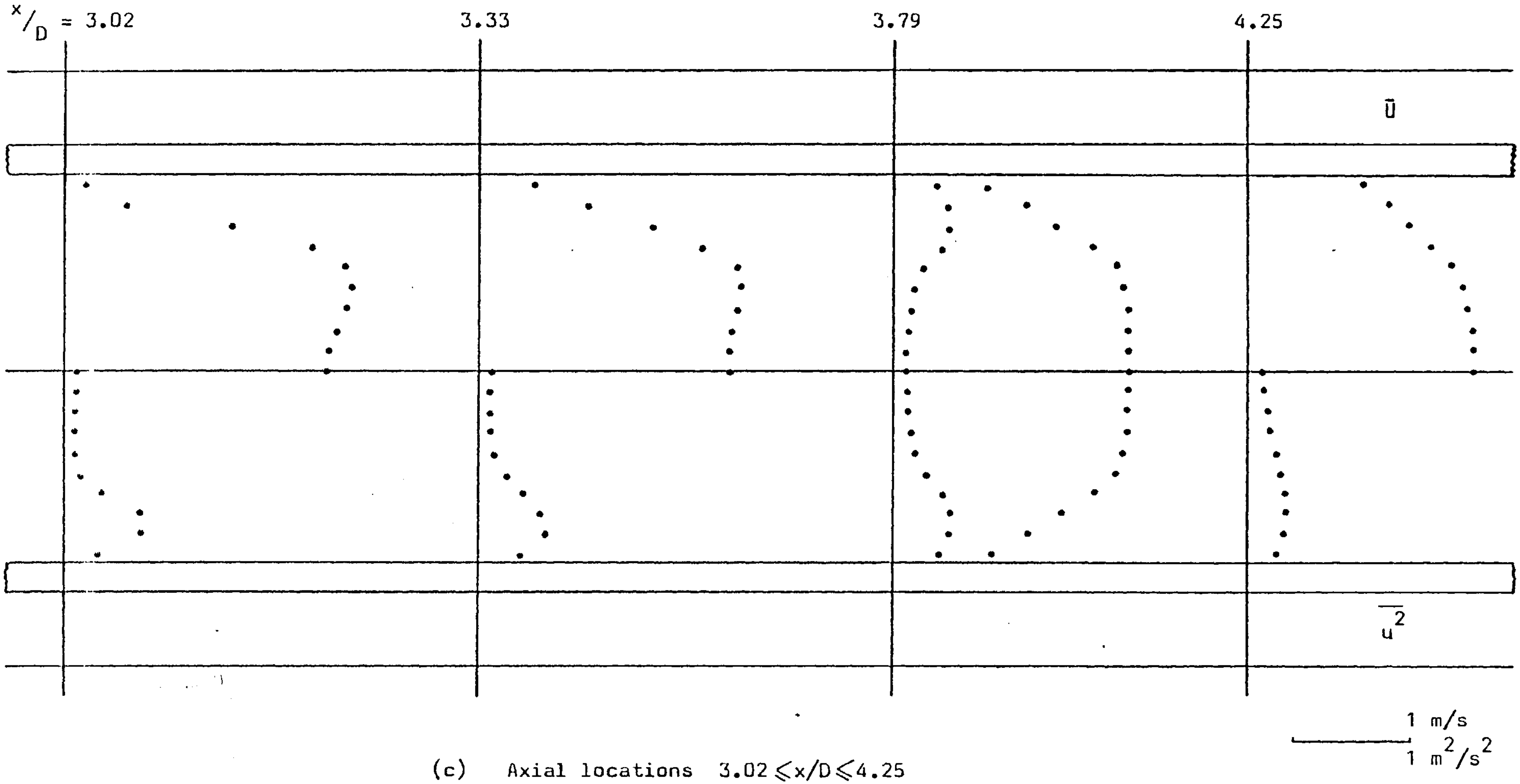

(c) Axial locations $3.02 \leqslant x/D \leqslant 4.25$

Figure 4.3.2 Radial profiles of mean axial velocity and normal stress

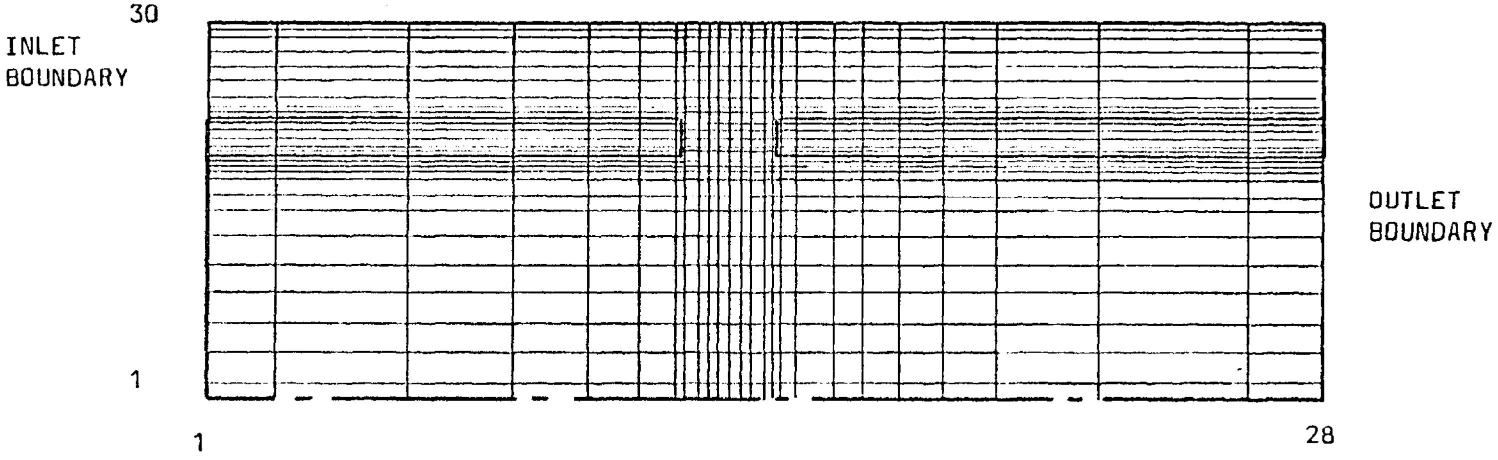

Figure 4.4.1 The finite-difference grid (28 x 30 nodes)

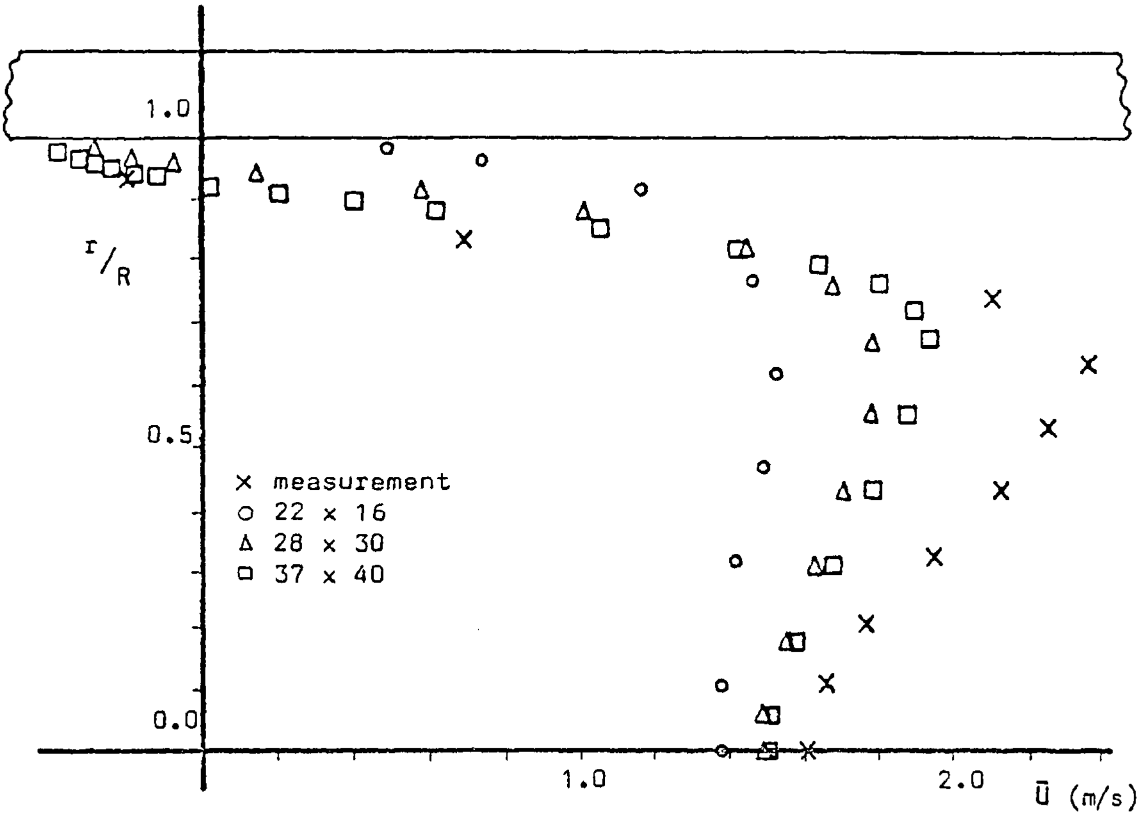

Figure 4.4.2 Dependence of mean axial velocity on grid node density at x/D = 2.55

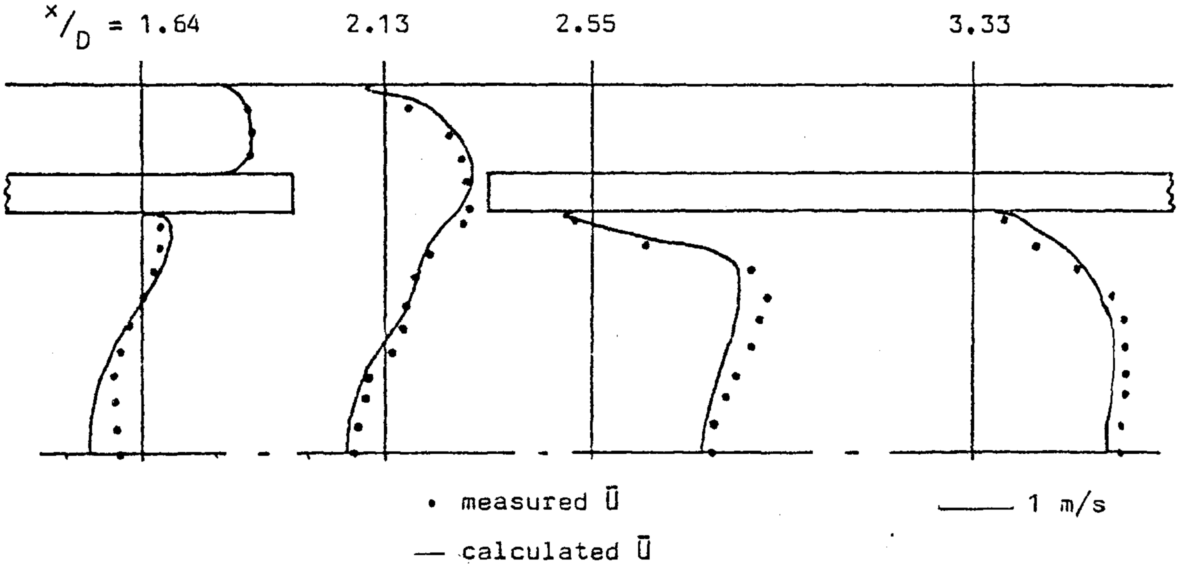

Figure 4.5.1 Comparison of calculated and measured mean axial velocity profiles at four locations

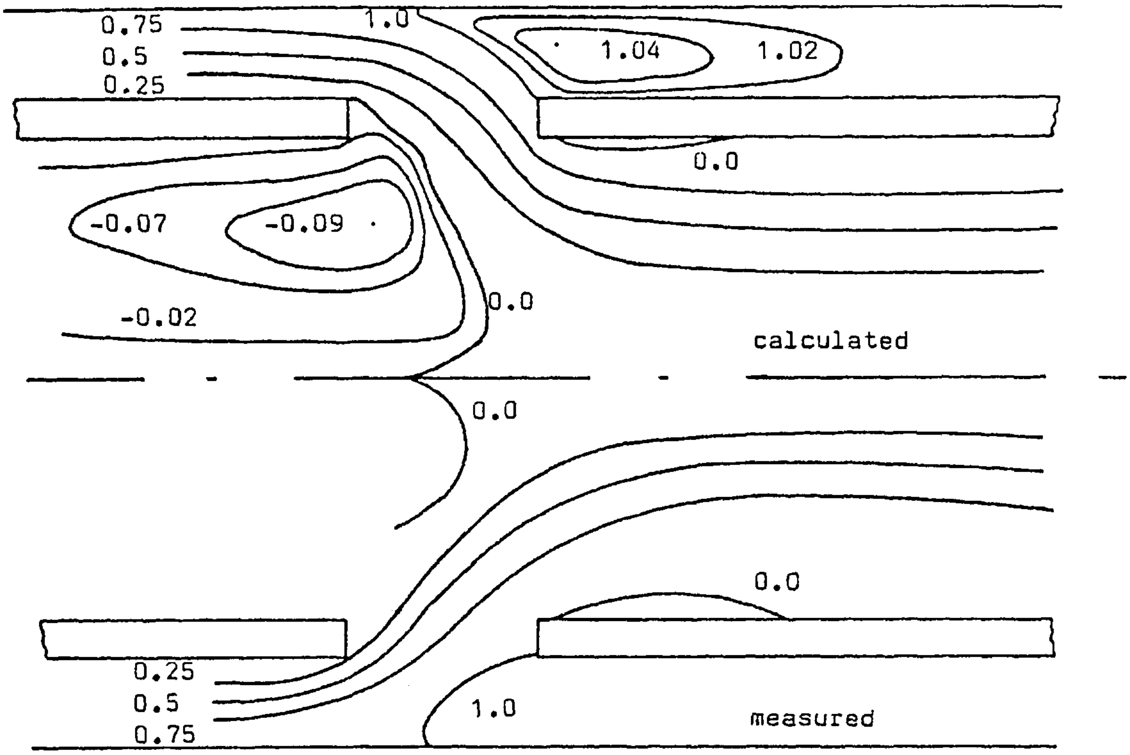

Figure 4.5.2 Comparison of calculated and measured streamline contours (determined from mean axial velocity)

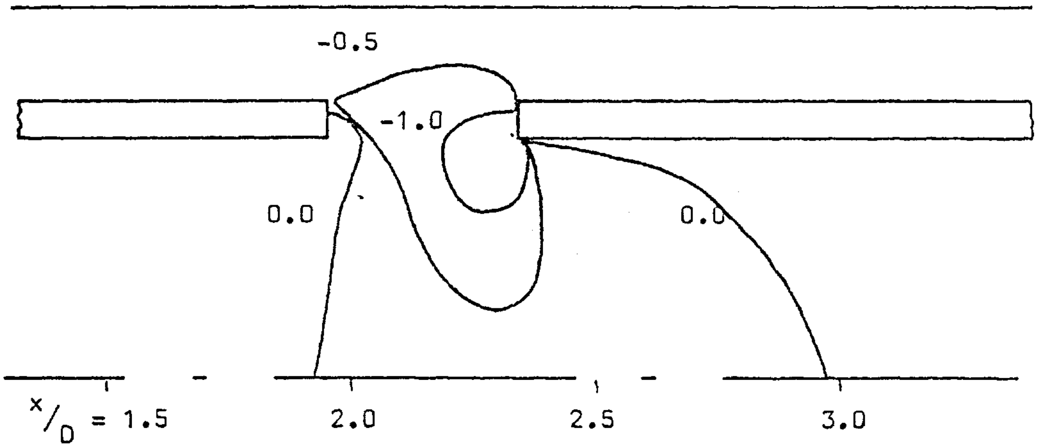

Figure 4.6.1 Contours of calculated radial velocity ($\bar{V}$)

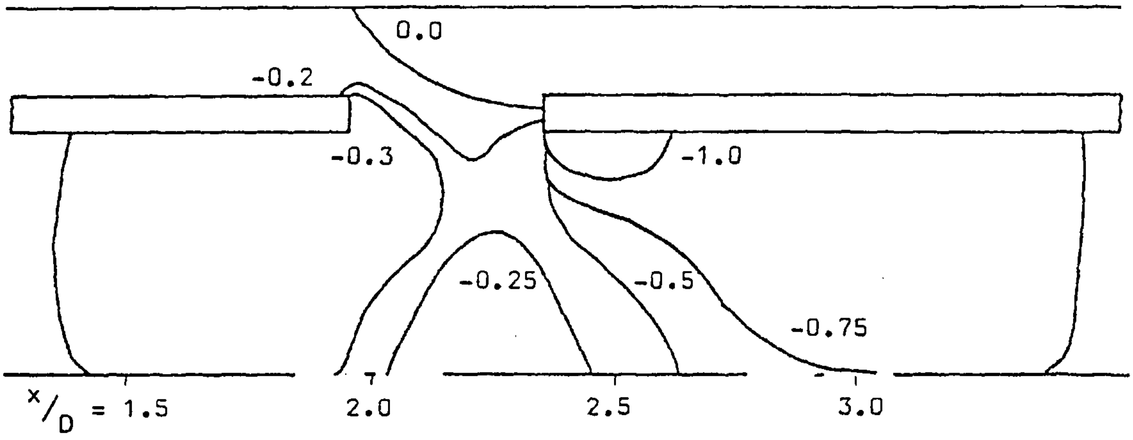

(a) The local normalised pressure contours (p_c) in the gap region

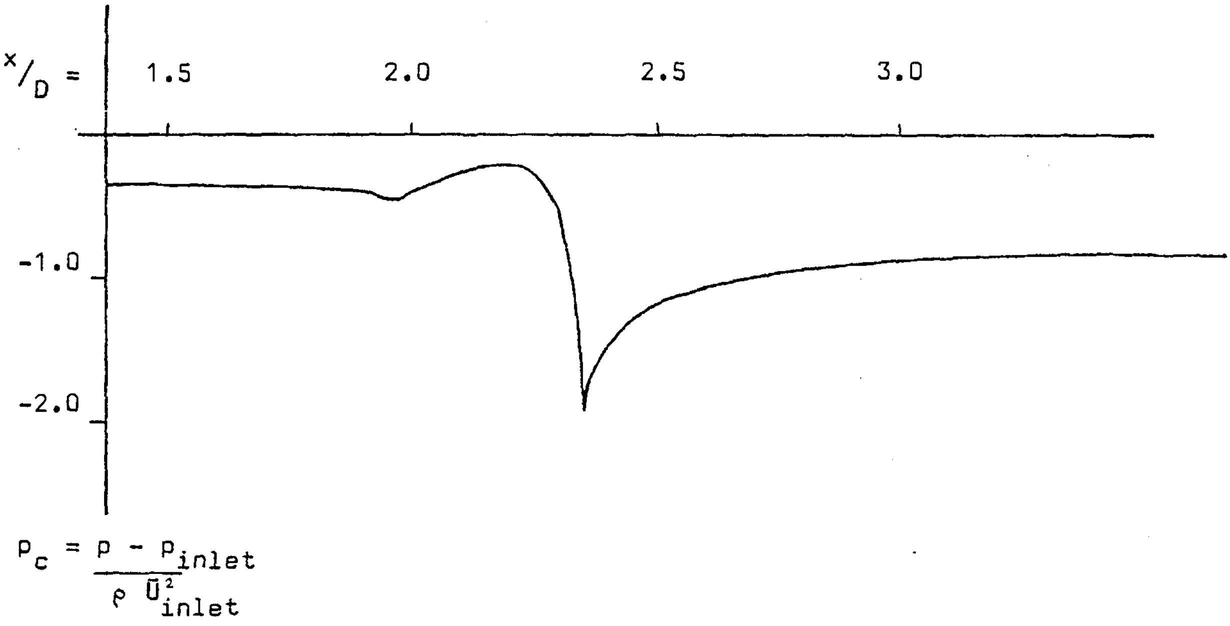

$$p_c = \frac{p - p_{inlet}}{\rho \, \bar{U}^2_{inlet}}$$

(b) A cross-section of the pressure contours at r/R = 0.99

Figure 4.6.2 The pressure distribution

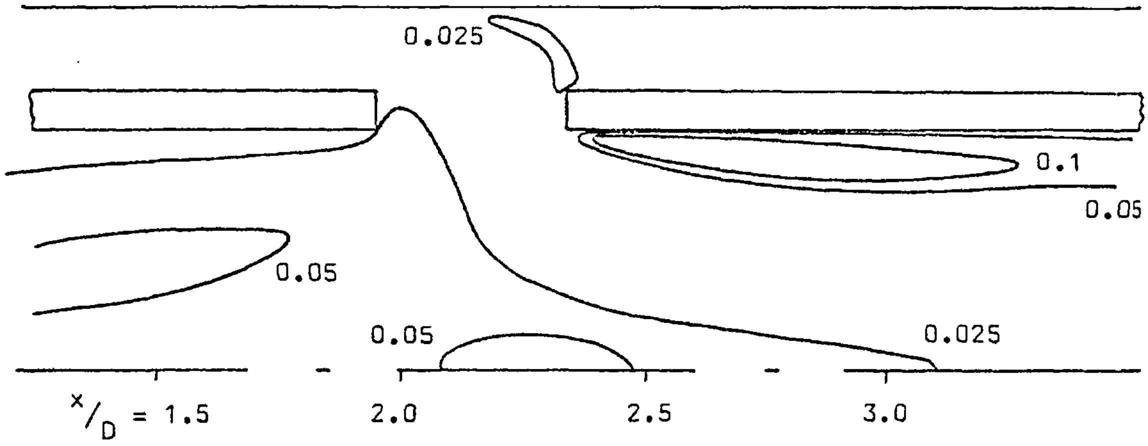

Figure 4.6.3 Contours of calculated turbulence kinetic energy

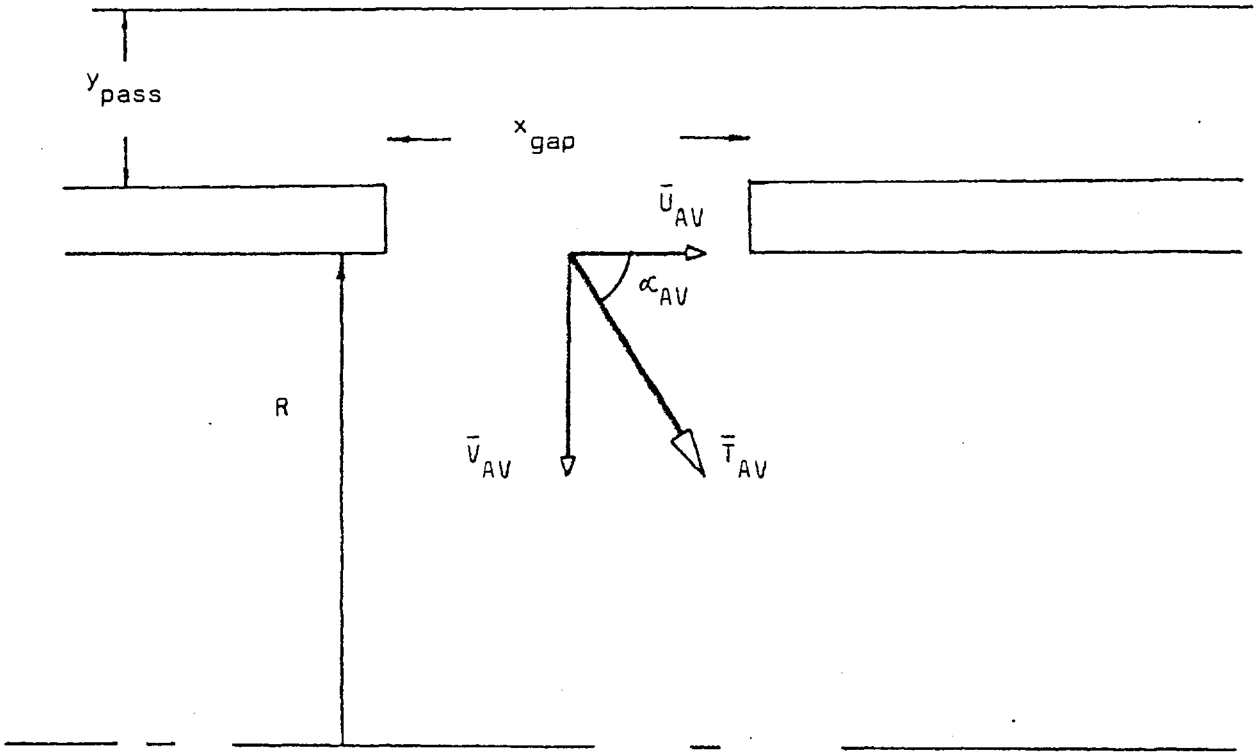

Figure 4.7.1 Location of trajectory angle and magnitude of jet resultant velocity

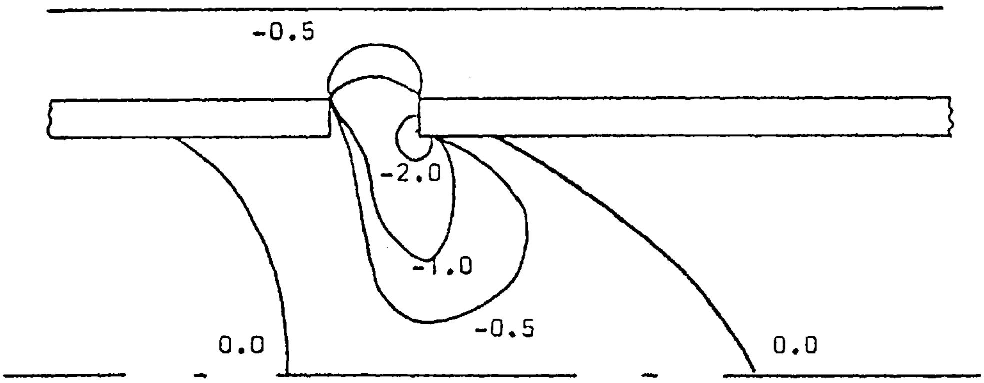

(a) Reduced gap width by 50%

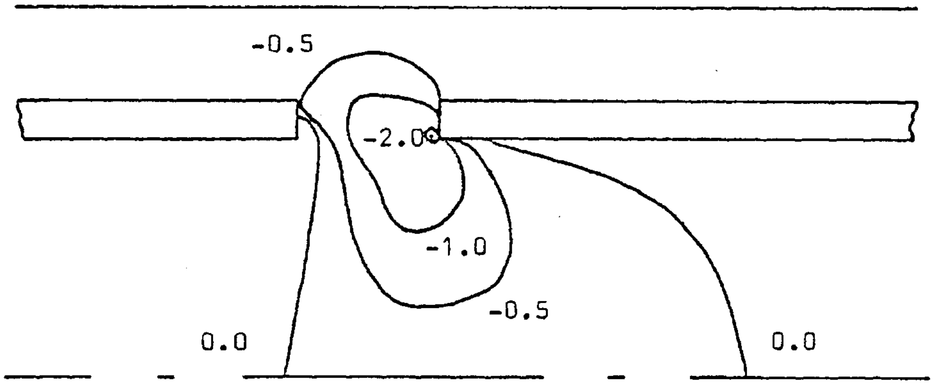

(b) Reduced gap width by 25%

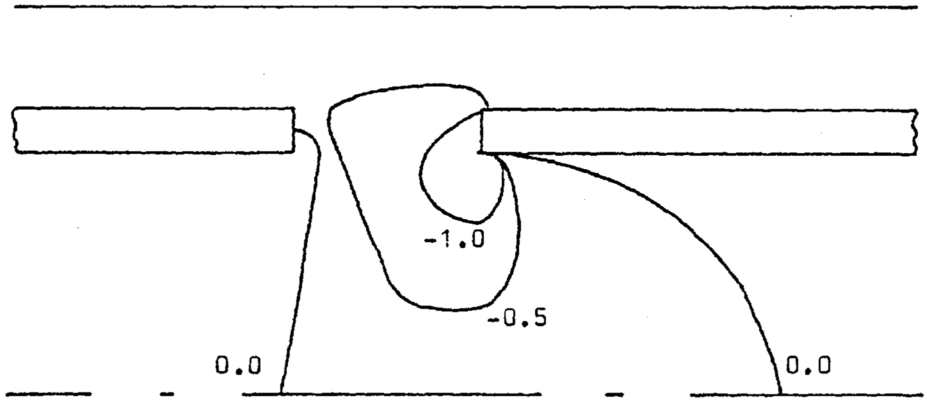

(c) Increased annulus by 25%

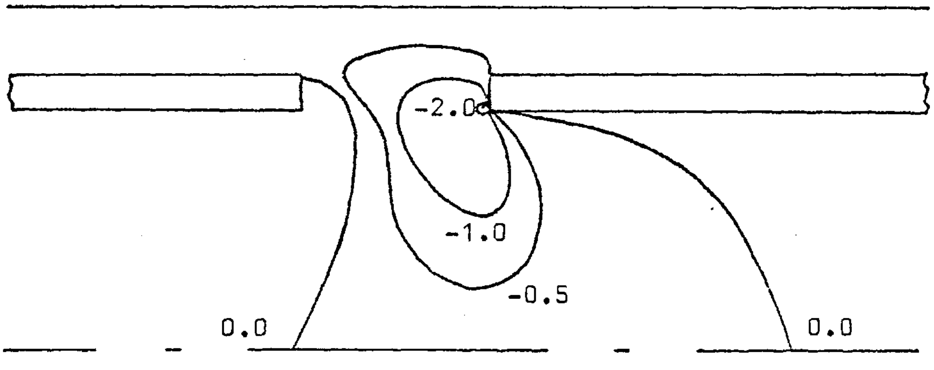

(d) Reduced annulus by 25%

Figure 4.7.2 Calculated radial velocity contours for variations in local geometry

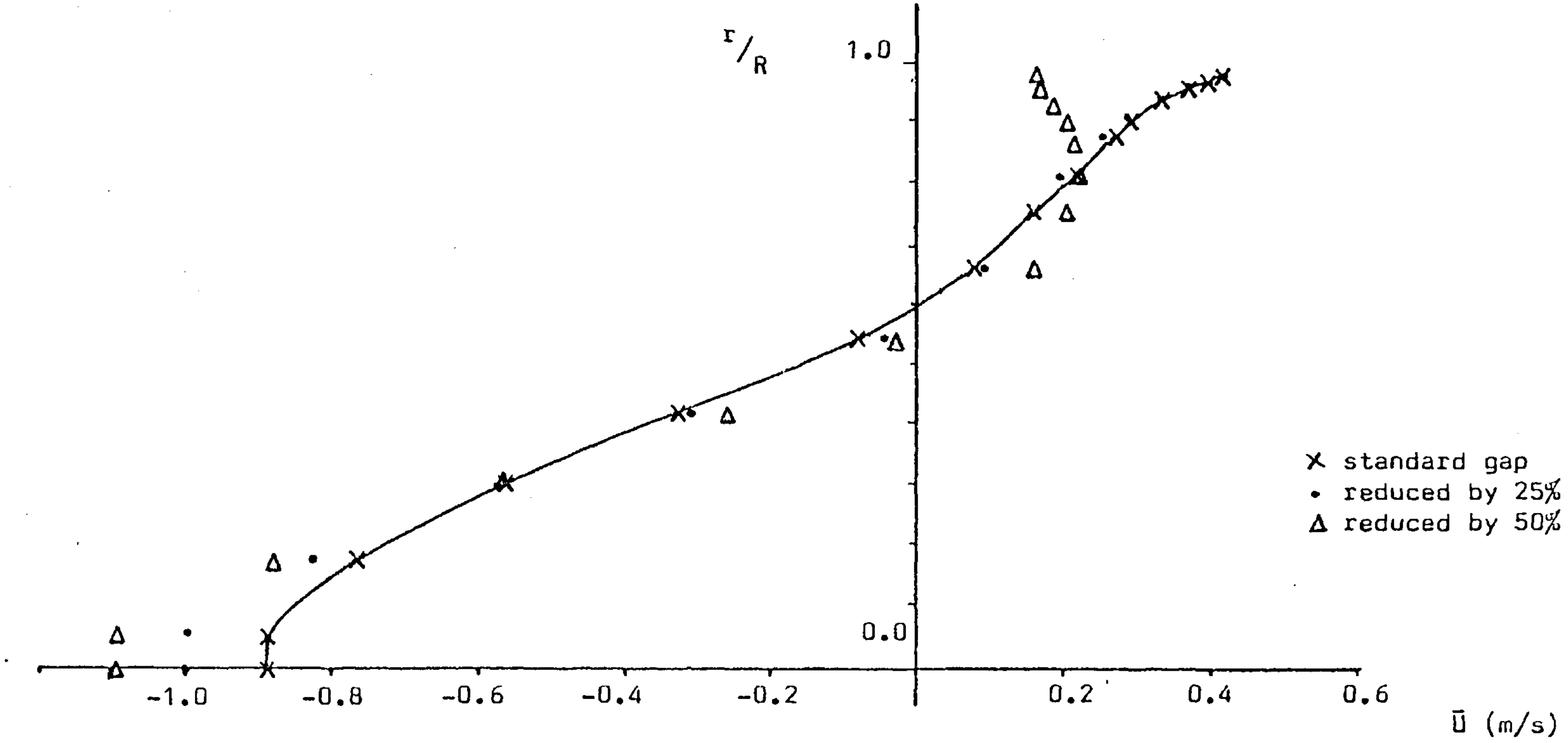

(a) Axial velocity profiles at x/D = 1.95 for variation in gap width

Figure 4.7.3 Calculated axial velocity profiles for variations in local geometry (i)

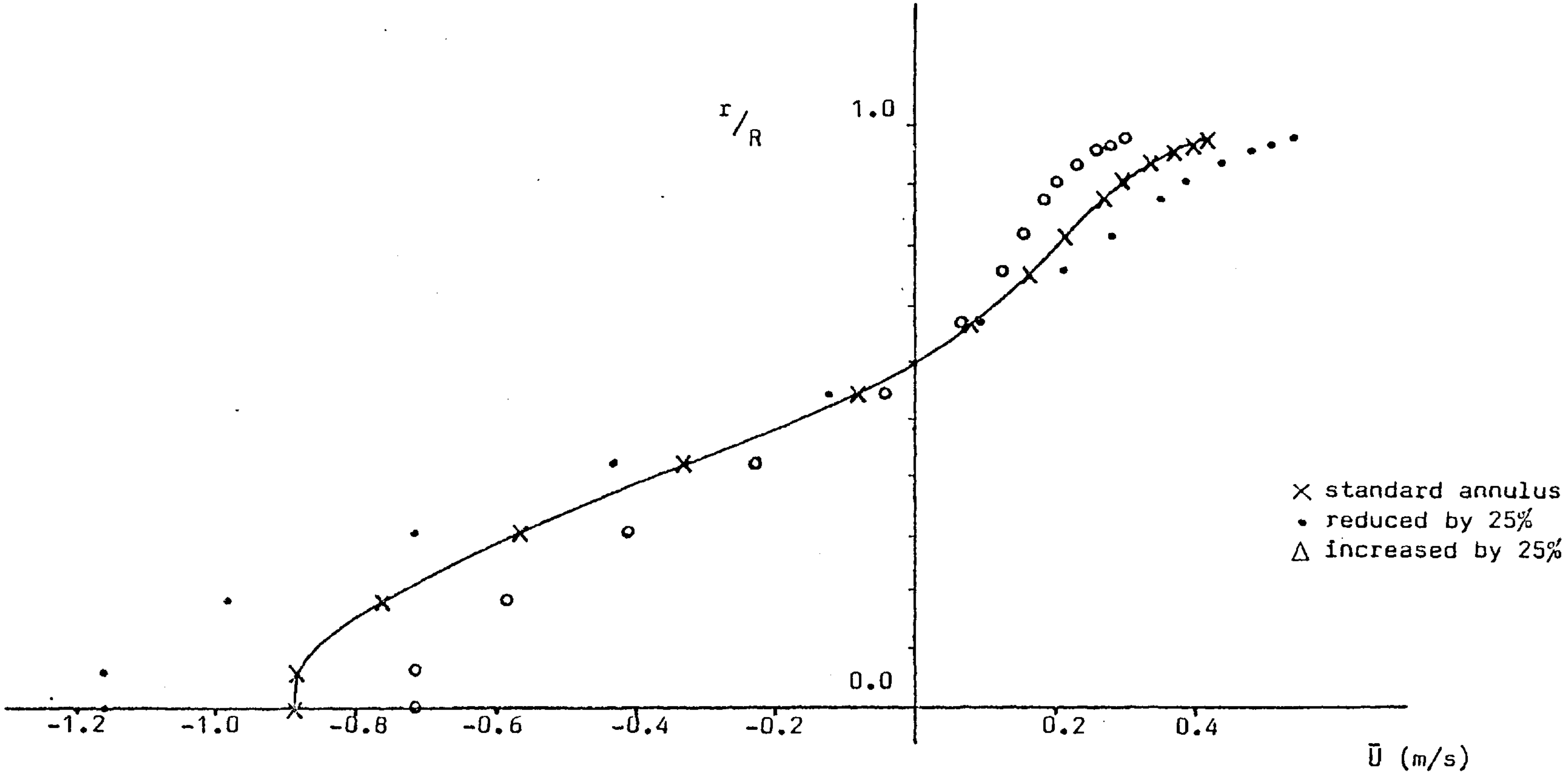

(b) Axial velocity profiles at x/D = 1.95 for variation in annulus width

Figure 4.7.3 Calculated axial velocity profiles for variations in local geometry (i)

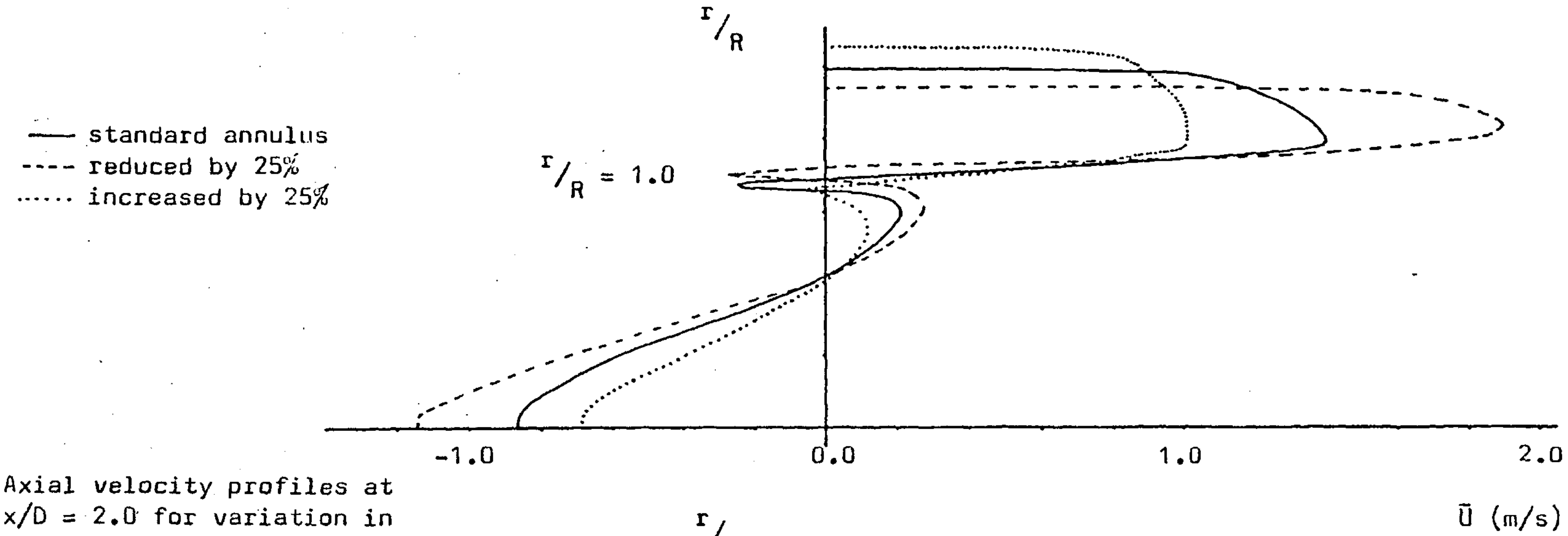

(a) Axial velocity profiles at x/D = 2.0 for variation in annulus width

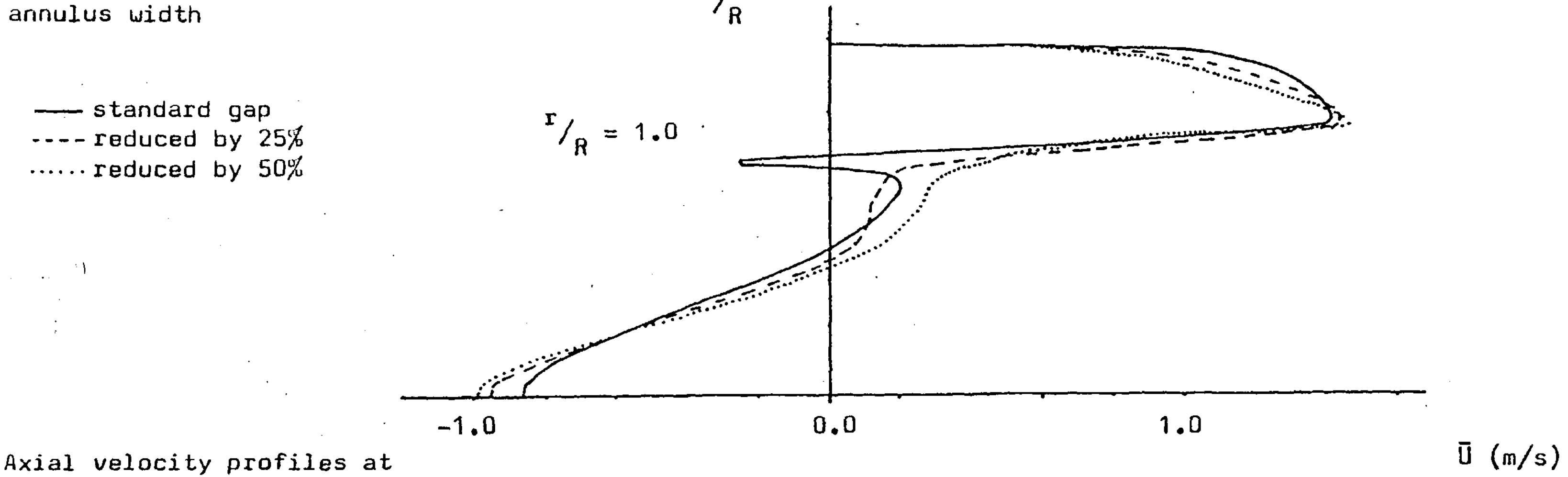

(b) Axial velocity profiles at x/D = 2.0 for variation in gap width

Figure 4.7.4 Calculated axial velocity profiles for variations in local geometry (ii)

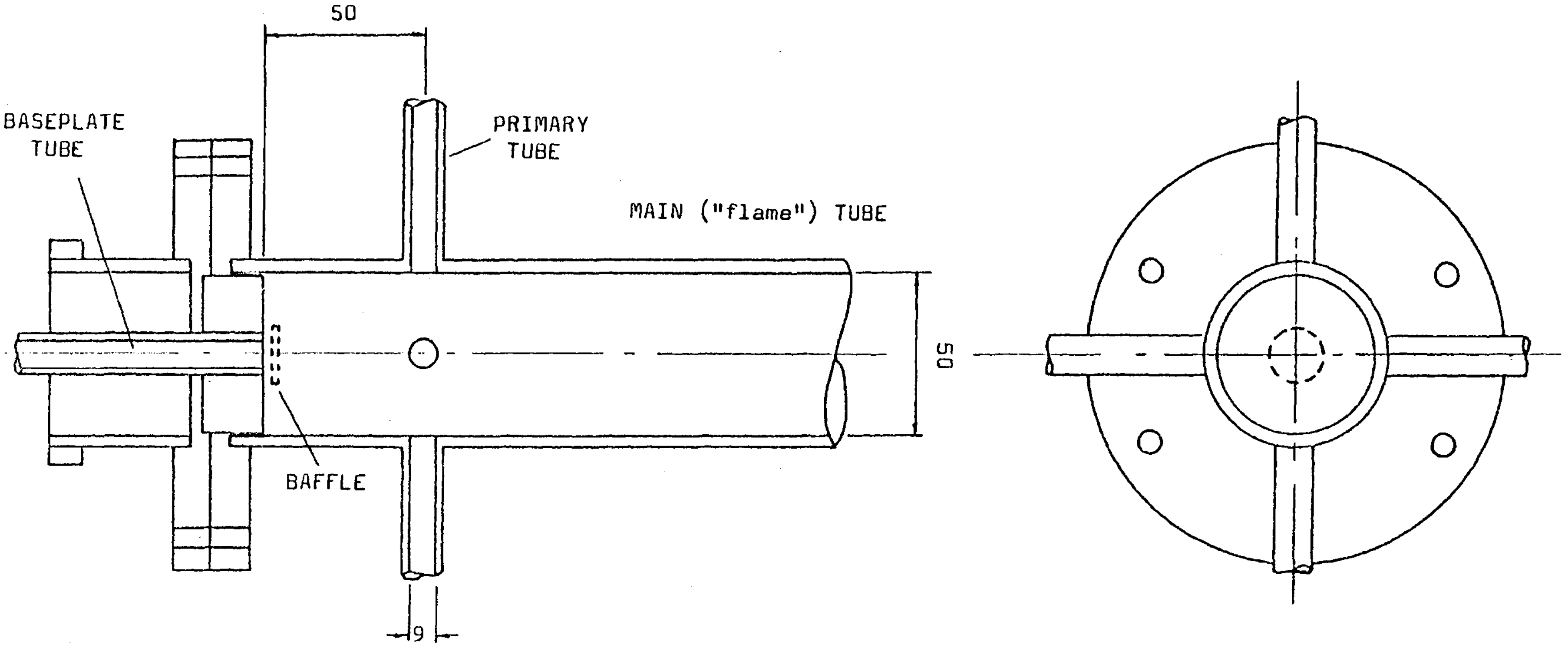

Figure 5.2.1 The three-dimensional model without an annulus

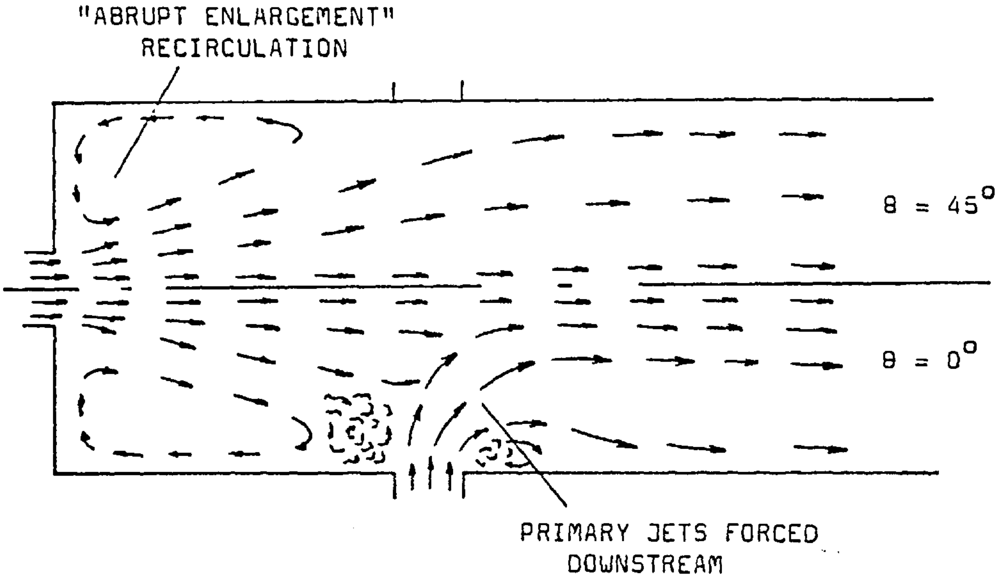

Figure 5.2.2 (a) Flow pattern for geometry without a baffle (Case 1)

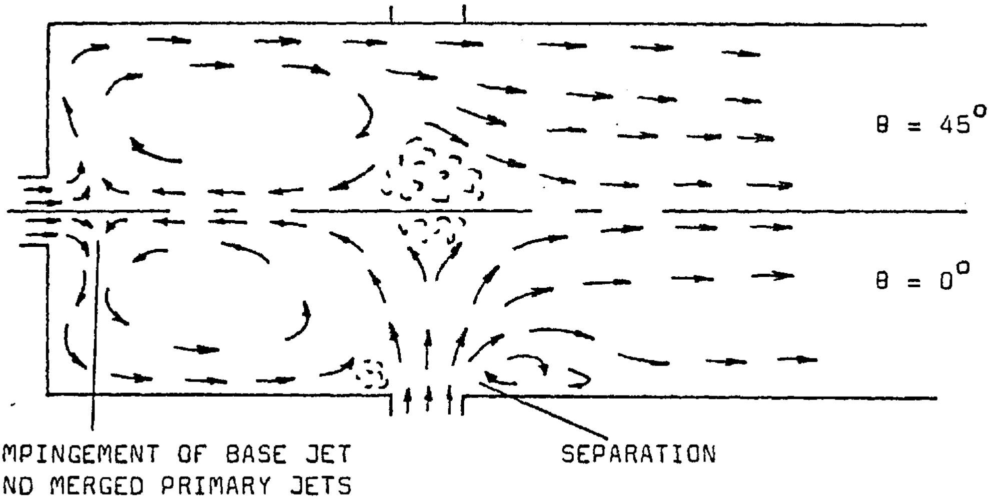

Figure 5.2.2 (b) Flow pattern for geometry without a baffle (Case 2)

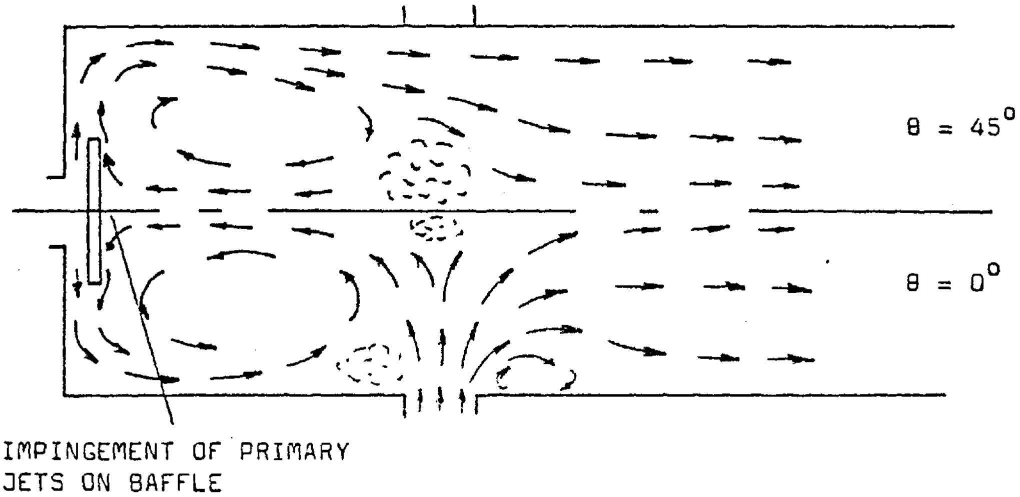

Figure 5.2.2 (c) Flow pattern for geometry with a baffle (Cases 3,4 and 5)

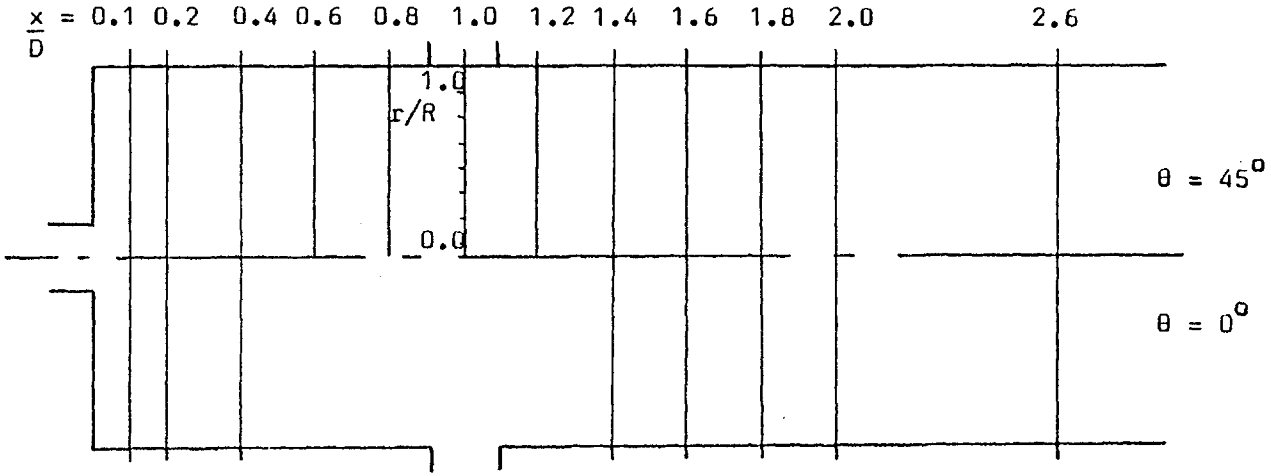

Figure 5.3.1 The measuring locations

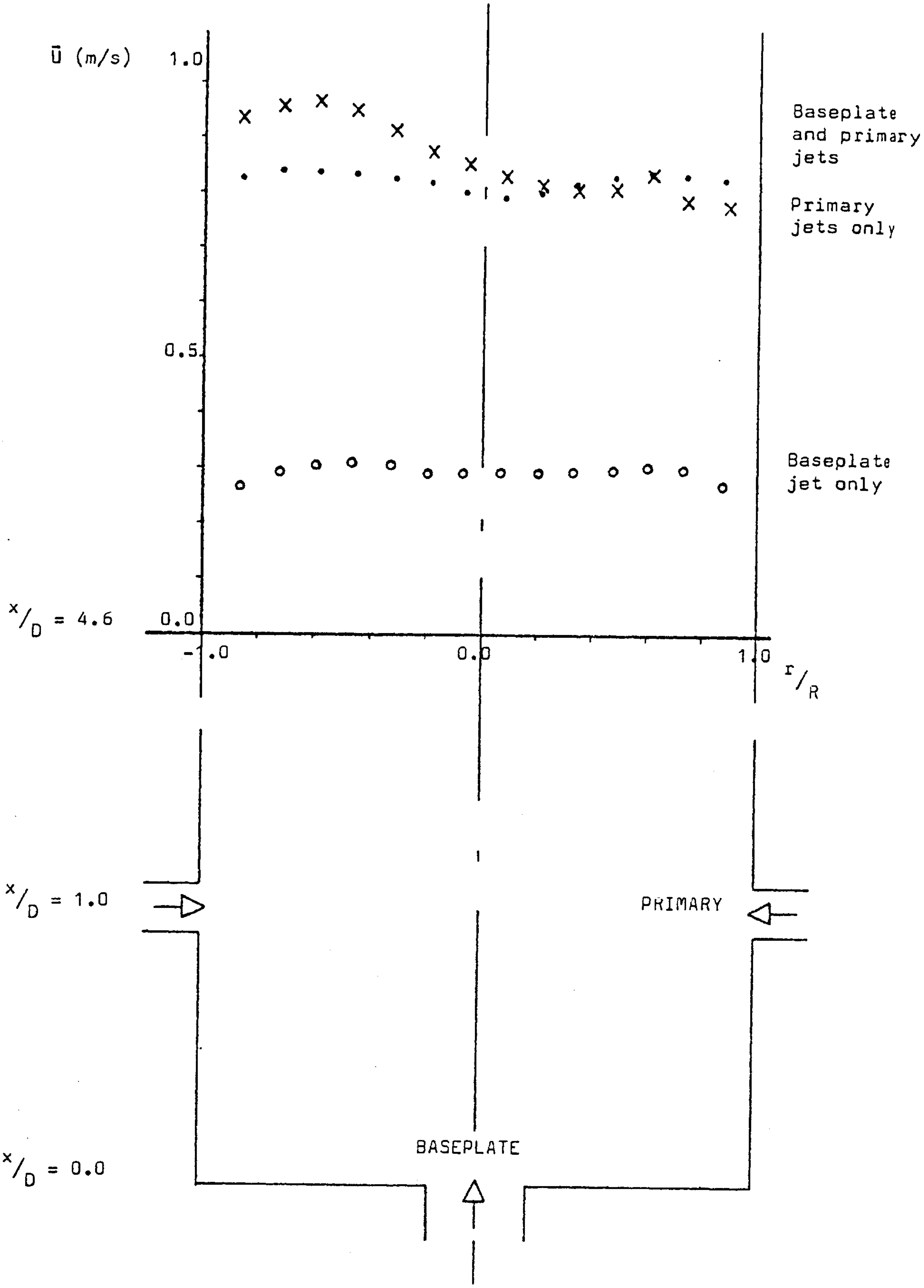

(a) Mean axial velocity profiles at x/D = 4.6 for Case 1 ($\theta = 0^{\circ}$)

Figure 5.3.2 Measured profiles for geometry without a baffle

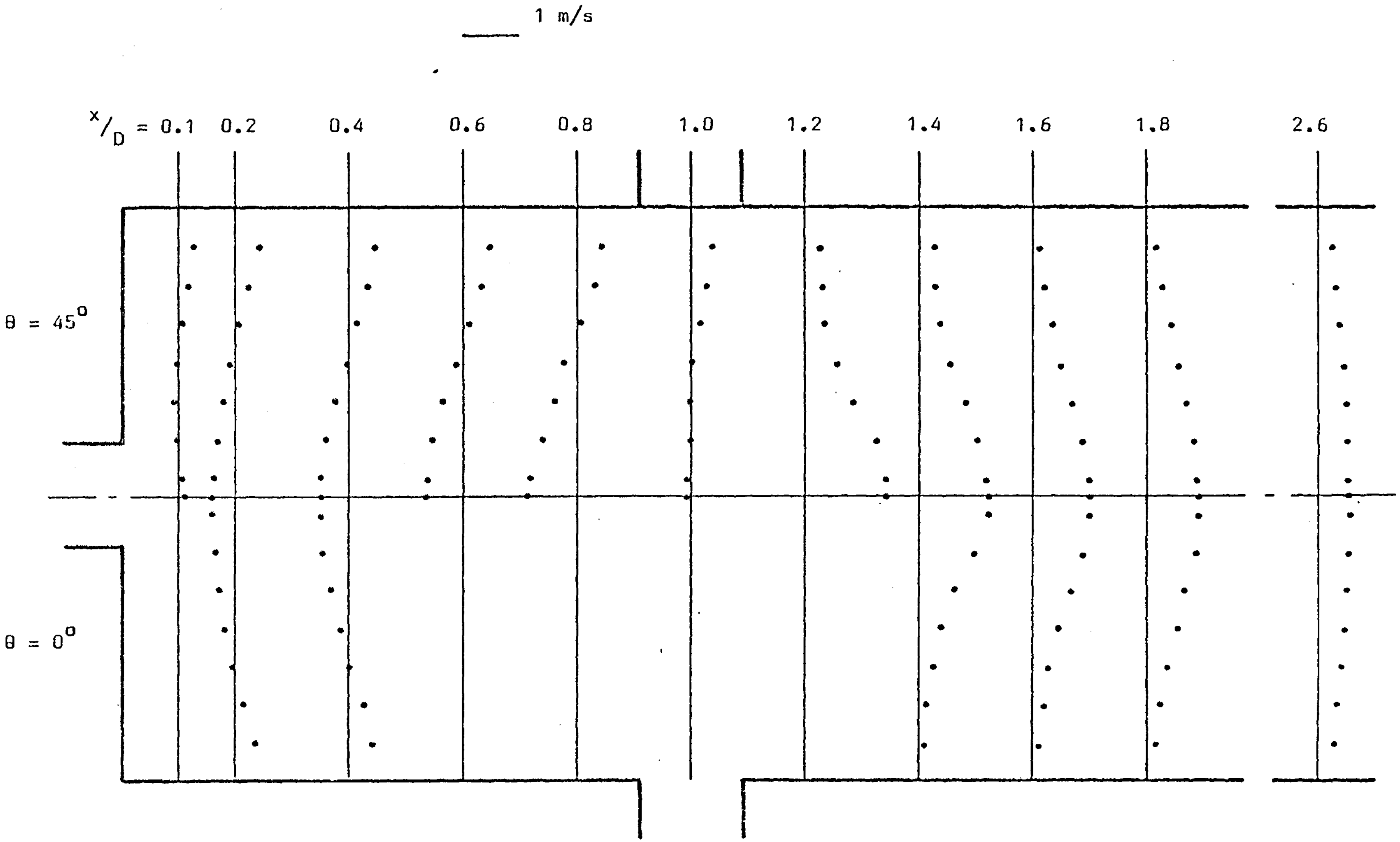

Figure 5.3.2 (b) Measured mean axial velocity profiles for Case 2

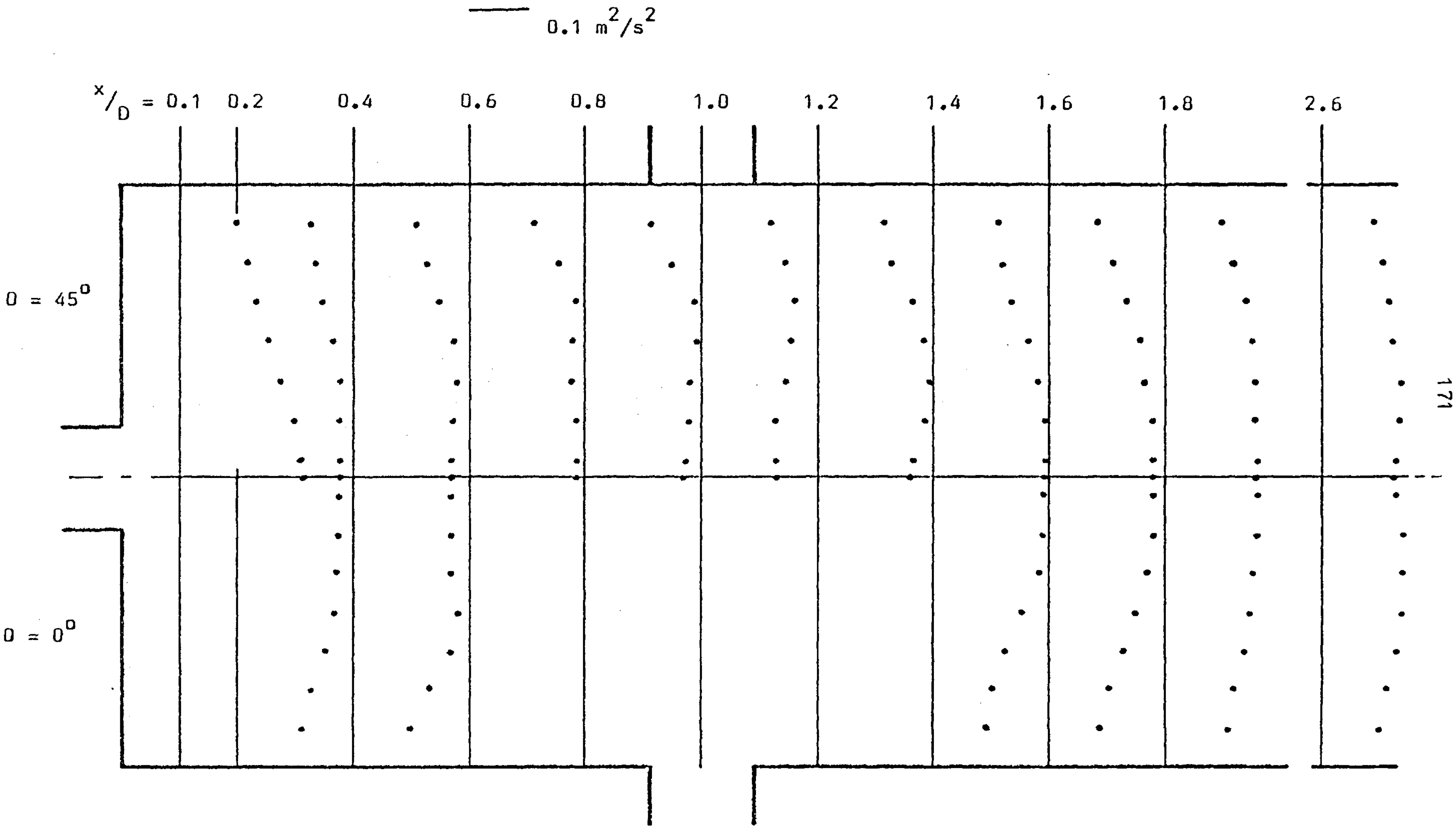

Figure 5.3.2 (c)   Measured normal stress profiles for Case 2

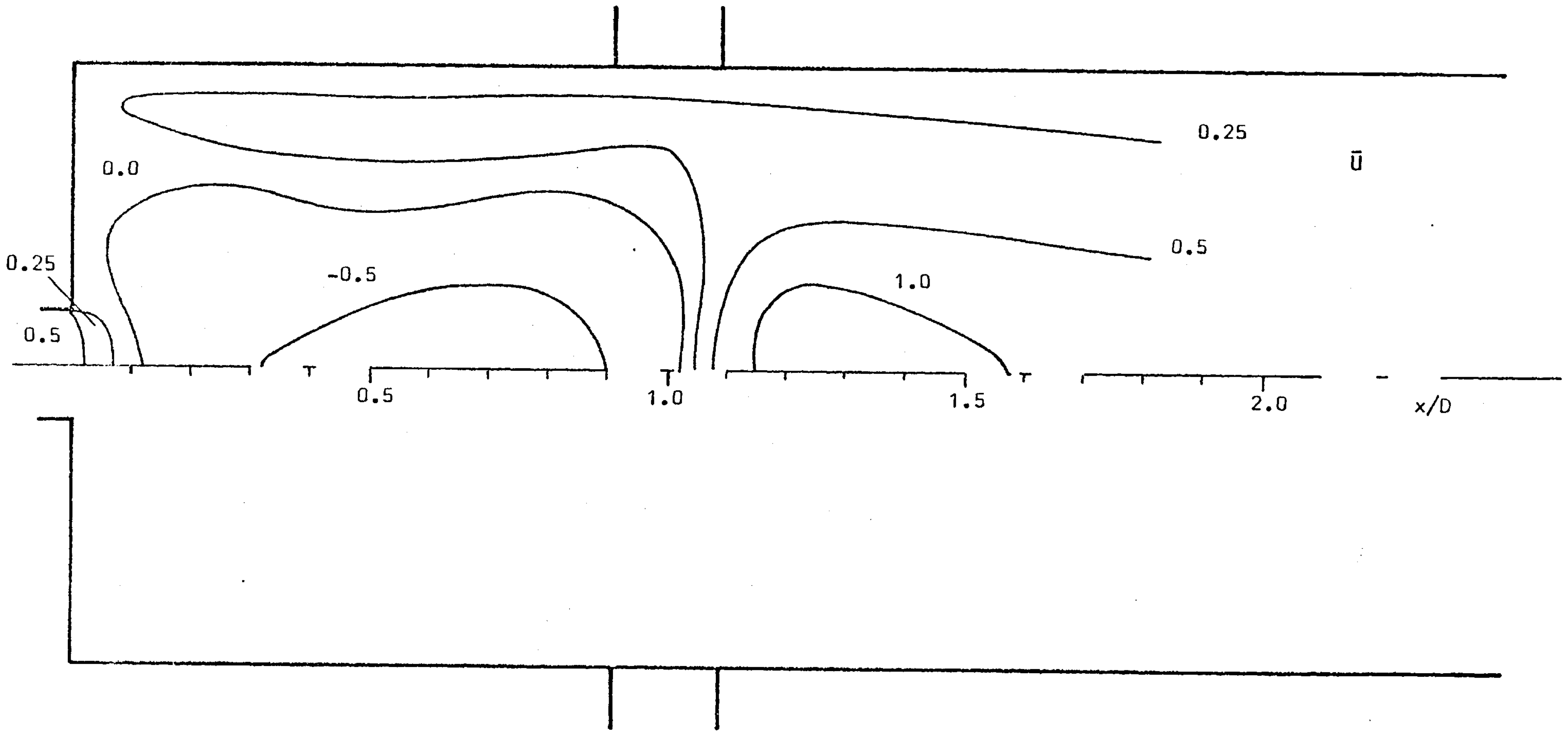

Figure 5.3.3 Measured mean axial velocity contours for Case 2 ($\theta = 45^0$)

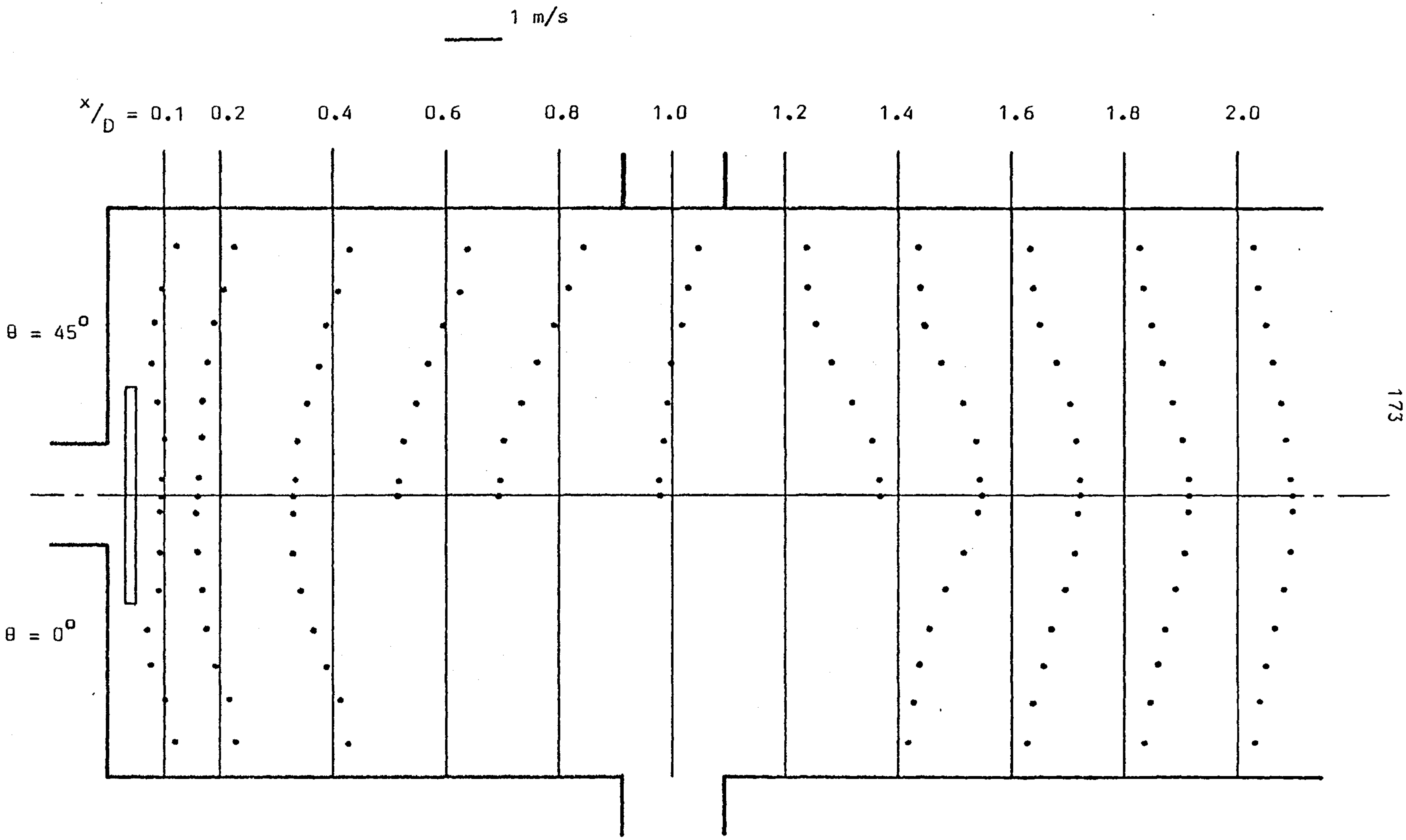

Figure 5.3.4 (a)   Measured mean axial velocity profiles for Case 3

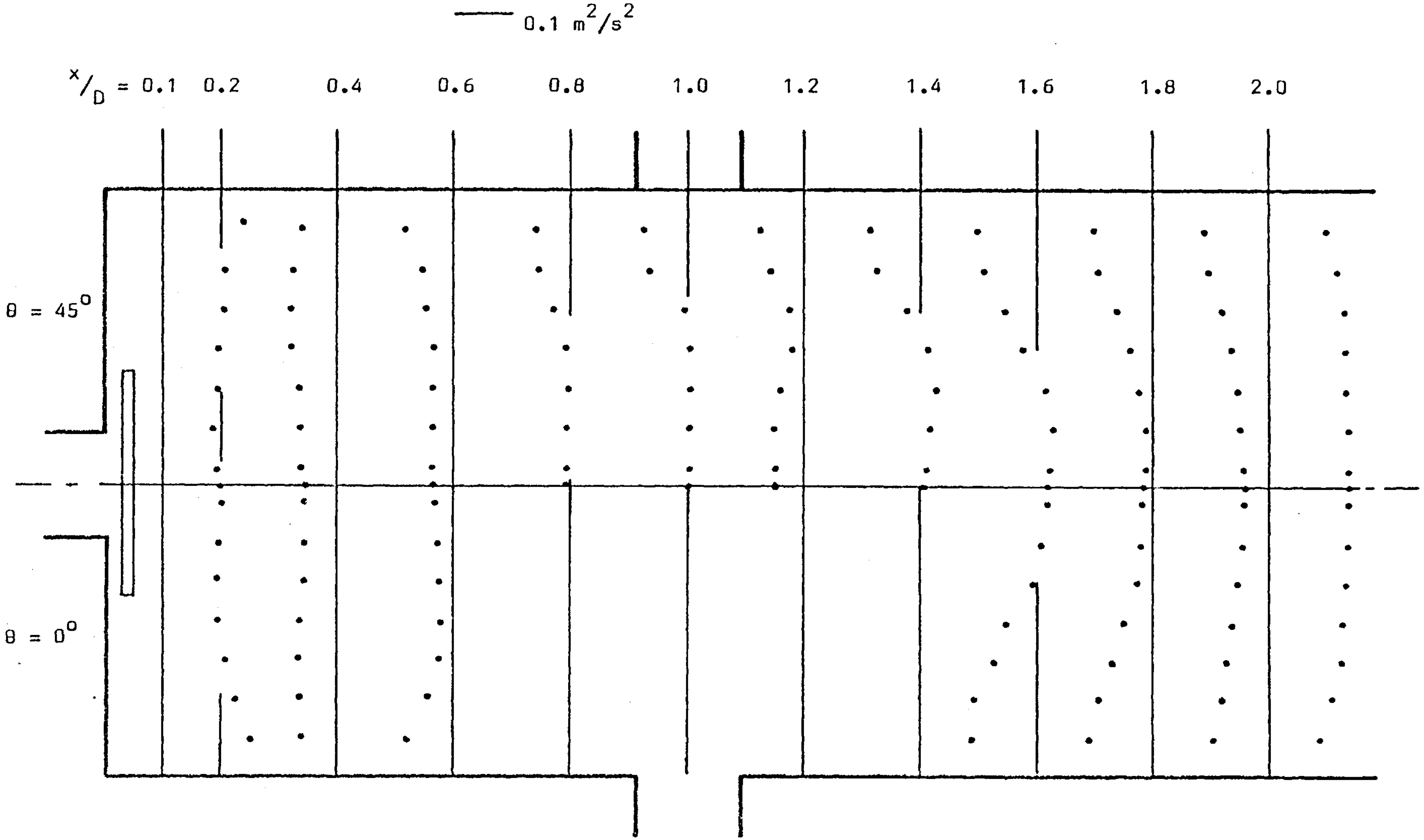

Figure 5.3.4 (b) Measured normal stress profiles for Case 3

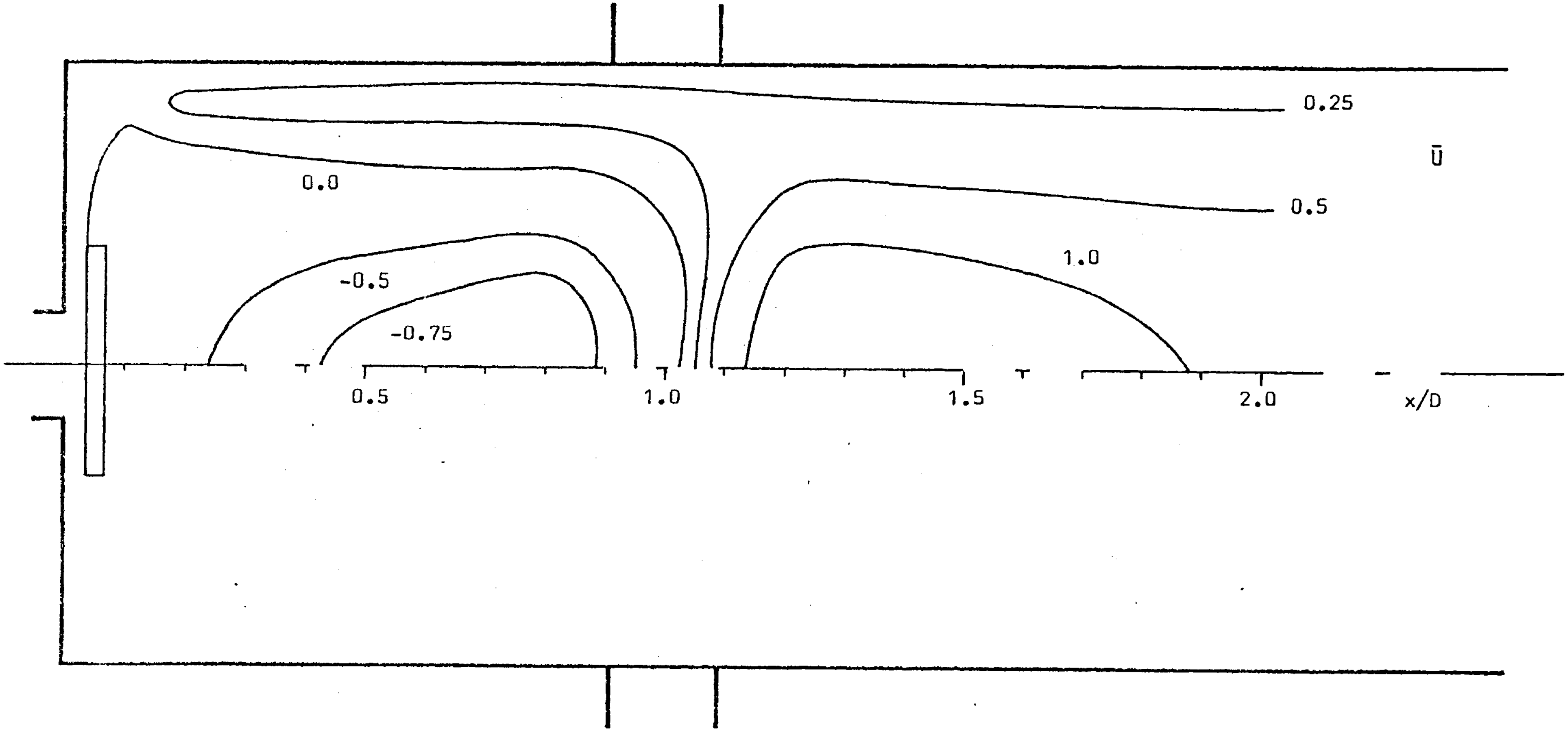

Figure 5.3.5 Measured mean axial velocity contours for Case 3 ($\theta = 45^{o}$)

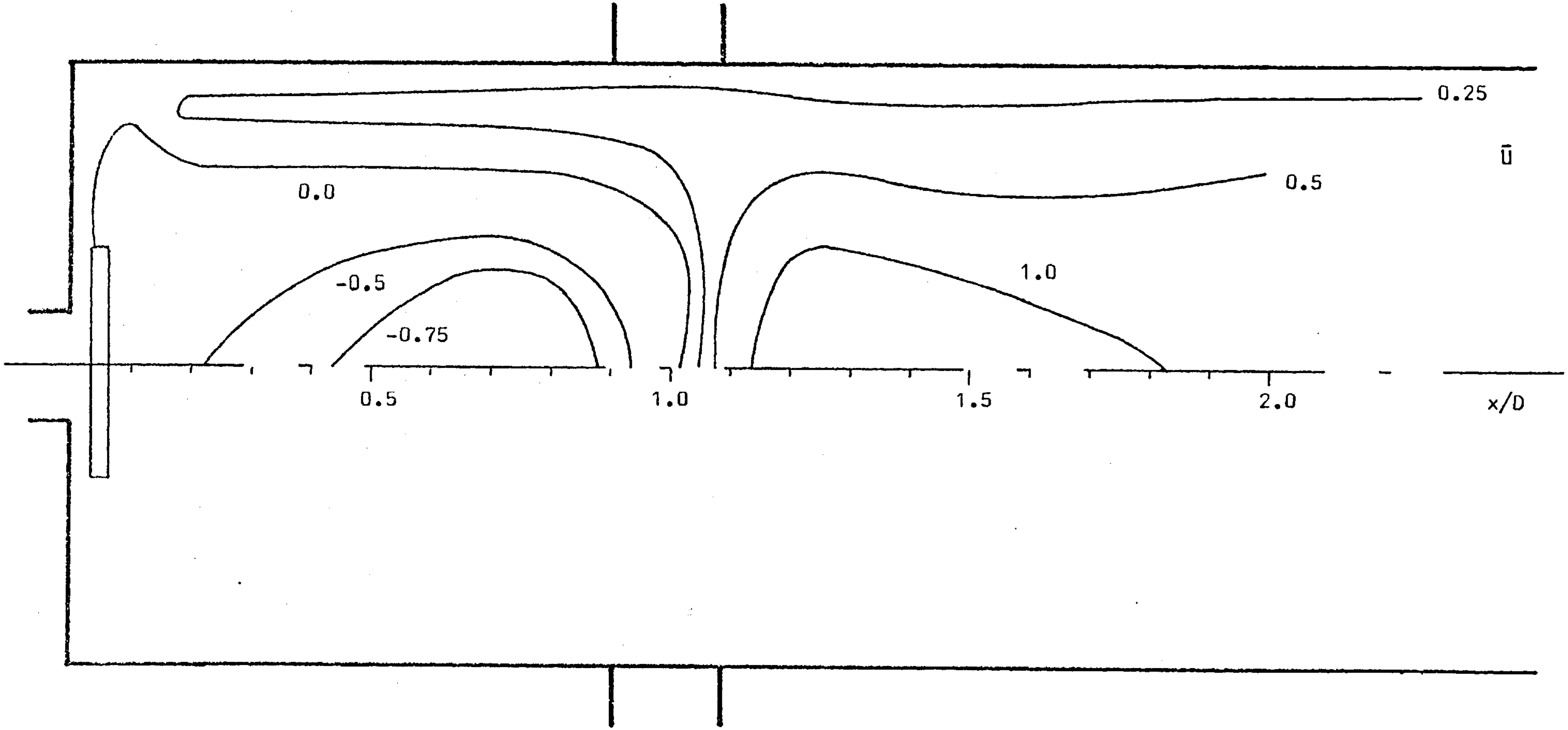

Figure 5.3.6 Measured mean axial velocity contours for Case 4 ($\theta = 45^{\circ}$)

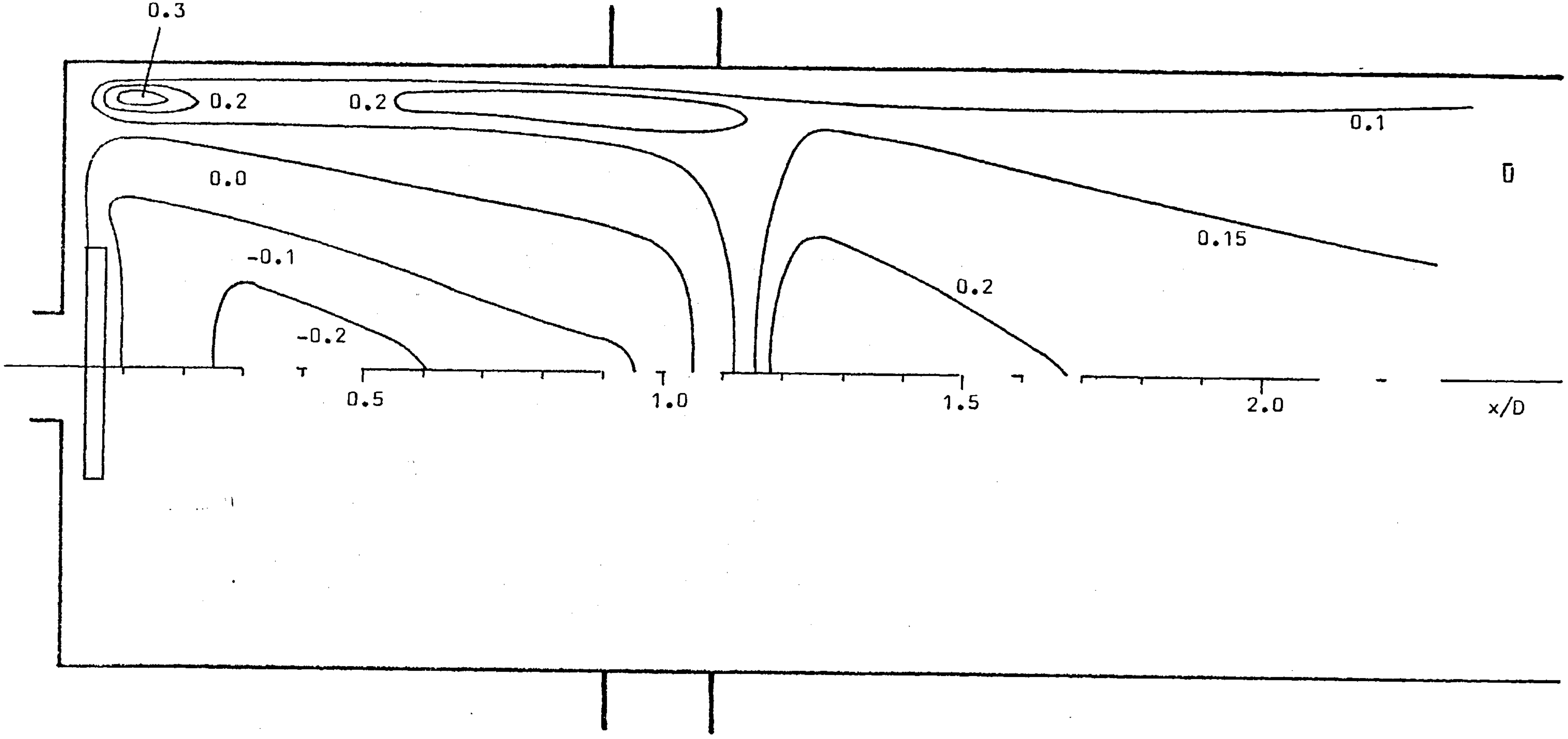

Figure 5.3.7 Measured mean axial velocity contours for Case 5 ($\theta = 45^{0}$)

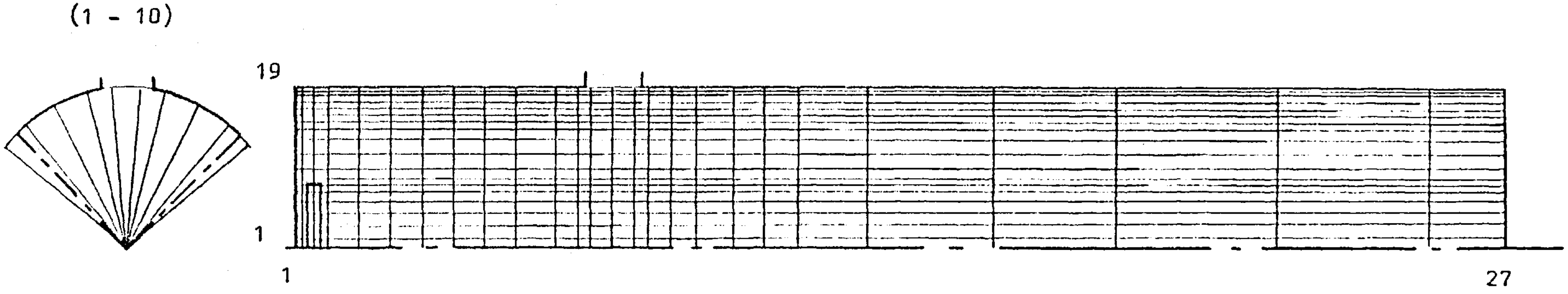

Figure 5.4.1 The finite-difference grid (10 x 19 x 27 nodes)

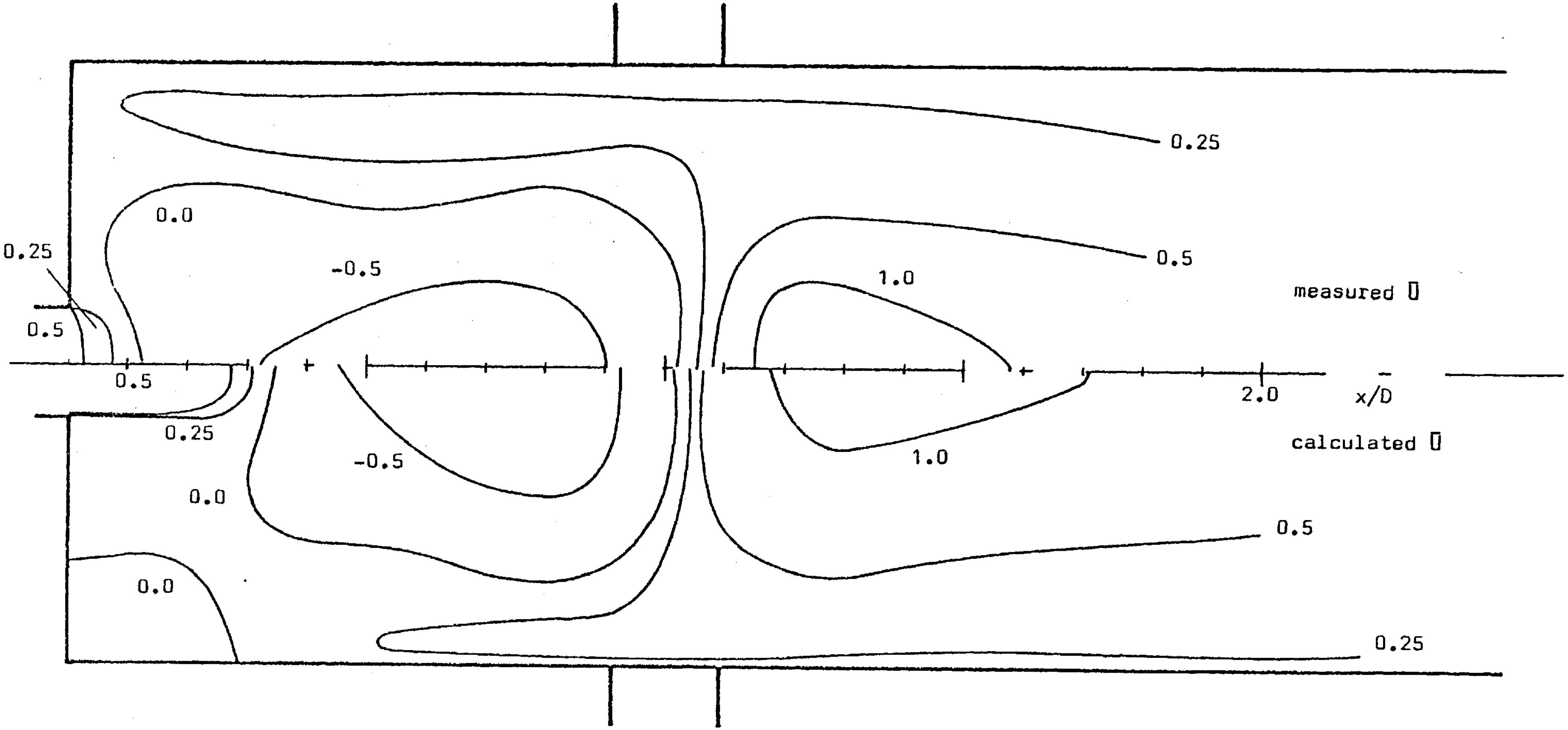

Figure 5.5.1 Comparison of calculated and measured mean axial velocity contours for Case 2 (θ = 45°)

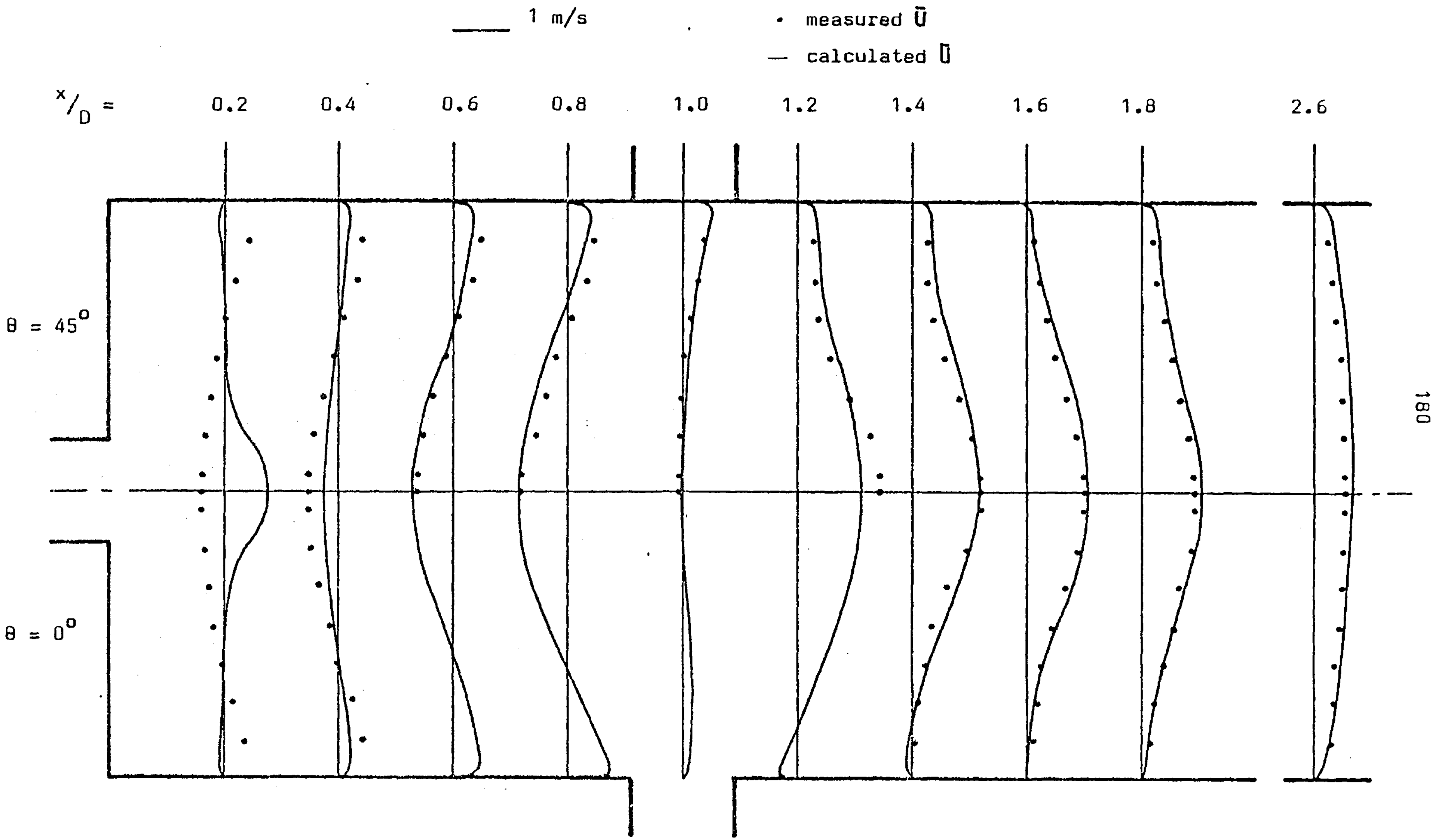

Figure 5.5.2 Comparison of calculated and measured mean axial velocity profiles for Case 2

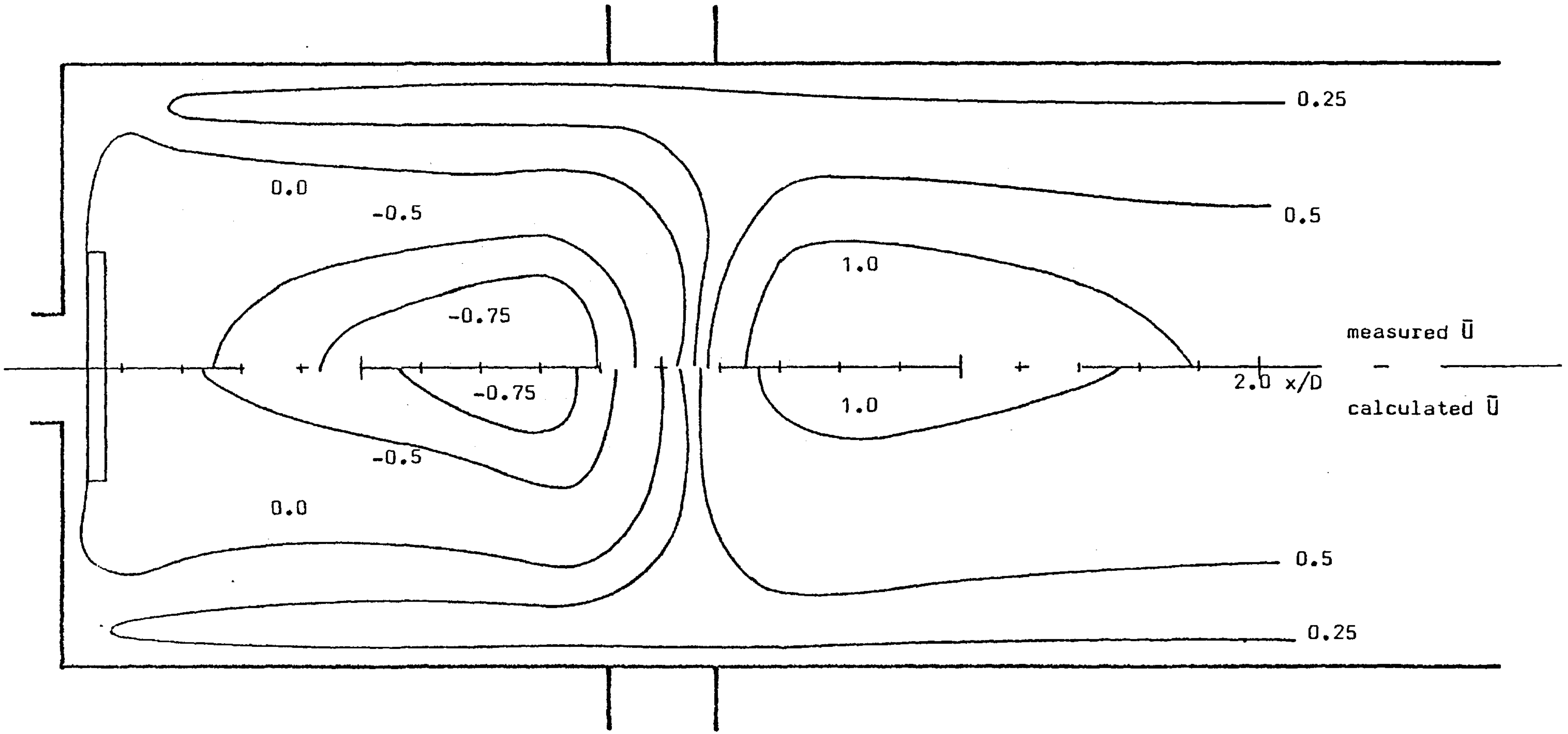

Figure 5.5.3 Comparison of calculated and measured mean axial velocity contours for Case 3 ($\theta = 45^{\circ}$)

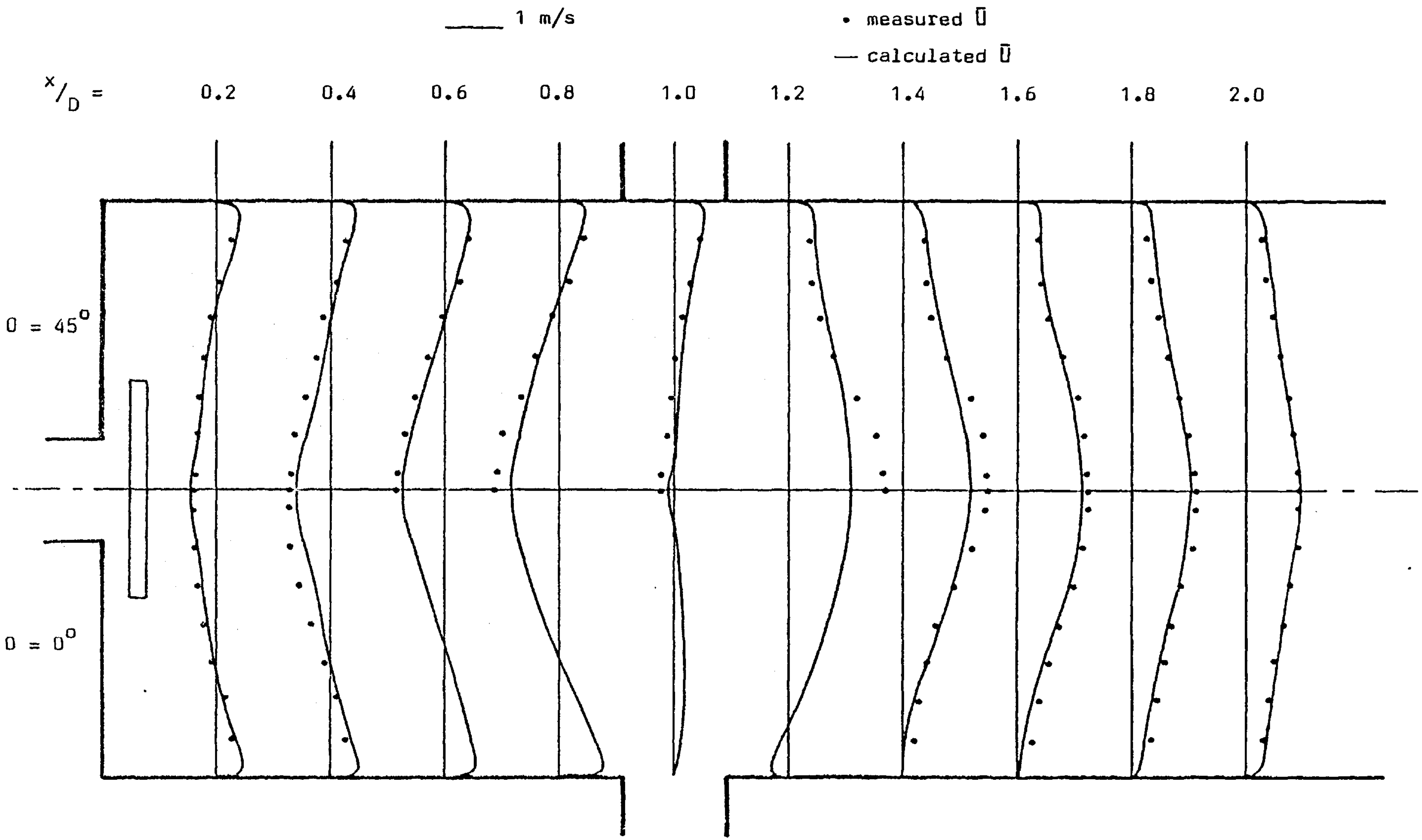

Figure 5.5.4 Comparison of calculated and measured mean axial velocity profiles for Case 3

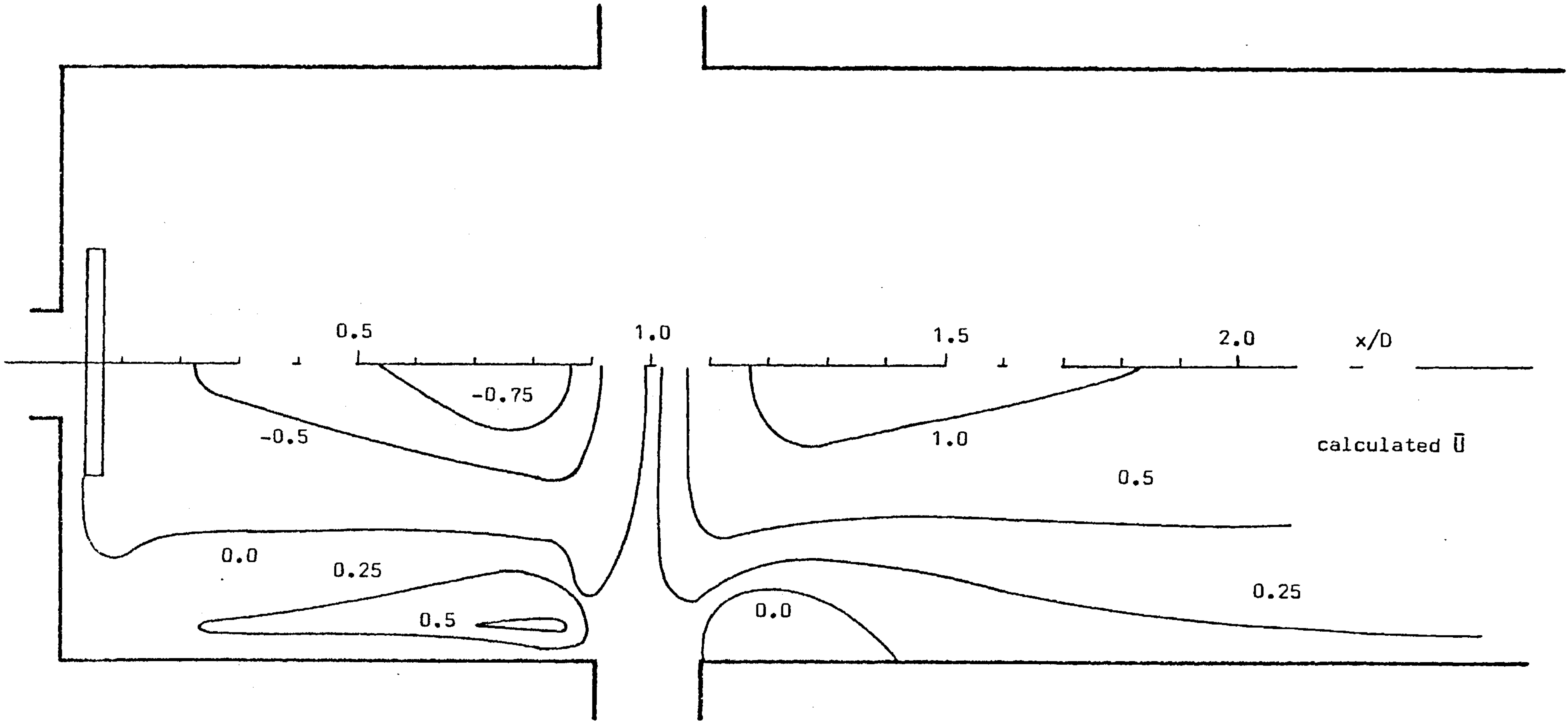

Figure 5.5.5 Calculated mean axial velocity contours for Case 3 ($\theta = 0^o$)

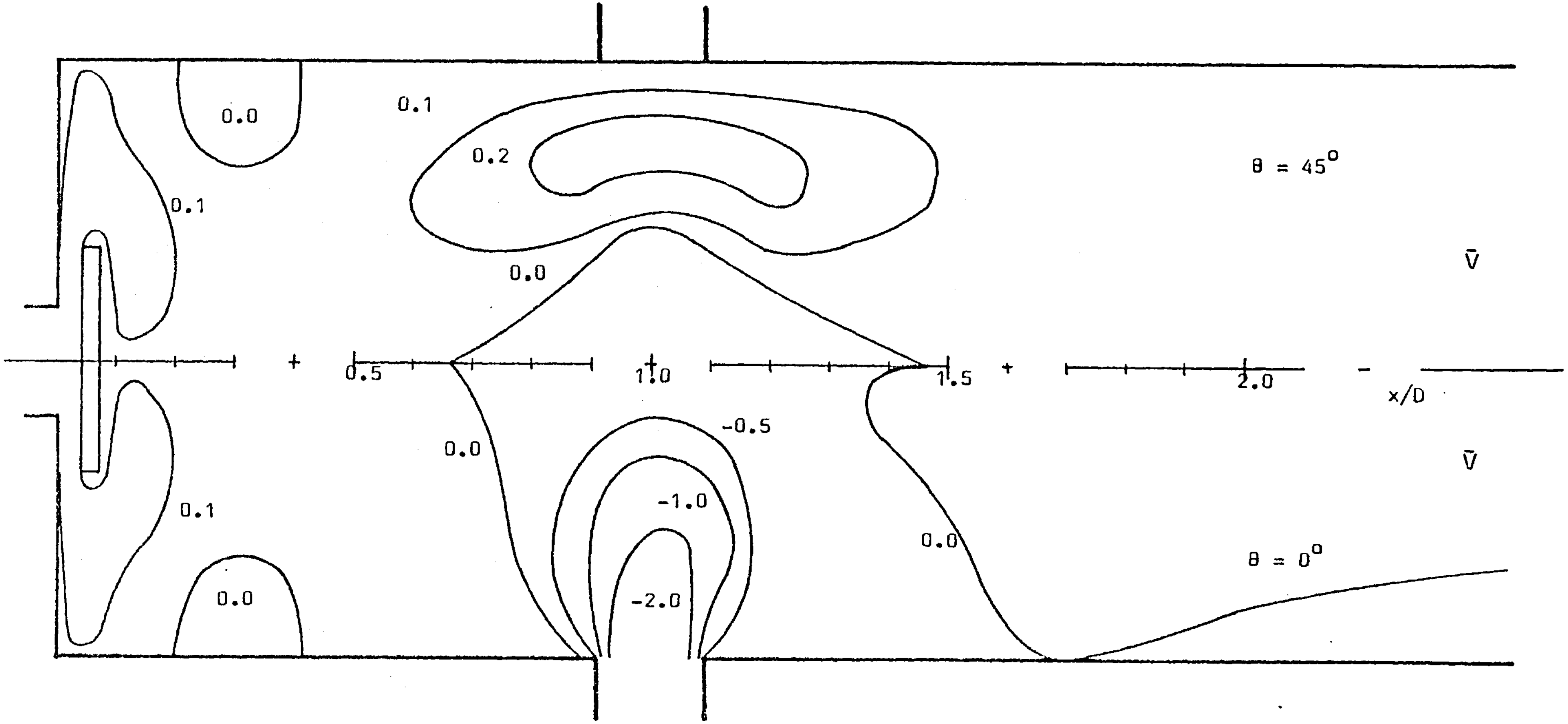

Figure 5.5.6 Calculated mean radial velocity contours for Case 3

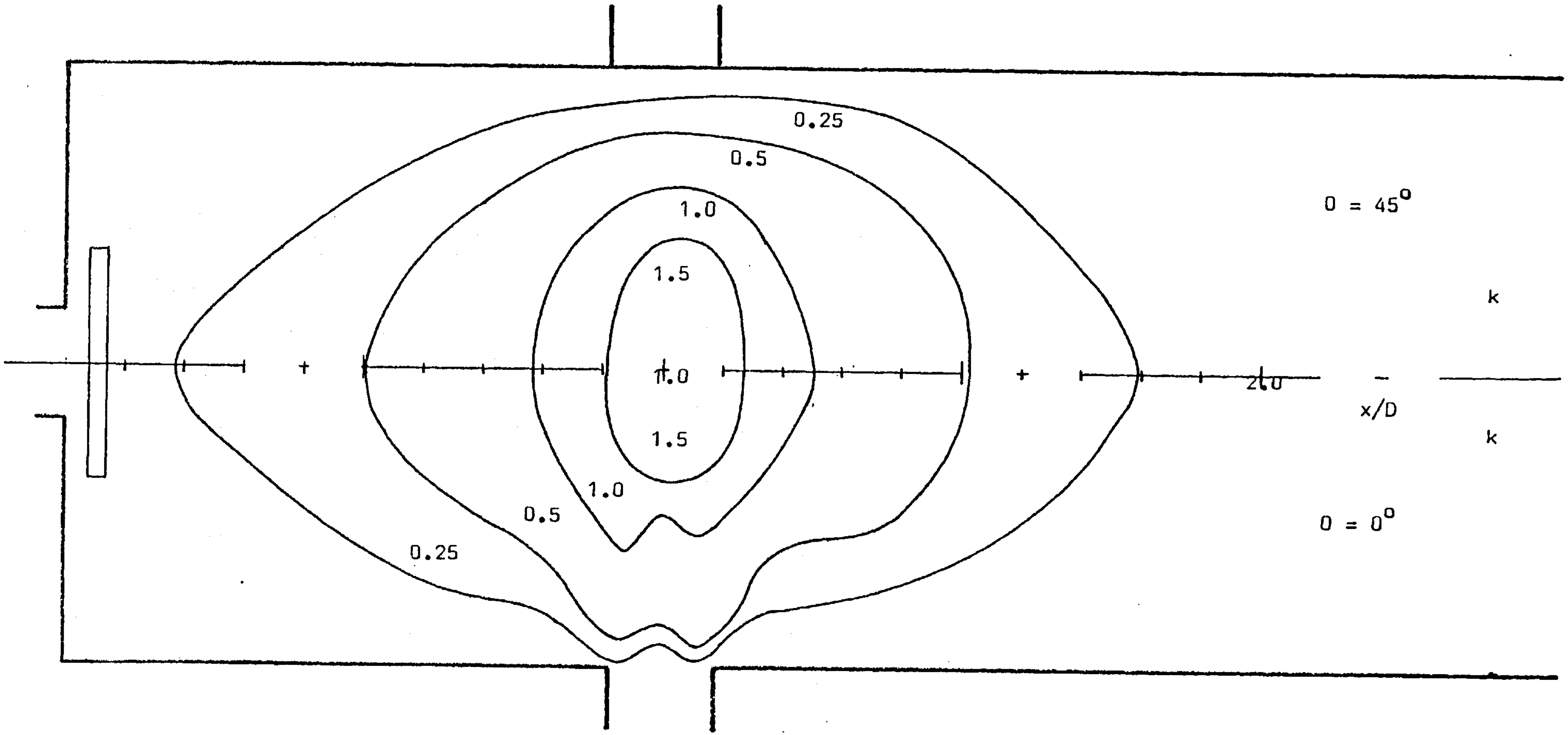

Figure 5.5.7 ; Calculated turbulence kinetic energy contours for Case 3

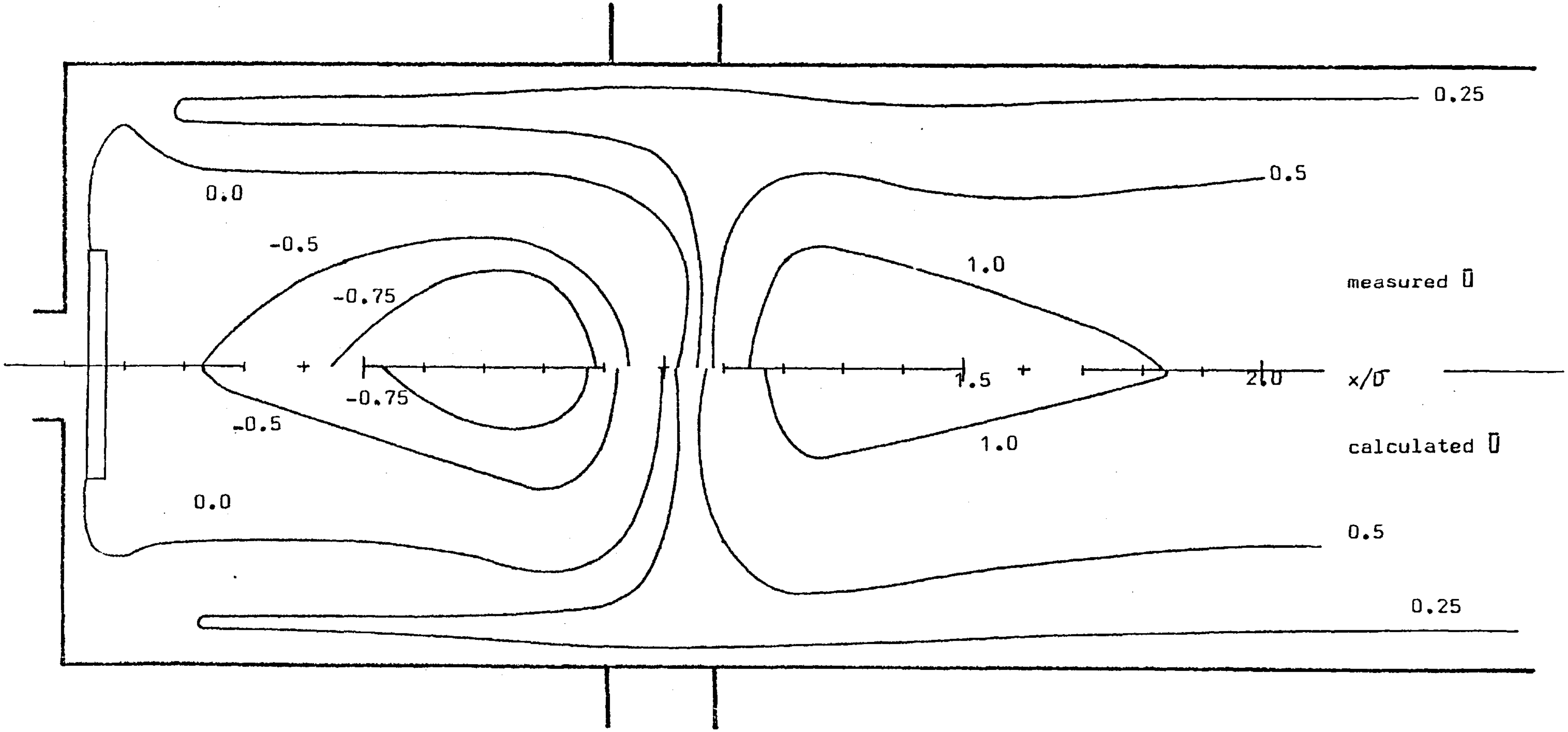

Figure 5.5.8 Comparison of calculated and measured mean axial velocity contours for Case 4 ($0 = 45^{o}$)

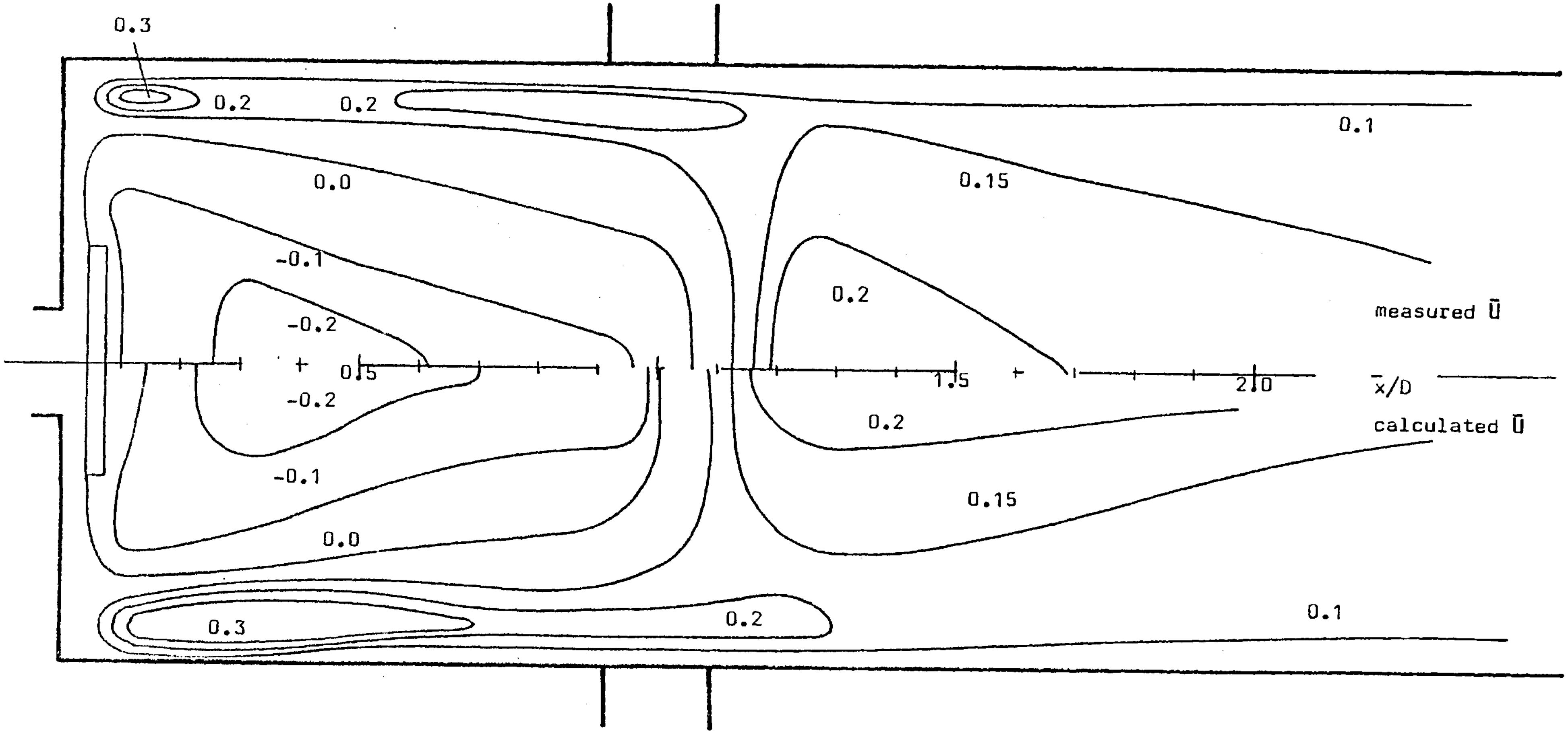

Figure 5.5.9 Comparison of calculated and measured mean axial velocity contours for Case 5 ($\theta = 45^{\circ}$)

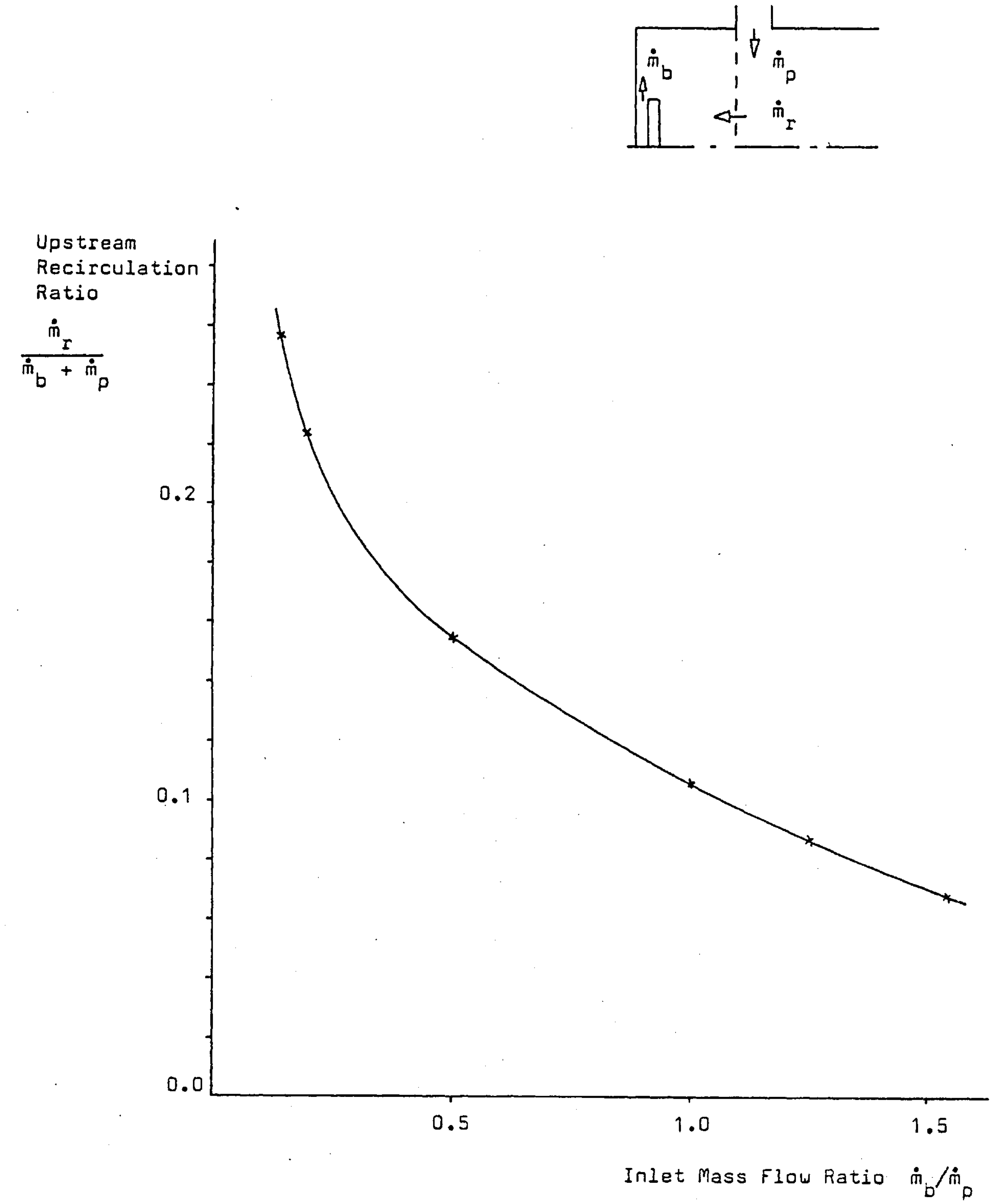

Figure 5.5.10 Relationship between Upstream Recirculation Ratio and Inlet Mass Flow Ratio

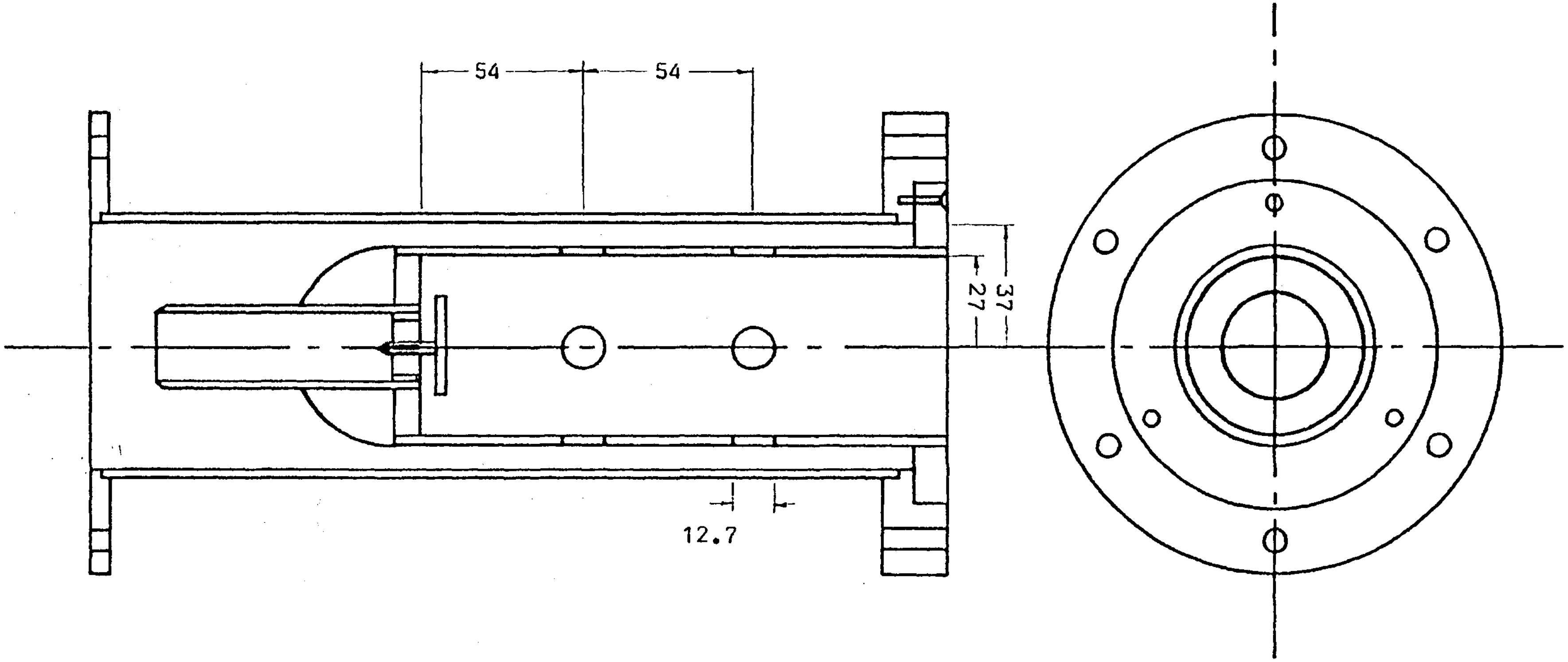

Figure 6.2.1 The three-dimensional water model with an annulus

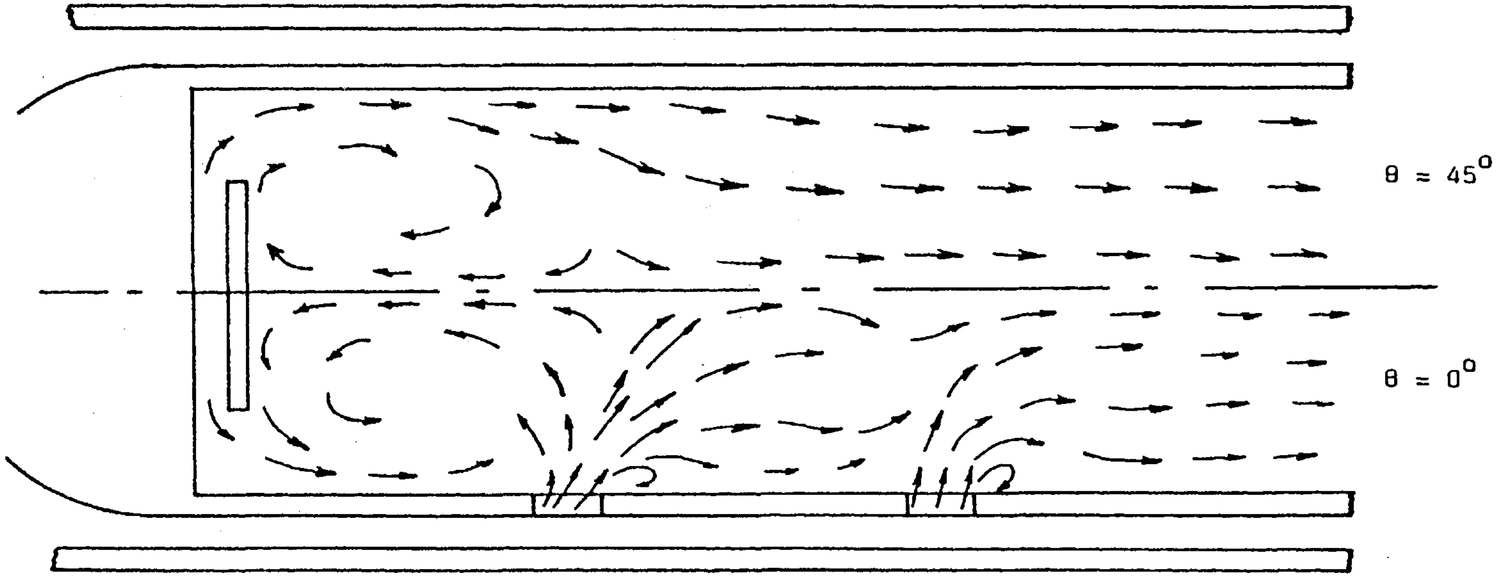

Figure 6.2.2 The flow pattern from flow visualisation

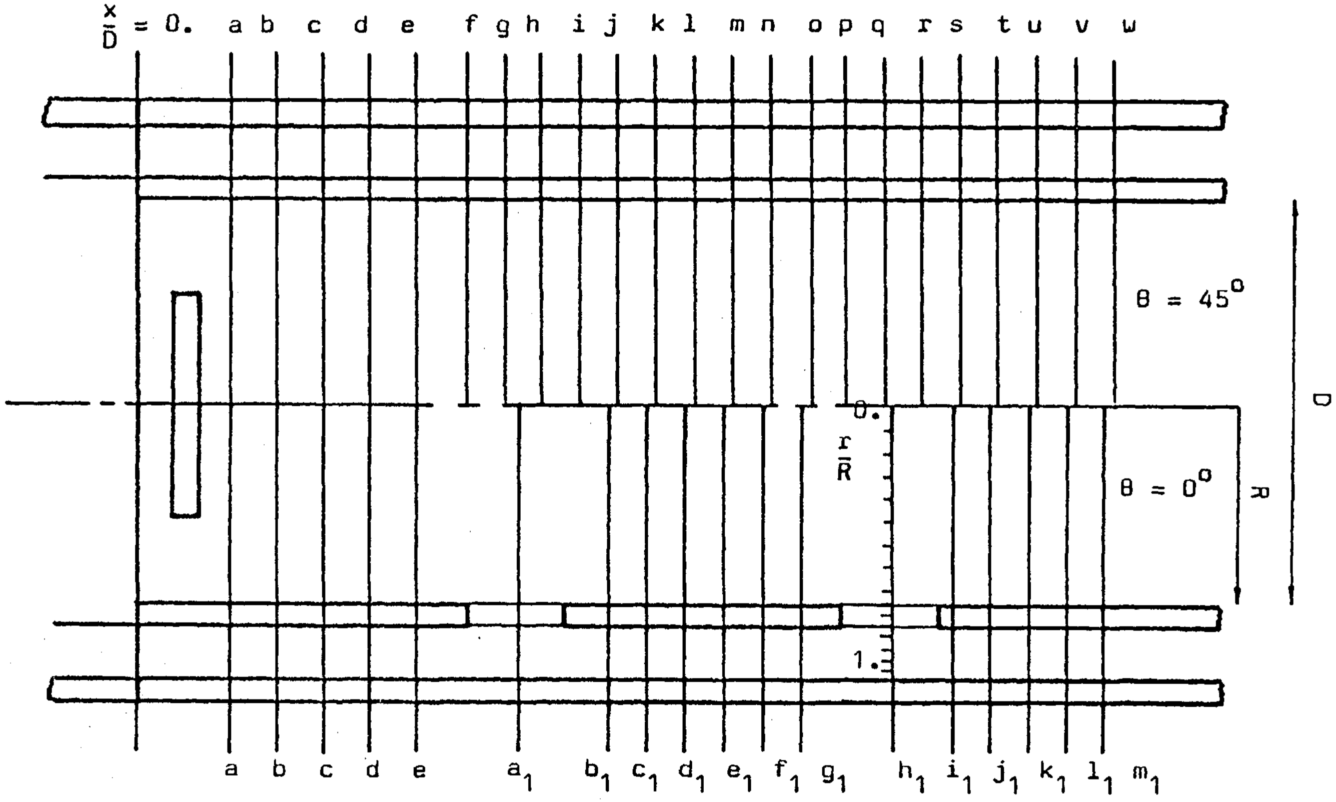

a = 0.25
b = 0.37
c = 0.49
d = 0.61
e = 0.74
f = 0.86
g = 0.96
h = 1.06
i = 1.16
j = 1.26
k = 1.36
l = 1.46

m = 1.56
n = 1.66
o = 1.76
p = 1.86
q = 1.96
r = 2.06
s = 2.16
t = 2.26
u = 2.36
v = 2.46
w = 2.56

a_1 = 1.00
b_1 = 1.24
c_1 = 1.34
d_1 = 1.44
e_1 = 1.54
f_1 = 1.64
g_1 = 1.74

h_1 = 2.00
i_1 = 2.14
j_1 = 2.24
k_1 = 2.34
l_1 = 2.44
m_1 = 2.54

Figure 6.3.1 The measuring locations

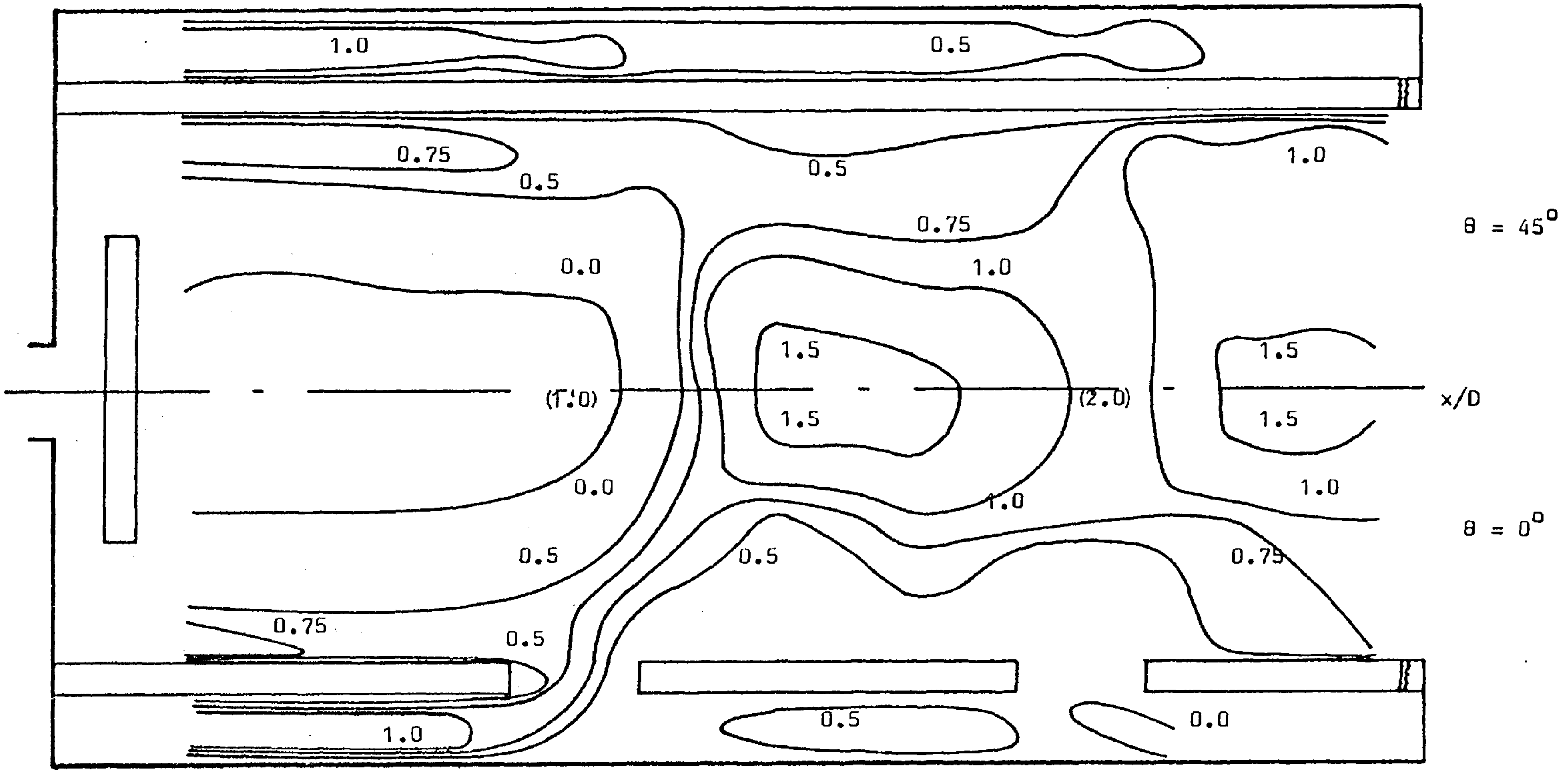

Figure 6.3.2 Measured mean axial velocity contours for θ = 0° and θ = 45° planes

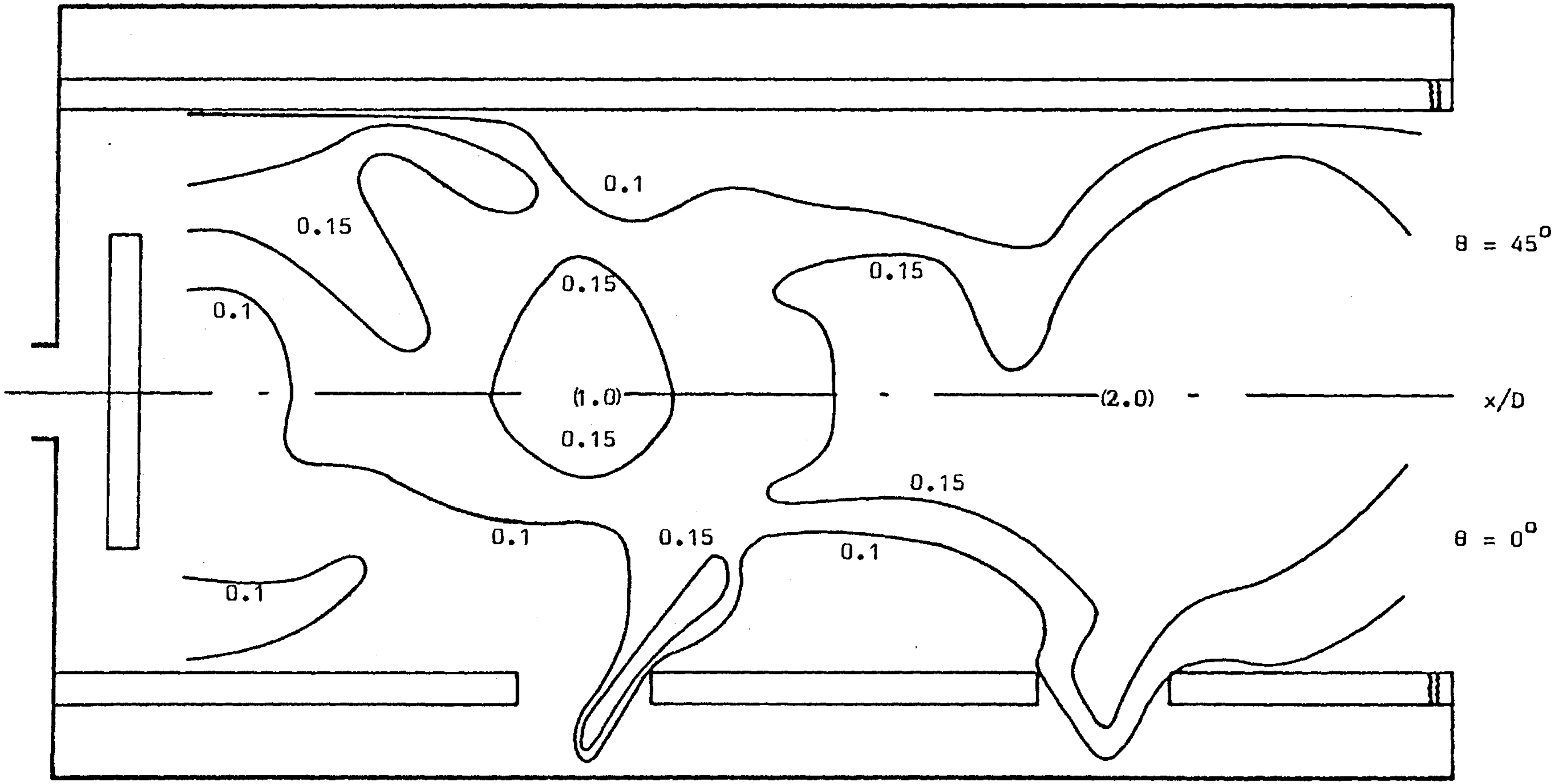

Figure 6.3.3 Measured normal stress contours for $\theta = 0^o$ and $\theta = 45^o$ planes

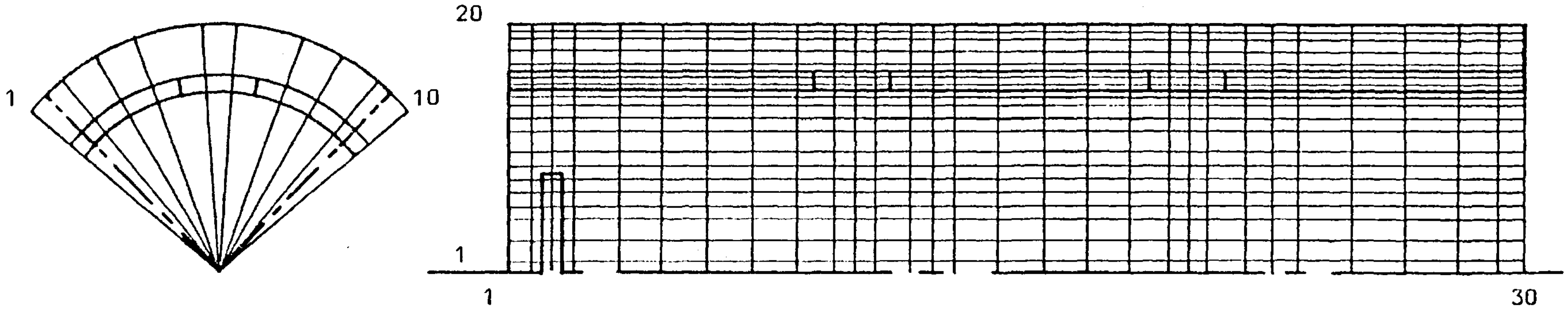

Figure 6.4.1 The finite-difference grid (10 x 20 x 30 nodes)

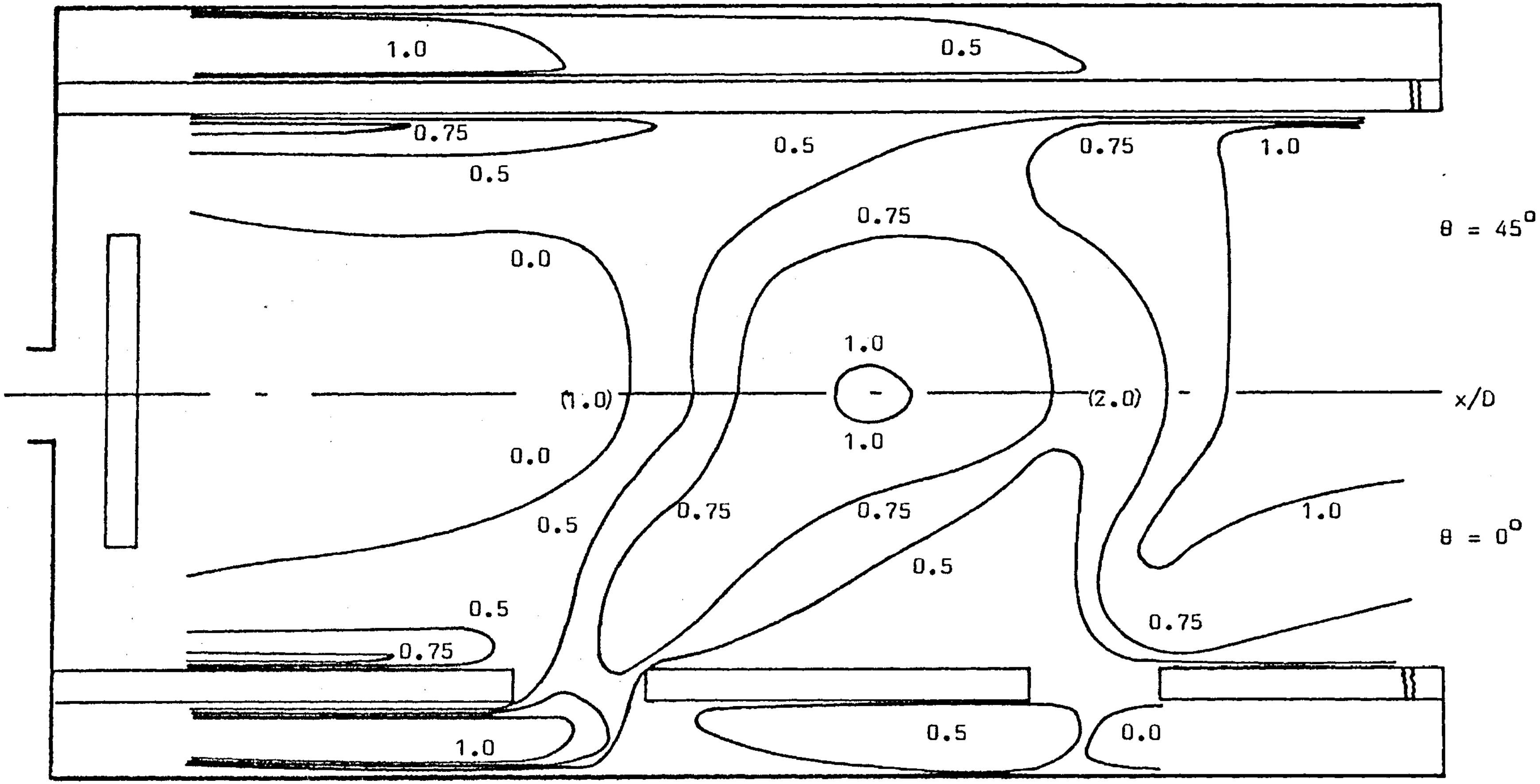

Figure 6.5.1 Calculated mean axial velocity contours for $\theta = 0^\circ$ and $\theta = 45^\circ$ planes

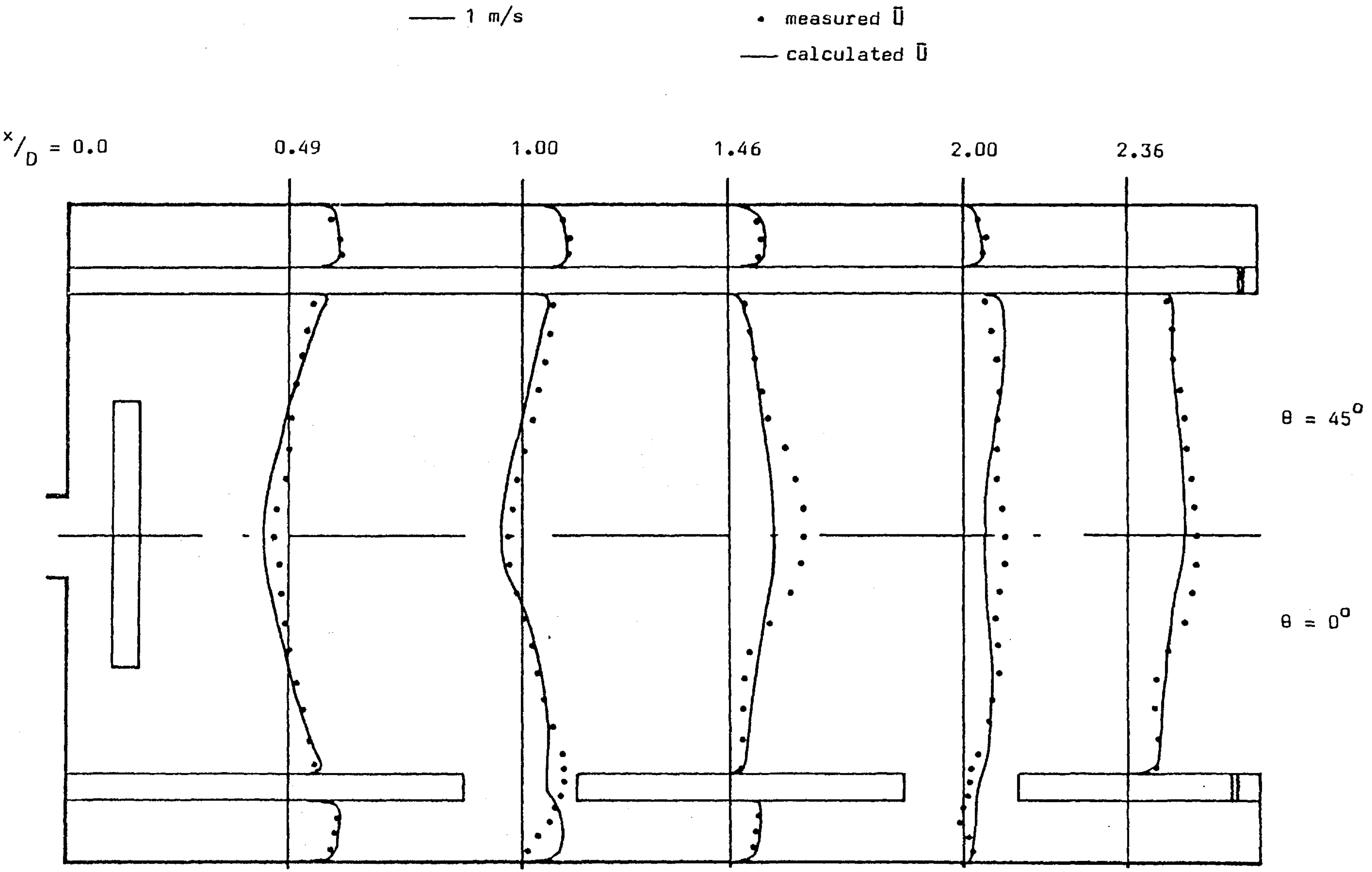

Figure 6.5.2 Comparison of measured and calculated mean axial velocity profiles

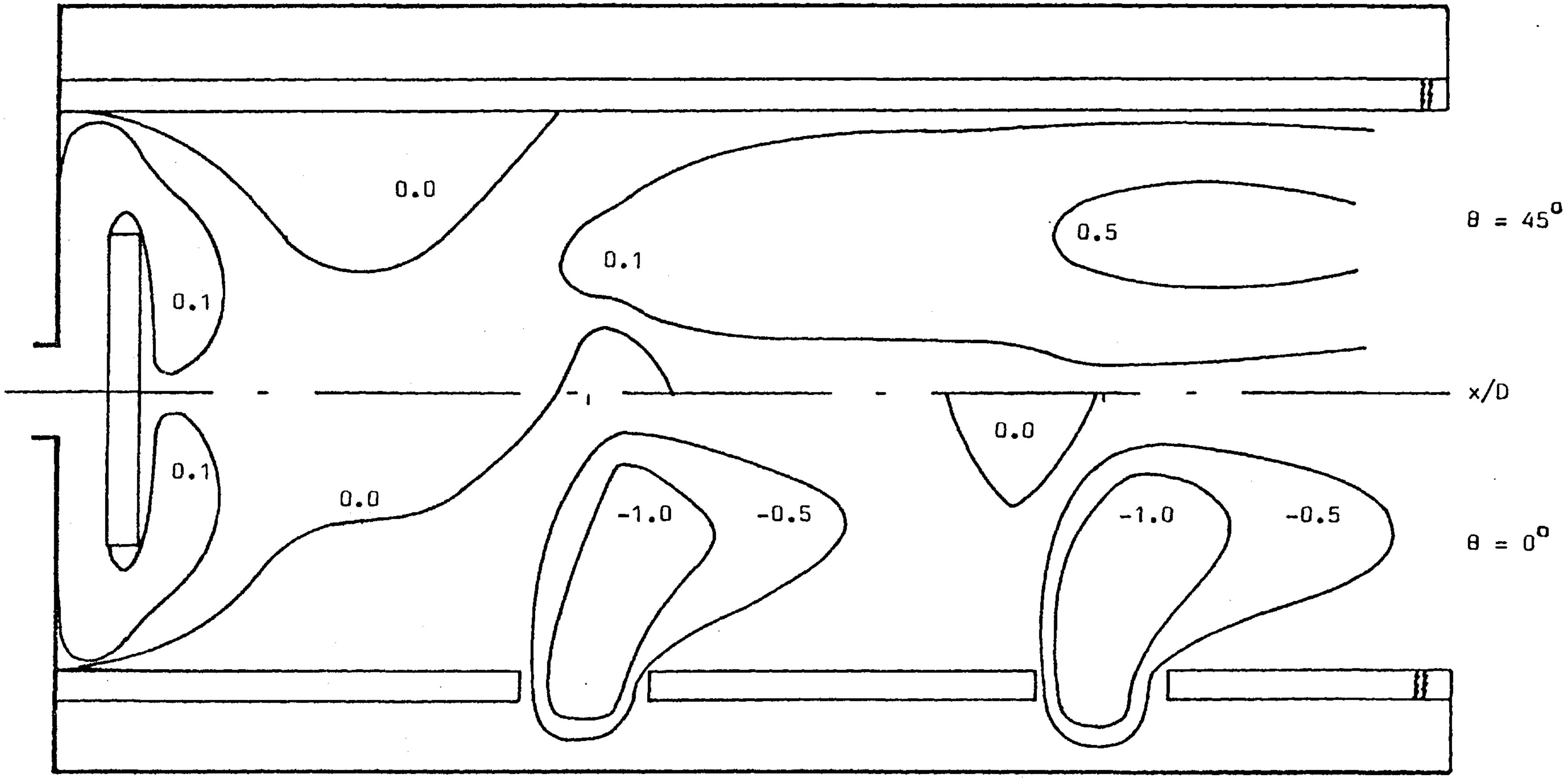

Figure 6.5.3 Calculated mean radial velocity contours for $\theta = 0^{\circ}$ and $\theta = 45^{\circ}$ planes

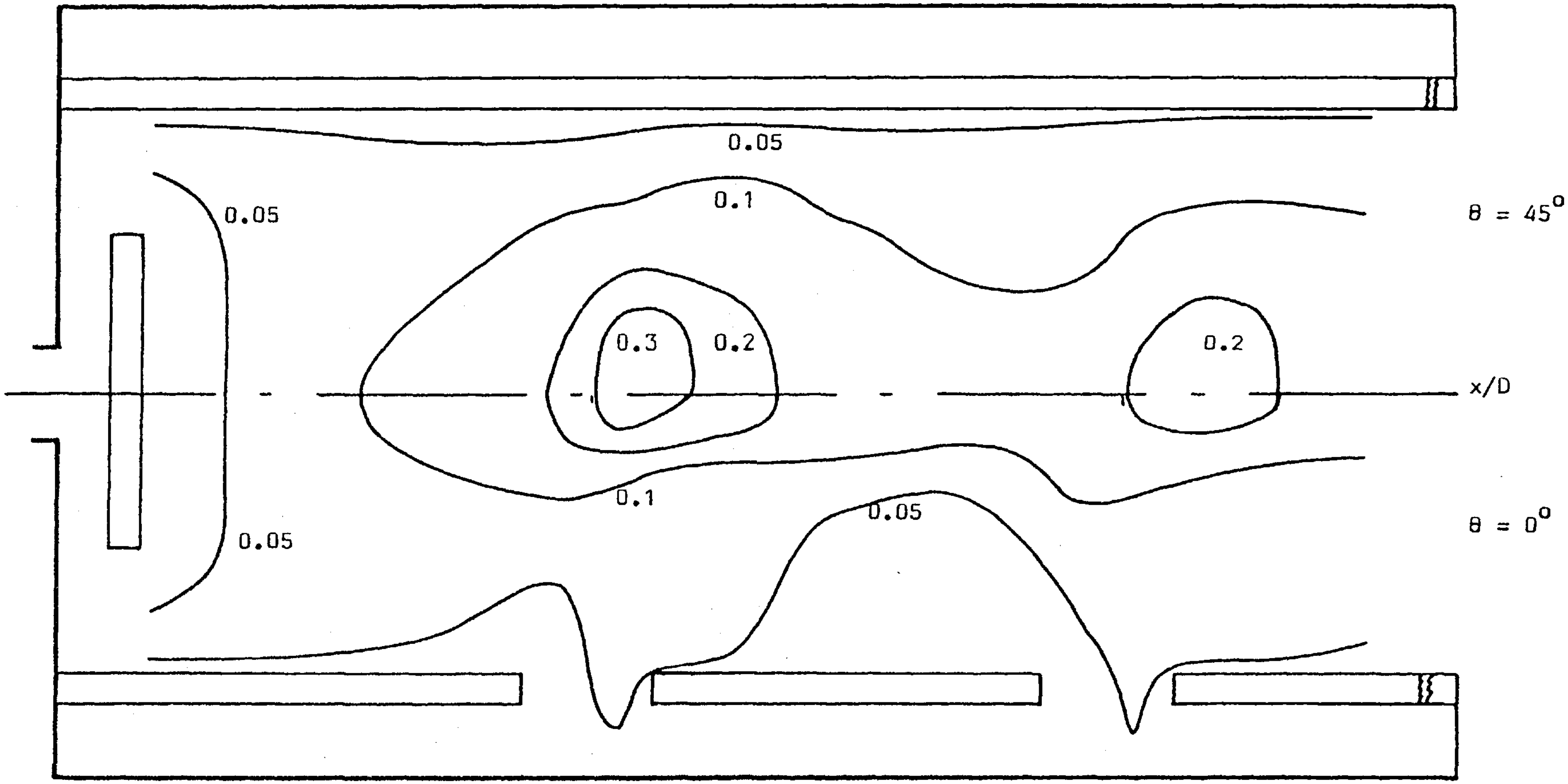

Figure 6.5.4 Calculated turbulence kinetic energy contours for θ = 0° and θ = 45° planes

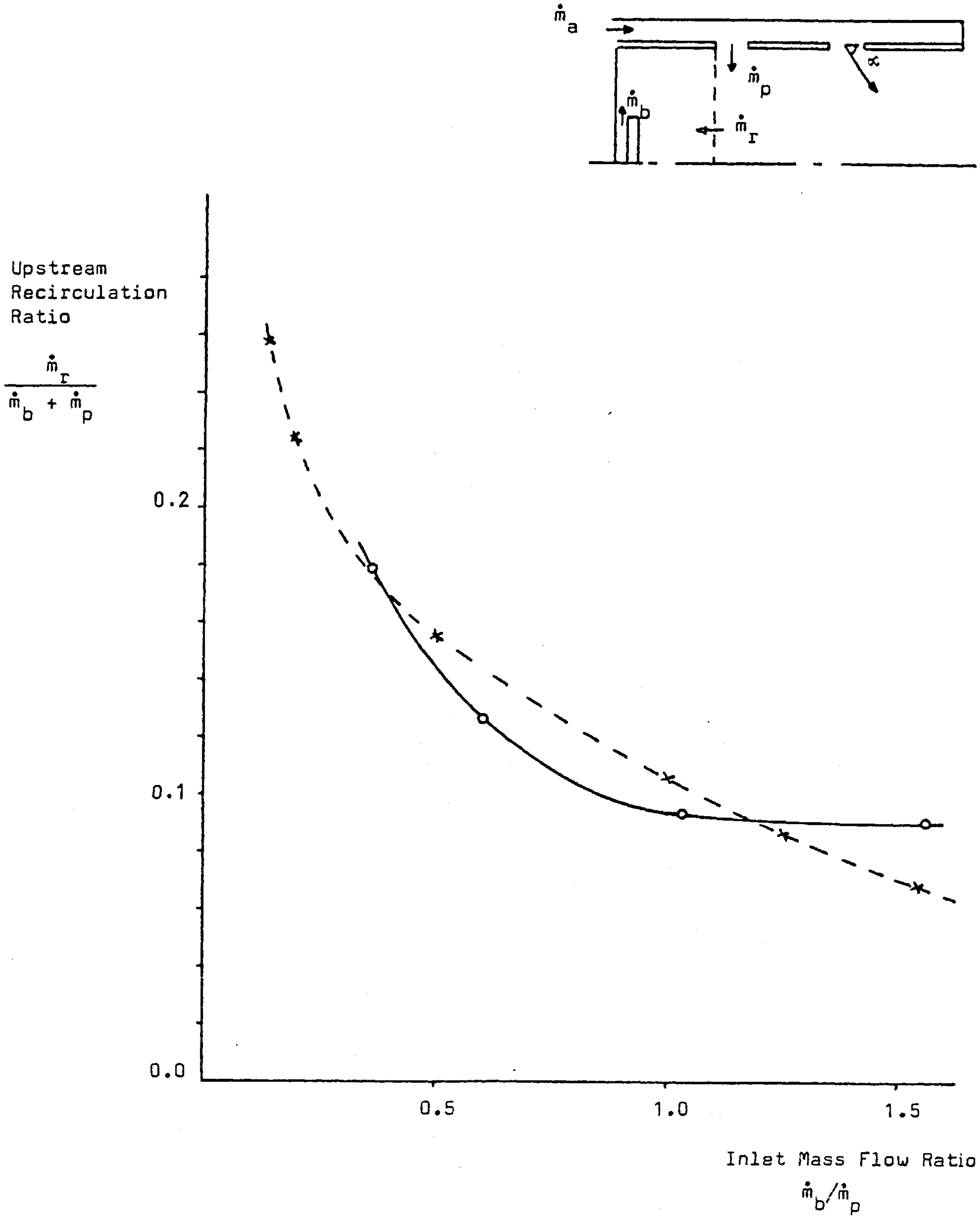

Figure 6.6.1 Relationship between upstream recirculation ratio and inlet mass flow ratio

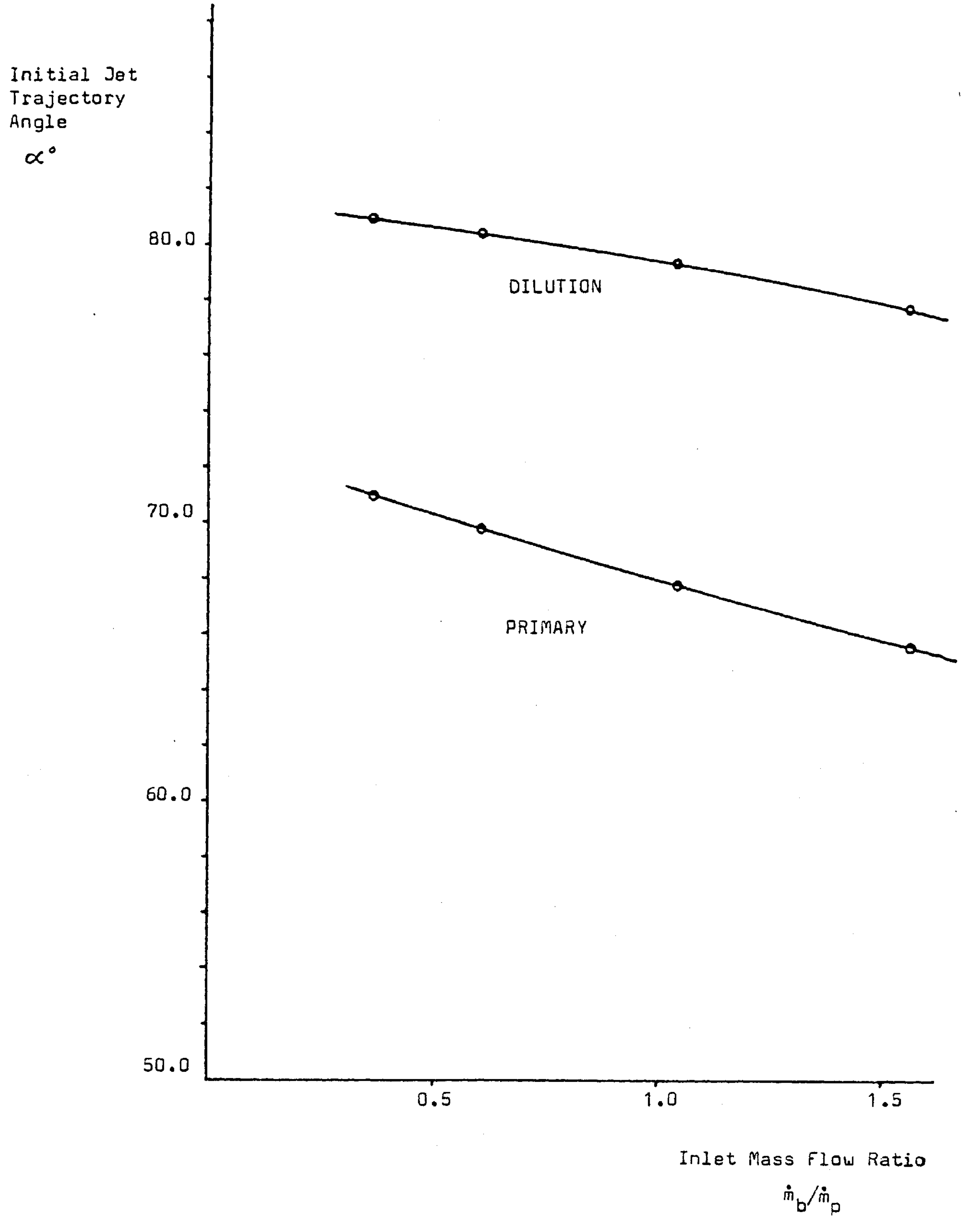

Figure 6.6.2 Relationship between initial jet trajectory angle and inlet mass flow ratio

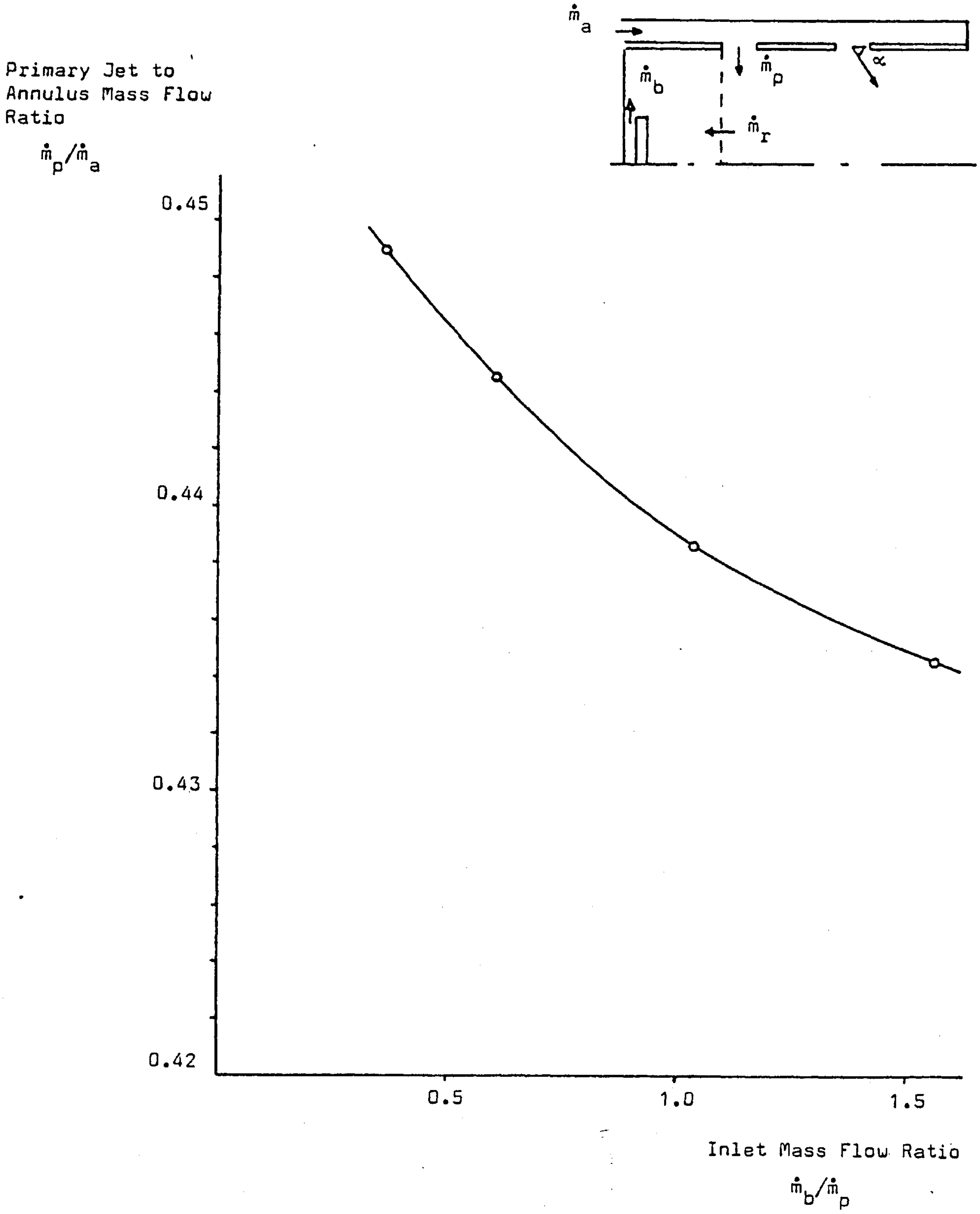

Figure 6.6.3 Relationship between primary jet to annulus mass flow ratio and inlet mass flow ratio